Non-invasive treatment of cardiac arrhythmias by high-intensity focussed ultrasound guided by magnetic resonance imaging

Pierre Bour

THESE PRESENTEE

POUR OBTENIR LE GRADE DE

DOCTEUR DE L'UNIVERSITÉ DE BORDEAUX

ECOLE DOCTORALE SCIENCES DE LA VIE ET DE LA SANTE

SPECIALITE: BIOIMAGERIE

PAR PIERRE BOUR

Traitement non invasif des arythmies cardiaques par ultrasons focalisés de haute intensité guidés par imagerie de résonance magnétique

Sous la direction de: Dr. Quesson Bruno

Soutenue le 17/11/2017

Membres du jury :

Dr. KOBER Frank , Directeur de recherche CNRS, CMRBM, Marseille	Rapporteur
Dr. VAPPOU Jonathan, Chargé de recherche CNRS, ICUBE, Strasbourg	Rapporteur
Dr. DUMONT Erik , PDG de la société Image Guided Therapy, Pessac	Examinateur
Dr. QUESSON Bruno, Directeur de recherche CNRS, CRCTB, Bordeaux	Examinateur

Titre: Traitement non invasif des arythmies cardiaques par ultrasons focalisés de haute intensité guidés par imagerie de résonance magnétique

---

Résumé: Les ultrasons focalisés de hautes intensités ont la capacité de déposer de l'énergie ultrasonore localement et de façon non invasive dans les tissus biologiques. Il est possible d'exploiter les effets mécaniques et/ou thermiques en fonction des paramètres ultrasonores utilisés. Guidée par un système d'Imagerie de Résonance Magnétique, cette technologie se voit dotée d'une modalité de planification et le suivi en temps réel de la procédure. Les applications actuelles des ultrasons focalisés guidés par IRM sont sur des organes fixes, notamment le cerveau et l'os ou le fibrome utérin. Dans le cas du cœur, d'une part la présence de mouvements cardiaques et respiratoires constitue une difficulté importante, tant pour le traitement ultrasonore (balistique) que pour l'IRM de température (artéfacts sur les images). D'autre part, la cage thoracique joue le rôle de barrière pour la propagation des ultrasons.

Dans ce travail de thèse, un ensemble de techniques nouvelles pour l'ablation et la stimulation cardiaque non invasive par ultrasons focalisés guidés par IRM ont été développées. Une première étude montre la faisabilité technique de contrôler le rythme cardiaque par des impulsions ultrasonores brèves dirigées vers le myocarde. L'influence des paramètres des impulsions ont été étudiés quantitativement sur cœur isolé battant puis in vivo sur un modèle préclinique. Pour cela, un dispositif original a été développé. Une seconde étude présente des nouvelles méthodes rapides d'IRM permettant de cartographier simultanément la température et le déplacement local induit par les ultrasons focalisés. La méthode est validée sur le foie sur un modèle préclinique et démontre qu'il est possible de corréler la dose thermique obtenue par thermométrie IRM à un changement des propriétés mécaniques des tissus traités mesurés simultanément.

Une troisième étude a consisté à développer une technique de mesure de position de la cible en 3D temps réel par quelques éléments de l'émetteur ultrasonore opérant en réception. Cette mesure permet de corriger dynamiquement la position du foyer ultrasonore pour maximiser le dépôt d'énergie au point ciblé, le tout monitoré par thermométrie IRM temps réel à une cadence de 10 images par seconde. Là encore une validation préclinique est présentée. Ce travail de thèse propose donc des avancées importantes pour lever les verrous actuels de la technologie permettant d'envisager des traitements non invasifs des pathologies cardiaques par voie non invasive, le tout guidé par IRM en temps réel.

Mots clés : coeur, ultrasons thérapeutiques, imagerie par résonance magnétique

Title: Non-invasive treatment of cardiac arrhythmias by high-intensity focussed ultrasound guided by magnetic resonance imaging

---

Abstract: High intensity focused ultrasound has the ability to deposit ultrasonic energy locally and non-invasively into biological tissues. It is possible to exploit the mechanical and/or thermal effects according to the ultrasonic parameters used. Guided by a Magnetic Resonance Imaging (MRI) scanner, this technology is equipped with a planning modality and real-time monitoring of the procedure. As of now, applications of MRI-guided focused ultrasound are on fixed organs, including brain and bone or uterine fibroid. For the heart, the presence of cardiac and respiratory movements constitutes an important difficulty, both for the ultrasonic (ballistic) treatment and for the temperature monitoring under MRI (artefacts on images). In addition, the rib cage acts as a barrier for the propagation of ultrasounds.

In this thesis work, a set of new technological development have been developed for ablation and non-invasive cardiac stimulation using focussed MRI-guided ultrasound. A first study shows the technical feasibility of controlling heart rhythm by short ultrasound pulses targeted to the myocardium. The influence of the parameters of the pulses (duration, amplitude, emission time in the cardiac cycle) were studied quantitatively on isolated beating heart then in vivo on a preclinical model. For this, an original device was developed. A second study presents new rapid MRI methods for simultaneously mapping the temperature and local displacement induced by focused ultrasound. The method is validated on the liver on a preclinical model and demonstrates that it is possible to correlate the thermal dose obtained by MR-thermometry with a change in the mechanical properties of the treated tissues measured simultaneously.

A third study consisted in developing a technique for measuring the position of the target in 3D real-time using some elements of the ultrasonic transmitter as receivers. This measure allows to dynamically correct the position of the ultrasonic focus to maximize energy deposition at the targeted point. In addition, we monitored in real-time the procedure using MR-thermometry at a rate of 10 images per second. Here again a preclinical validation is presented. This thesis work proposes important advances to remove the current locks of the technology allowing to envision non invasive treatments of cardiac pathologies, all guided by MRI in real-time.

Keywords: heart, therapeutic ultrasounds, magnetic resonance imaging

Unité de recherche

LIRYC - L'Institut de Rythmologie et Modélisation Cardiaque.

Centre de Recherche Cardio-Thoracique de Bordeaux - INSERM U1045

Avenue du Haut Lévêque, 33600 Pessac

REMERCIEMENTS

A l'issue de la rédaction de ce travail de recherche, je suis convaincu que la thèse est loin d'être une "course en solitaire". En effet, je n'aurais jamais pu réaliser ce travail doctoral sans le soutien d'un grand nombre de personnes dont les compétences, la générosité, la bonne humeur et l'intérêt manifestés à l'égard de ma recherche m'ont permis de toujours progresser, d'apprendre et d'avancer.

En premier lieu, je tiens à remercier mon directeur de thèse, M. BRUNO QUESSON, et le directeur de la société Image Guided Therapy, M. ERIK DUMONT. Je remercie M. BRUNO QUESSON pour la confiance qu'il m'a accordée en acceptant d'encadrer ce travail doctoral, pour ses multiples conseils et pour toutes les heures qu'il a consacré à ma recherche. Il aura été d'une grande aide dans les moments de rédaction mais également durant les expérimentations et ce, jusque tard le soir. Je tiens également à le remercier pour la liberté d'initiative qu'il m'a accordé toute au long de ce travail doctoral. Je remercie M. ERIK DUMONT pour m'avoir apporté un soutien logistique et de nombreuses réponses aux questions techniques que j'ai pu rencontrer tout au long de ce travail de recherche. Aussi, je remercie l'ensemble des employés de la société, qui m'ont prodigué conseils et qui ont pu apporter des solutions concrètes à mes problèmes.

Mes remerciements vont également à FABRICE MARQUET, post-doctorant dans l'équipe imagerie pour avoir partagé ses connaissances dans le domaine des ultrasons et plus largement. Il m'a aidé sur l'ensemble du travail réalisé durant cette thèse. Il a pu répondre à mes interrogations et les discussions scientifiques que l'on a pu avoir durant cette thèse m'ont beaucoup apporté.

Je tiens ensuite à remercier VALERY OZENNE, SOLENN TOUPIN, MATTHIEU LEPETIT-COIFFE et MARYLENE DELCEY, qui ont partagé mon bureau durant ces 3 années. L'alternance de nos discussions scientifiques et d'autres, un peu moins, ont rythmé ce travail et l'ont rendu très convivial. Enfin, je tiens à remercier l'ensemble de l'équipe imagerie pour le partage de connaissances et les moments divers que nous avons partagés.

Je tiens à remercier toutes les personnes qui, de près ou de loin, m'ont prodigué con-

seils et soutiens, tout au long de ce travail de thèse.

Je souhaiterais exprimer ma gratitude au Pr. MICHEL HAISSAGUERRE, directeur du laboratoire et chef du service de cardiologie - électrophysiologie et stimulation cardiaque du CHU de Bordeaux, ainsi qu'au Pr. OLIVIER BERNUS, directeur scientifique, pour m'avoir accueilli au sein de L'Institut de RYthmologie et de modélisation Cardiaque.

Merci également aux rapporteurs de ce travail de thèse, M. JONATHAN VAPPOU et M. FRANK KOBER. Les discussions et questions ont été très enrichissantes.

Je remercie ma famille, mes parents et ma sœur de m'avoir soutenue durant toutes ces années et d'avoir su s'intéresser à mon travail. Ils ont toujours cru en moi. Je remercie également mon parrain pour avoir assisté à la soutenance où j'ai pu concrètement montrer le travail que j'ai effectué durant ces trois années. Je remercie également tous les autres membres de ma famille qui ont pensé à moi lors de la soutenance.

Enfin je souhaite remercier l'ensemble de mes amis "Strasbourgeois": Roxane, Manon, Laura, Morgane, Thomas, Arnaud, Pierre, et bien-entendu Simon. Merci à toi d'avoir fait le déplacement et d'avoir "essayé" de me détendre avant la soutenance. Merci également d'avoir réalisé cette petite vidéo forte en émotions.

Pour finir, je souhaiterais remercier MARION, qui partage maintenant ma vie. Cette thèse fut l'occasion de te rencontrer et de ne plus te quitter. Ton amour et ton soutien quotidien m'ont beaucoup aidé, tu m'as donné le courage et la force de toujours persévérer.

Contents

$2D$	Two Dimensional
$3D$	Three Dimensional
RF	Radiofrequency

Heart

CRT	Cardiac Resynchronization Therapy
ECG	Electrocardiogram
EP	Electro-Physiology
HF	Heart Failure
LA	Left Atrium
LV	Left Ventricle
PVC	Premature Ventricular Contractions
RA	Right Atrium
RV	Right Ventricle

MR-imaging

EPI	Echo Planar Imaging
FOV	Field Of View
$GRAPPA$	Generalized Autocalibrating Partially Parallel Acquisitions
LTD	Lethal Thermal Dose
MEG	Motion Encoding Gradient
MR	Magnetic Resonance
$MRgHIFU$	Magnetic Resonance guided High Intensity Focused ultrasound
MRI	Magnetic Resonance Imaging
PRS	Proton Resonance Frequency Shift
$ssGE-EPI$	Single shot Gradient Echo Echo-Planar Imaging sequence
$ssSE-EPI$	Single shot Spin-Echo Echo-Planar Imaging sequence
TD	Thermal Dose
TE	Echo Time
TR	Repetition Time

Ultrasound

$ARFI$	Acoustic Radiation Force Impulse
$HIFU$	High Intensity Focused ultrasound
MI	Mechanical Index
PCD	Passive Cavitation Detection
US	Ultrasound

List of Figures

List of Tables

Résumés en français

Introduction

Les ultrasons focalisés de hautes intensités ont démontré leur intérêt dans le traitement non invasif d'organes ou de tissus pathologiques. Combinée à l'imagerie par résonance magnétique, cette thérapie peut ainsi être guidée (ciblage) et monitorée grâce à des méthodes, telles que le suivi de température sous imagerie par résonance magnétique ou encore le suivi du déplacement, induit par la force de radiation ultrasonore. Son application telle que mentionnée précédemment a été réalisée avec succès pour le traitement du rein, du foie, de l'utérus et du cerveau. Deux effets de l'action des ultrasons sur les tissus peuvent être exploités. Le premier vient de l'absorption de la puissance ultrasonore par les tissus qui engendre une élévation de température au niveau du foyer. Si l'augmentation de température est suffisante, les tissus se nécrosent et meurent. Ce processus est particulièrement intéressant dans les cas de cancers, en permettant de détruire les cellules cancéreuses de manière non invasive. Un second effet est l'action mécanique des ultrasons sur l'organe cible. Cette action vise à promouvoir des effets biologiques tels que la perméabilisation de la membrane endothéliale des vaisseaux sanguins ou encore l'excitation mécanique des membranes cellulaires, et ceci tout en préservant le tissu sous-jacent. Ces processus sont principalement dominés par des effets de cavitations où de petites bulles de gaz viennent créer des forces mécaniques oscillatoires au voisinage de la cible, au passage de l'onde ultrasonore. Dans la littérature, ce processus a été démontré comme permettant l'ouverture de la barrière hémato-encéphalique, la stimulation de certaines régions du cortex moteur ou encore le déclenchement de contractions non spontanées du cœur.

Jusqu'à présent, le cœur reste un organe très peu exploré par les ultrasons focalisés. Pourtant, plusieurs applications ont été proposées chez l'homme et/ou chez le petit animal, qui tendent à montrer l'intérêt des ultrasons dans certains traitements de maladies cardiaques. Durant cette thèse, nous avons ciblé deux applications : d'une part, l'ablation non invasive de régions pathologiques du cœur et d'autre part, la stimulation non invasive du cœur dans le cas de l'insuffisance cardiaque. Dans ce but, nous avons réalisé une première preuve de faisabilité de la stimulation cardiaque sur un modèle gros an-

imal. Cette étude préclinique a été suivie de deux développements méthodologiques : dans un premier temps, la validation d'une méthode de suivi simultané de température et de déplacement sous imagerie par résonance magnétique, compatible avec l'application cardiaque et dans un second temps, une méthode de correction 3D et temps réel du foyer ultrasonore.

Etude # 1

À l'heure actuelle, il n'existe pas de dispositif de stimulation cardiaque non invasif acceptable pour une utilisation prolongée chez des patients conscients. Depuis 2004, les ultrasons focalisés de hautes intensités ont été proposés et étudiés pour réaliser des stimulations à distance en utilisant la réversibilité du couplage électromécanique des cellules cardiaques. Dans cette étude, nous avons designé un dispositif de stimulation cardiaque extracorporelle et testé son efficacité et sa sécurité. Nous avons mené des expériences ex vivo et in vivo sur un modèle gros animal (cochon) pour évaluer les perspectives cliniques d'une telle technique, en se rapprochant le plus possible des contraintes anatomiques retrouvées chez l'homme. Le seuil de stimulation cardiaque a été déterminé sur 10 cœurs ex vivo différents (pression acoustique nécessaire de 4 MPa). Différents effets électriques, cliniquement pertinents, tels que des stimulations consécutives de différentes chambres cardiaques avec une seule sonde ultrasonore, une stimulation continue ou l'induction de tachycardies ventriculaires ont été montrés. En utilisant un agent de contraste ultrasonore, la stimulation cardiaque s'est avérée reproductible in vivo pour des séances allant jusqu'à 1 heure, sur 4 animaux différents. Aucune lésion n'a pu être observée sur l'imagerie de résonance magnétique réalisée in vivo sur les 4 animaux. L'analyse histologique n'a révélé aucune différence entre les régions stimulées et les régions contrôles, pour tous les cas ex vivo et in vivo.

Dans la perspective du transfert vers le patient, différents axes de recherches restent à explorer. D'une part, le design d'une sonde ultrasonore dédiée aux applications cardiaques, de manière à optimiser la dépose d'énergie et ainsi éviter l'injection d'un agent de contraste ultrasonore. D'autre part, des études sur la fréquence d'émission ultrasonore et sur la distribution de la dépose d'énergie dans le cœur est à envisager.

Etude #2

Actuellement, le critère d'arrêt d'une ablation réalisée par ultrasons de hautes intensités guidées par l'imagerie de résonance magnétique, est le dépassement de la dose ther-

mique létale du tissu ciblé. Bien que ce paramètre soit fortement corrélé à la viabilité du tissu, il apporte très peu d'informations sur les changements des propriétés mécaniques du tissu au cours de l'ablation. Dans cette étude, nous avons développé une nouvelle séquence d'acquisition, rapide et multi-coupes, qui permet de suivre simultanément l'évolution de la température et du déplacement des tissus ciblés. Une séquence d'imagerie echo-planar a été modifiée pour intégrer une paire de gradients d'encodage du mouvement, avec une polarité alternée à chaque répétition. Une première impulsion ultrasonore a été synchronisée sur le second lobe du gradient d'encodage de mouvement, suivi d'un tir continu pour induire une augmentation locale de la température. Cette méthode a été validée ex vivo dans le muscle et in vivo sur le foie de porc. La séquence utilisée est compatible avec l'application cardiaque. Les résultats de cette étude ont montré que pour des doses thermiques supérieures au seuil létal, l'amplitude de déplacement a été progressivement réduite au point focal de 21 % dans les muscles et de 28 % dans le foie. La valeur du déplacement est restée constante pour les valeurs de doses thermiques non létales. Ainsi, cette nouvelle séquence d'imagerie rapide donne une mesure en temps réel de la répartition de la température et du déplacement, en plus d'une information qualitative de l'élasticité du tissu apportée par la variation du déplacement. L'application de cette méthode sur le cœur, nécessite des modifications de la chaîne de traitement, qui ont été identifiées au cours de cette thèse mais également, une instrumentation adaptée pour le ciblage de cet organe.

Etude #3

Les traitements par ultrasons focalisés de hautes intensités, destinés aux organes mobiles (cœur, foie), nécessitent le verrouillage du faisceau ultrasonore sur le tissu ciblé, ceci, afin de maximiser l'efficacité du chauffage. Dans ce étude, nous proposons d'utiliser une technique autonome de correction en trois dimensions du mouvement, en utilisant le transducteur ultrasonore en mode pulse-écho. La validation de cette méthode a été effectuée in vitro et in vivo dans le foie de porc en monitorant l'élévation de température sous imagerie par résonance magnétique. L'estimation du mouvement a été réalisée en utilisant la corrélation temporelle de deux signaux radiofréquences consécutifs, rétrodiffusés par le speckle du tissu ciblé. Le déplacement a été ainsi estimé selon quatre sous-ouvertures du transducteur ultrasonore, en calculant la corrélation croisée des signaux rétrodiffusés suivie d'un algorithme de triangulation. La position du faisceau ultrasonore a ensuite été déplacée pour compenser le mouvement, et l'énergie perdue par déflection électronique

a été corrigée. Ce processus a été contrôlé par thermométrie temps-réel sous imagerie par résonance magnétique (jusqu'à 5 coupes toutes les 700 ms, en utilisant la méthode de changement de la fréquence de résonance de protons en fonction de la température, combinée à une compensation de mouvement en ligne et à une correction des artefacts de susceptibilité magnétique associés). Un écho navigateur positionné selon l'axe principal de déplacement, a été utilisé pour évaluer la qualité de la correction de mouvement proposée. Les résultats obtenus par l'estimation du déplacement étaient en bon accord avec le signal de l'écho navigateur. In vitro, l'augmentation maximale de la température a été améliorée de 38 % par rapport aux expériences réalisées sans correction de mouvement et la répartition de la température est restée beaucoup plus localisée. Des résultats similaires ont été montrés in vivo, avec une augmentation de 34 % de la température maximale à l'aide de ce verrouillage de la position du foyer ultrasonore. Cette technique autonome de correction de mouvement 3D, basée sur le signal ultrasonore, s'est montrée robuste pour des mouvements respiratoires, tout en offrant une grande flexibilité sur la paramétrisation de la séquence de thermométrie. Les résultats in vitro et in vivo ont montré environ 35 % d'amélioration de l'efficacité du chauffage lorsque la position de focalisation est verrouillée sur la cible en utilisant la technique proposée. La faisabilité de cette méthode pour une application cardiaque reste à être démontrée.

Conclusion et perspectives

Le traitement du cœur à l'aide des ultrasons focalisés est un grand défi car il combine deux limitations bien connues de l'application des ultrasons : à savoir, les mouvements physiologiques et une fenêtre acoustique limitée. Au cours de ce travail de thèse, nous avons identifié deux applications potentielles d'ultrasons thérapeutiques utilisant des approches totalement non invasives. Premièrement, les ablations cardiaques en cas d'arythmie et, deuxièmement, la stimulation cardiaque en cas de bradycardie ou d'asystolie. La première étape consistait à valider les développements méthodologiques en imagerie de résonance magnétique, requis pour la surveillance des procédures ultrasons de hautes intensités, sur le cœur.

Malgré l'intérêt évident de ces deux méthodes pour les applications cardiaques des ultrasons thérapeutiques, leurs validations sur le cœur n'ont pas été possibles dans le calendrier de cette thèse. La principale limitation a été la conception de notre dispositif d'ultrasons focalisés qui n'a pas pu fournir une puissance acoustique suffisante pour le traiter. Néanmoins, pour les deux méthodes, nous avons identifié des points de

développement précis pour rendre possible leurs applications.

La preuve de faisabilité de la stimulation cardiaque a pu être faite in vivo avec le système d'ultrasons focalisés à disposition. Nous avons pu évaluer la pertinence d'une telle technologie, ses possibilités et ses contraintes. Cette étude nous a également permis de valider des moyens de suivi du traitement en monitorant par exemple le déplacement et les effets de cavitation. Là aussi, des points clés dans l'amélioration du système ont été identifiés.

CHAPTER 1

Introduction

Contents

1.1 Magnetic Resonance Imaging guided HIFU

Magnetic Resonance-guided High Intensity Focused Ultrasound (MRgHIFU) combines two modalities: a therapeutic ultrasound device (HIFU) and MRI as a planning and monitoring system. MRgHIFU is seen as a promising method for the non-invasive treatment of

pathological tissues, and has already been evaluated for numerous pathologies [1]. Under MRI, these procedures can benefit from 2D/3D imaging to localization the transducer and monitor the energy deposition. In addition, an excellent soft tissue contrast is provided by MRI, which helps to precisely target the tissue of interest (tumor, organ). During therapeutic ultrasound delivery, MRI allows real-time monitoring of biomarkers such as the temperature (MR-temperature) [2] and/or the displacement induced at the focus by the acoustic radiation force (MR-ARFI) [3]. These biomarkers are particularly interesting to monitor during HIFU treatments as they characterize the results of ultrasound interactions with the tissue, which can be used to improve the treatment efficacy and safety. At the end of the procedure, MR-imaging with or without injection of contrast agent can highlight the treated area [4]. MRgHIFU applications can be coarsely divided in two categories: one employing thermal effects of ultrasounds and another using mechanical effects. We will illustrate both strategies on the brain, where these effects have been extensively explored under MR-guidance.

Thermal effects: Absorption of ultrasound energy by soft tissues leads to local heating at the focal point of the transducer. The increase of temperature follows the Bioheat transfer equation:

$$\rho C_t \frac{\partial T}{\partial t} = K_t \nabla^2 T - W_b C_b (T - T_b) + Q_m + Q_v \tag{1.1}$$

Where ρ ,C_t, and K_t are the density, specific heat capacity, and thermal conductivity of the tissue respectively, T is the temperature of the biological tissue, Tb is the temperature of blood, Q_m (often negligible) and Q_v are the rate of heat generation per unit volume due to the metabolism and ultrasound external heat source respectively, W_b and C_b are perfusion rate and specific heat capacity for blood,respectively. Q_v is related to tissue absorption of ultrasounds. Note that the ultrasound tissue absorption is defined by several parameters. It depends on the tissue, on its temperature and, on the operating frequency used for sonication [5].

During ultrasound delivery, temperature at the focus will increase depending on energy delivery. If the accumulated heating reaches a threshold defined as a lethal thermal dose [6], biological changes occur at the cell level and irreversible cells damages can be induced, resulting in a coagulation necrosis. Several applications exploit this energy deposition to resect pathological tissues which was sucessfully demonstrated on the brain, muscle, liver, breast and pancreas [7]. For instance, Figure

1.1 (Graphical interface of Insightec^{TM} software) shows a real-time monitoring of MR-Thermometry during an MRgHIFU procedure on the brain. This treatment consists in ablating a pathological region of the brain causing essential tremors to the patient. In this procedure, a low temperature increase (< 4 °C) is used to localize the focus position, and during the ablation, the temperature evolution defines the therapy end-point.

In terms of sonication patterns, thermal effects often require high sonication duty cycles and high acoustic powers, in order to compete with cooling factor such as the perfusion (see $W_b C_b$ term in equation 1.1). For moving organs, motion correction of the position of the focus is often mandatory to preserve surrounding tissues and enhance the heating efficiency at the desired location [8, 9, 10, 11, 12].

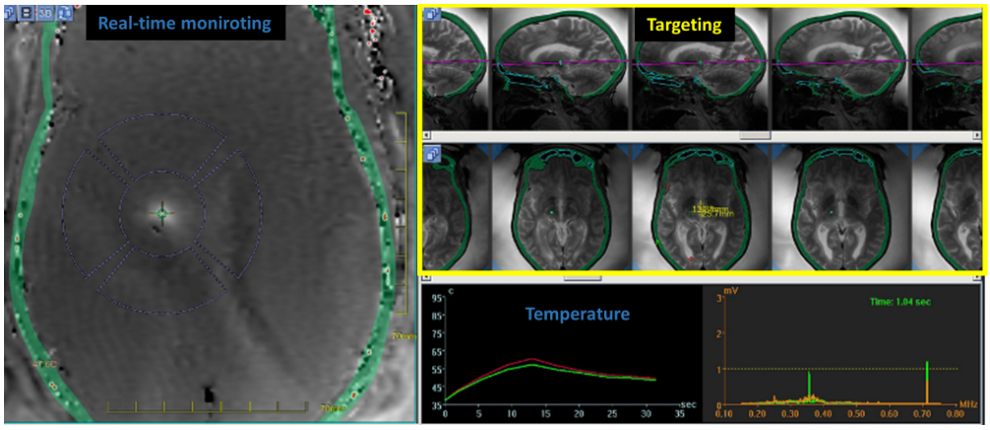

Figure 1.1: Screenshot of a focused ultrasound brain sonication showing anatomical and real-time thermal data.

Mechanical effects: This strategy exploits the ultrasound cavitation effects to promote bioeffects, while preserving the underlying tissue. Acoustic cavitation mediates US's tissular effects through three potential mechanisms [13]. One of these mechanisms is microstreaming. It describes the transmission of shear stress from fluid motion generated by oscillating bubbles at the ultrasound frequency, to cell membranes and endothelial surfaces (stable cavitation). Another mechanism is jetting from asymmetric collapse of a bubble (inertiel cavitation). Jetting of bubbles from vessel lumen into tissue, or from tissue into the lumen, can potentially increase vascular permeability and allows therapeutic agents to enter the cells. Cells permeability may also be enhanced by expanding and compressing bubbles in direct contact with its surface. Even-though mechanical effects tend to preserve the underlying tissue, these mechanisms could also lead to soft tissue damages when inertial cavitation becomes predominant. This is particularly the case during jetting, where temperature and

local pressures can reach extreme values.

However, with careful titration of US parameters, non-thermal effects can be exploited for therapeutic purposes. Compared to thermal effects, mechanical effects usually involves low/medium acoustic power deposition. In the literature, it has been shown to promote beneficial bioeffects such as drug delivery [14], thrombolysis [15, 16], disruption of the blood brain barrier [17, 18], cardiac stimulation [19, 20] and neuro stimulation [21, 22].

As of today, mechanical and thermal applications of MRgHIFU on the brain are clearly identified and their feasibility is now widely accepted. Other organs such as the heart, could also benefit from similar approaches (i.e. thermal and mechanical effects). The main objective of this thesis work is to develop methods and evaluate the feasibility of cardiac applications of therapeutic ultrasounds. MRI will be used for real-time targeting and monitoring as well as for safety assessments. We have tried during this work to target cardiac applications with a clear relevance in cardiology and with concrete clinical perspectives. The following of this chapter will give a quick overview on the heart and on cardiac electrophysiology. Then, based on clinical needs and possible gain for the patient, several applications of ultrasounds on the heart are presented.

1.2 The heart

The heart is composed of four chambers, two atria and two ventricles. The right heart collects the venous blood and sends it to lungs for blood reoxygenation.Then, the blood comes back in the left atrium and is transferred to the left ventricle in order to be expelled in rest of the body. The separation of atria and ventricles is made by valves in order to ensure the blood transfer into the different cavities (Figure 1.2).

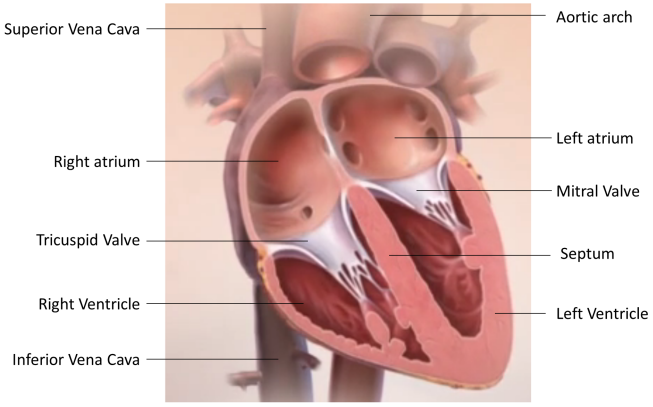

Figure 1.2: Anatomy of the anterior surface of the heart in cross section. The heart is divided into four heart chambers : two atria and two ventricles separated by the septum. LV ejects blood to the aorta to ensure blood perfusion of the body. The RV pushes blood through the pulmonary arteries to the lungs for blood reoxygenation.

1.2.1 Cardiac electrophysiology

The cardiac contraction of the heart is driven by the propagation of an electric wave. Cardiac electrophysiology (EP) is the study of this electrical system. The heart has a cardiac automatism which confers its properties of spontaneous and regular contraction at about 65-90 beats per minutes for an healthy patient at rest. In physiological conditions also referred as sinus rhythm, the electrical activity is initiated at the sinoatrial node (SAN) and propagates toward the atrioventricular node (AVN). During the propagation of the wave, cardiomyocytes of atria are successively electrically depolarized that triggers their mechanical contractions. Then the electrical wave follows the left and right bundle brunch and purkinje fibers in order to depolarize the ventricles (see Figure 1.3).

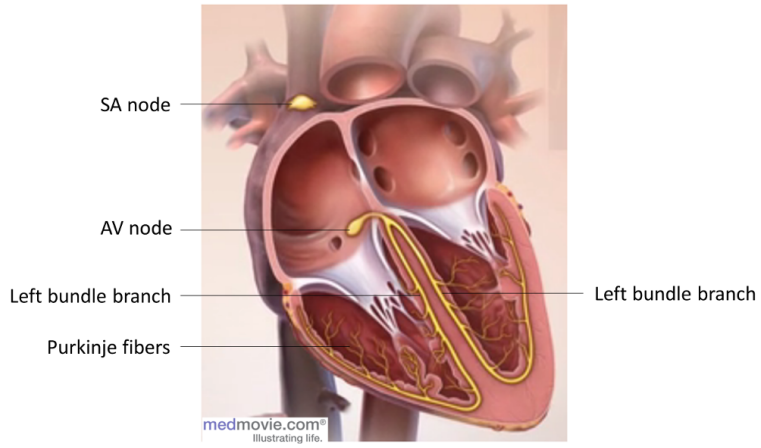

Figure 1.3: Electrical conduction system of the heart. Schematic representation of the heart chambers and conduction pathways. The home of cardiac automatism is at the SAN . The wave of depolarization spreads to both atria and converges to the AVN . Then, it propagates in the His bundle, which splits into two branches for each ventricle and arborizes in many branches called Purkinje fibers.

1.2.2 Electrocardiogram

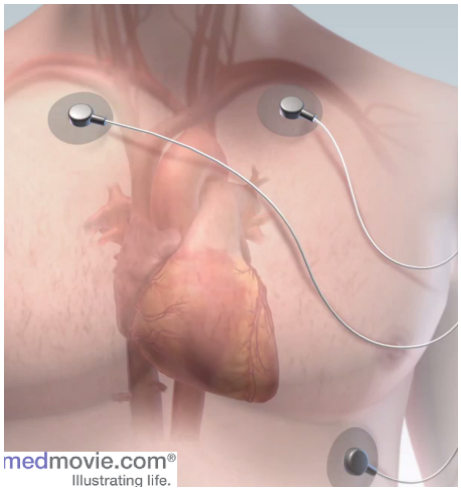

Figure 1.4: Position of three electrodes for ECG recording

There are numerous ways to explore cardiac electro-physiology, the gold standard electrophysiological exam in clinic being the 12 derivations ElectroCardioGram (ECG). However a simpler configuration is the two derivations ECG. It has the advantage of being non-invasive and easily achievable with the use of 3 electrodes positioned on the chest (see Figure 1.4). On the ECG trace the activity of the different cardiac chambers can be observed. The ECG trace is thus a good surrogate for cardiac activity. Figure 1.5 presents a schematic representation of one derivation of an ECG. Several peaks can be depicted: termed the P, Q, R, S and T waves.

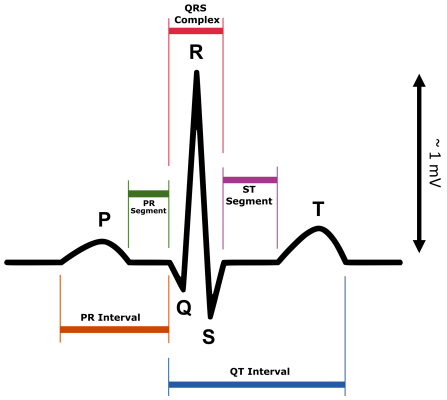

Figure 1.5: QRS complex. Schematic representation of an ECG recording

- **P wave** corresponds to the depolarization of the atria.
- **PQ or PR interval** represents the electrical conduction delay between the NAV and branches of the bundle of His.
- **QRS complex** depicts the depolarization of both ventricles. Note that repolarization of the atria occurs during this period of time and is often hidden by the

amplitude of the QRS complex.

- **ST segment** indicates the period during which the ventricular contractile fibers are completely depolarized and no depolarization can occur.
- **T wave** corresponds to ventricular repolarization. After this wave, the heart is in resting state before a new depolarization.

In the context of cardiac MRI, the ECG trace is used to synchronize the MR-acquisition on cardiac rhythm by detecting the R wave of the QRS complex (see Figure 1.5). If MR-acquisitions are fast and if they are always performed at the same time point within the cardiac cycle, the heart motion can be artificially frozen on resulting images. Note that cardiac contraction occurs predominantly during the QT interval, called systole, and the rest of the cardiac cycle, termed diastole, is the resting state of the heart. ECG gating in diastole is thus widely-used in cardiac MRI and in interventional MRI, as it can avoid motion of the target during treatment monitoring (see section 2.2.5.2 for more details).

Despite its good ability to characterize cardiac contraction state, the ECG trace turns out to be insufficient for a precise cardiac diagnosis. It only gives an "averaged" activity of the heart due to its non localized feature. In addition, the torso acts as low-pass filter, which avoids precise electrical activity measurement of the local depolarization/repolarization.

1.2.3 Catheters

To overcome the lacks of the ECG trace to perform precise electrophysiology measurements at the desired locations, cardiac catheters have been developed. Catheter are medical devices used to map electrical activity of the heart. The catheter is inserted under mini-invasive access inside vascular routes, in order to reach heart cavities. This procedure is routinely performed under x-ray guidance. To reach the LV or RV, the catheter can be inserted in the femoral artery or in the femoral vein, respectively. A catheter is usually made up of two to four electrodes but multiple electrodes systems are constantly developed to map more efficiently the 3D electrical activity of a cardiac chamber.

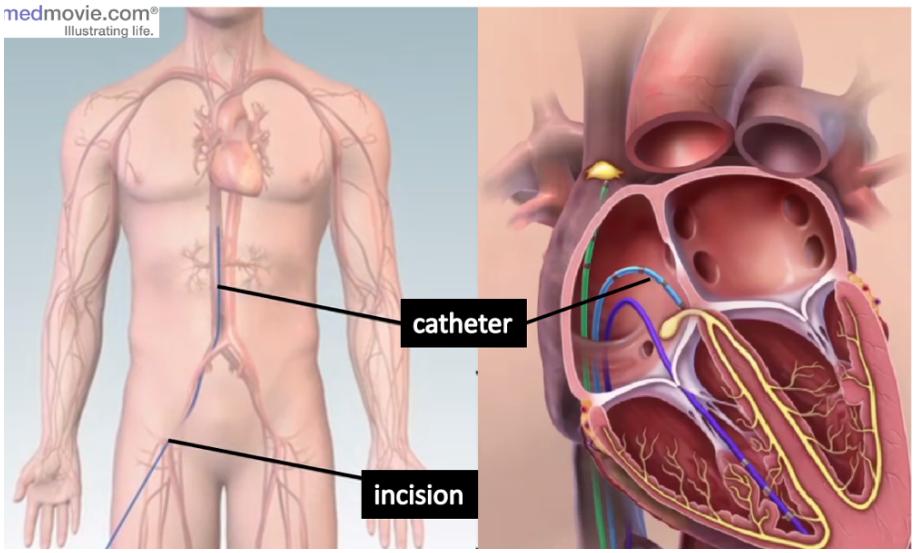

Figure 1.6: Electro-physiological catheter. The catheter is inserted in vascular routes to reach heart cavities. Once in contact with the cardiac wall, electric activity of this region can be measured.

1.2.4 Cardiac stimulation

In previous section (section 1.2.1), we have seen that cardiac contractions are induced by an electrical depolarization initiated by the SAN, which propagates to the rest of the heart. Similarly to the SAN, it is possible to induce a local depolarization anywhere in the heart by sending an external stimulus, such as an electrical impulse. Then, this local depolarization propagates, following the cardiac conduction pathways. To produce this local depolarization, an electrical lead can be inserted inside a cardiac cavity and put in contact with the cardiac wall. The other end is connected to a pacemaker (see Figure 1.8 D and F). Typical pulse settings to produce a stimulation are a duration of 1-2 ms and an amplitude of 5-10 Volts for the ventricles. Note that cardiac stimulation can only occur during a specific timing window in the cardiac cycle. When cardiomyocytes are depolarized (i.e. ST segment) no stimulation can be induced. This is called the refractory period (see red box on Figure 1.7). After the T wave, the cardiomyocytes are repolarized and can be stimulated again. This period is referred as the non refractory period (see green box on Figure 1.7).

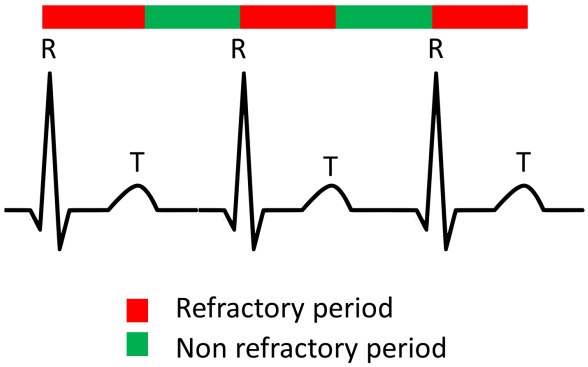

Figure 1.7: Refractory and non refractory periods. Red and green box represent the refractory period and the non refractory period, respectively.

It is possible to repeat this stimulation over several repetitions (at a fixed frequency). This procedure is called continuous cardiac pacing. If the pulse frequency is greater than the SAN activity, electrical impulses will overdrive the SAN activity and force the heart to beat a the same frequency. In clinic, pacing can be performed on the atria, on a single ventricle or on both ventricles (see Figure 1.8A,B and C).

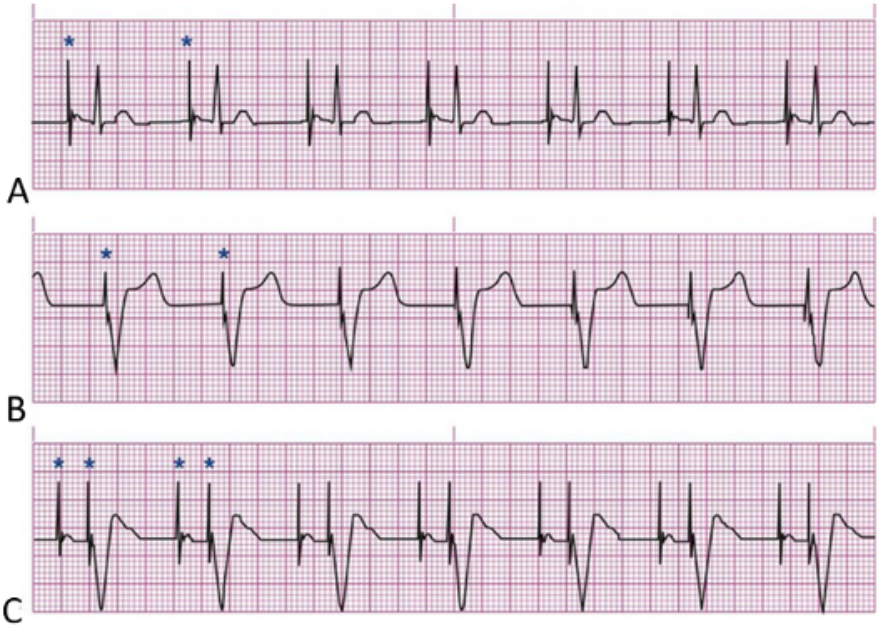

Figure 1.8: Pacing examples. A, Atrial pacing. B, Ventricular pacing. C, Dual-chamber pacing (atrial and ventricular pacing). Each asterisk represents a pacemaker impulse.

1.2.5 Abnormal conduction pathways

As described in section 1.2.1, for healthy subjects, the electrical conduction pathway is well organized and regular. However in pathological conditions, the heart conduction pathways can be deeply modified, altering its capacity to pump blood to the rest of the body. Origins of arrhythmias are numerous: it can involve arythmogenic subtrates [23],

conduction abnormalities [24] or can result from environmental factors. Figure 1.9 shows different types of ventricular arrhythmias:

Tachycardia corresponds to a increase in heart rate.

Fibrillation is a complete and permanent disorganized electrical activity of the heart. In this condition, the heart does not pump blood anymore and its defibrillation is the only way to restore the cardiac function.

Heart failure occurs when the heart is unable to pump blood sufficiently to maintain blood flow to meet the body's needs. Common cause of heart failure is ventricular dyssynchrony. This cardiomyopathy is diagnosed in patient with a QRS complex larger than 120 ms and reduced ejection fraction (lower than 35 %).

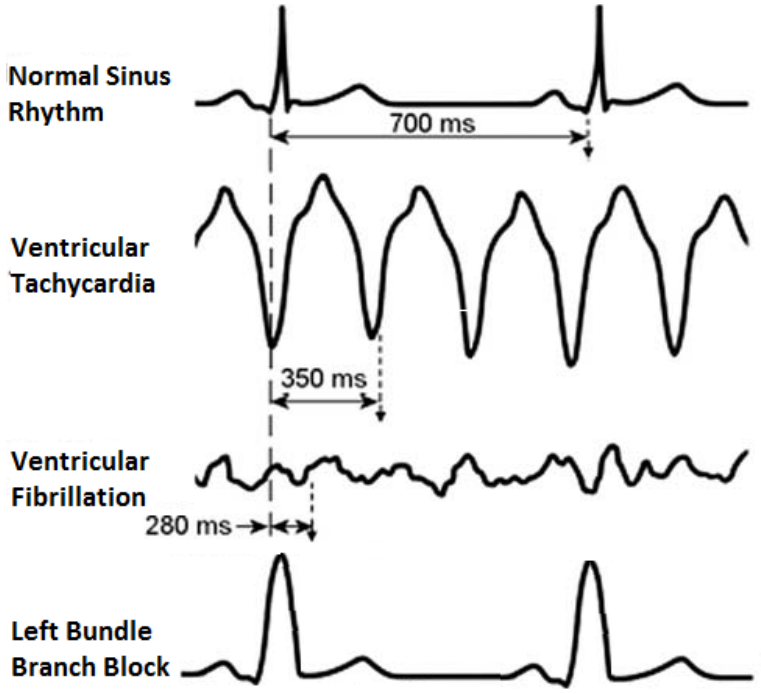

Figure 1.9: Examples of cardiac arrhythmias. ECG recordings in sinus rhythm (A), during a ventricular tachycardia episode (B) and ventricular fibrillation (C).

Atrioventricular block is a failure of the AVN. The conduction pathway from the atria to the ventricles is not functional anymore. Patients suffering from this disease have often a slow and irregular rhythm which results from the capacity of regions in the ventricles to trigger local depolarizations (ectopic foci). This rhythm is called the escape rhythm. Due to the severe bradycardia, these patients are often in really bad conditions.

Cardiovascular disease is the first cause of mortality in the whole world. In 2008, the world health organization reported that it is responsible for 29% of deaths, followed

by infectious diseases (16.2%) and cancers (12.6%)1. The economic burden related to cardiac diseases will grow with the ageing European population making cost management of Public Health more challenging.

1.3 Potential applications of HIFU on the heart

1.3.1 Application 1: Cardiac ablation

1.3.1.1 Clinical context

Radiofrequency ablation is a medical procedure used in cardiology for the treatment of a number of cardiac rhythm disorders and complements antiarrhythmic drug therapies. This surgical procedure consists in eliminating ectopic depolarisation foci (local depolarization) or undesired conduction pathways. To this end, a catheter is inserted in contact with the myocardium, under X-ray guidance to burn the abnormal conductions sites. For the treatment of atrial tachysystolia or certain ventricular tachycardias, a preliminary step consists in mapping the electrical activity of the heart using catheters to identify pathological regions. Then, a 3D rendering of parametric electrical signals (amplitude, frequency,...) is performed on a dedicated software (Figure 2-E) such as NavX (St Jude Medical, St Paul, MI, U.S.A.) or CARTO (BiosenseWebster, Diamond Bar, CA, U.S.A.), in order to assist the clinician during the ablation. The therapeutic outcome of the ablation depends highly on the identification of origin sites of the arrhythmia.

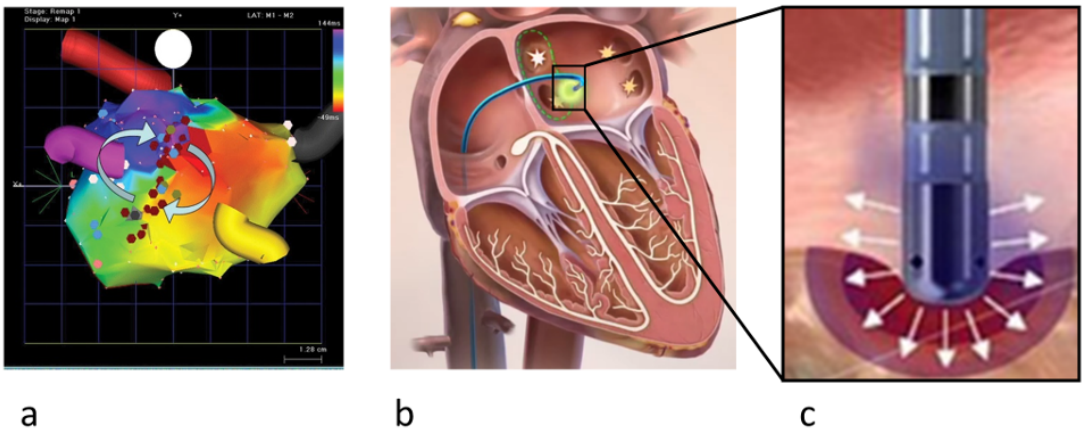

Figure 1.10: Radiofrequency ablation. a) 3D mapping of an artia using a CARTO. Red dots represent the ablation points. b) Isolation of pulmonary veins using a catheter inserted in the heart cavity. c) Schematic representation of an radiofrequency ablation procedure

1.3.1.2 MRgHIFU for cardiac ablations

As for now, combining an HIFU device and MRI for cardiac ablations is a major step forward compared to the current patient care or even current preclinical studies. However, their gains for the improvement of ablation therapies have been demonstrated independently. For instance, studies have inverstigated HIFU ablations under X-ray [25, 26], and some others have monitored the temperature evolution during radiofrequency ablation under MRI[27, 28, 29]. Combining both methods could potentially bridge therapeutic dead-ends and provide the operator with new information on the intervention process.

MR-monitoring versus X-ray guidance: Compared to X-ray, MRI has a greater soft tissue contrast, which allows precise targetting of the pathological cardiac tissue. In addition, as proposed by De Senneville et al. [28] real-time monitoring of the procedure could be performed using MR-thermometry, which has proven its ability to predict the lesion size, while controlling the energy delivered. Finally, 3D post-ablation imaging can attest the extension of the lesion and could give insights of the need of other ablation point. As of now, MRI is the only imaging modality that provides imaging at every stages of the ablation procedure.

HIFU versus radiofrequency ablation Compared to radiofrequency ablation, HIFU ablation has the possibility to target deeper cardiac tissues and can be made non-invasive (see epicardial catheter ablation on Figure 1.11, extracted from [26]). As shown in Figure 1.11, for radiofrequency ablations the catheter tip has to be in contact with the tissue to deliver the electric power. As a consequence, the lesion enlarges from this contact (see Figure 1.10c) with limited ability to reach the other side of the cardiac wall for cardiac wall thickness of 1 cm and more in the LV. In this context, common strategies to improve lesion sizes are: to increase electric power delivery and/or lengthen the ablation duration. These strategies are accompanied with possible adverse effects which are: induction a coagulum, which prevents deeper ablations, or increase the risk of steam pop resulting in cardiac perforations [30]. Also note that application of radiofrequency energy on the epicardium is often limited by epicardial fat that reduces electrical current intensity, or proximity to the phrenic nerve or coronary arteries present on the epicardium [31]. The hot spot generated by an HIFU ablation is located at the focus of the transducer, without the need of a physical contact with the cardiac tissue to be treated. The only requisite is an ultrasound coupling, from the transducer to the target. As shown by 1.11, HIFU

ablation shapes could be more suited to perform transmural ablations or target the endocardium or the epicardium, respectively.

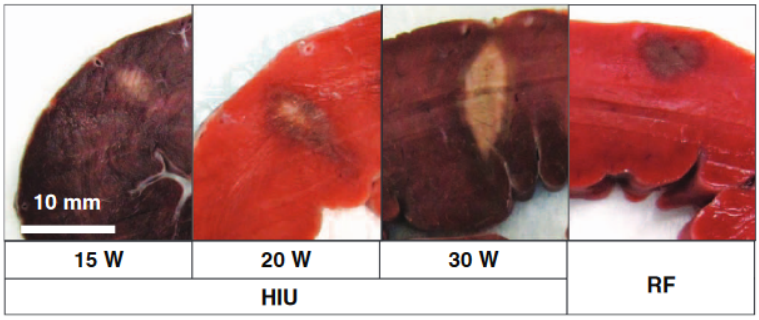

Figure 1.11: Ablation comparison Representative high-intensity ultrasound (HIU) and radiofrequency (RF) epicardial lesions. Triphenyl-2H-tetrazolium chloride–stained cross-sections of left ventricular myocardium shown with epicardial surface on top.

Technological considerations apart, cardiac ablations under MRI using an external HIFU device could allow non-invasive ablation of cardiac muscle, while providing biomarkers monitoring such as temperature and/or displacement. Finally, post-ablation imaging would attest the resulting lesion extension from consecutive individual ablations

1.3.2 Application 2: Heart failure and cardiac pacing

1.3.2.1 Clinical context

Current patient treatment for heart failure consist in electrical pacing of the heart using a pacemaker. To this end, a surgical approach is done under x-rays guidance to insert electrical leads into heart cavities (see Figure 1.12). Lead placement depends on the patient disease but most often a lead is placed in a coronary sinus for LV pacing in addition to a conventional RV endocardial lead. This therapy is referred as the resynchronization therapy [32]. In France, patients suffering form heart failure in 2001 were 500 000, with 120 000 new cases each year [33].

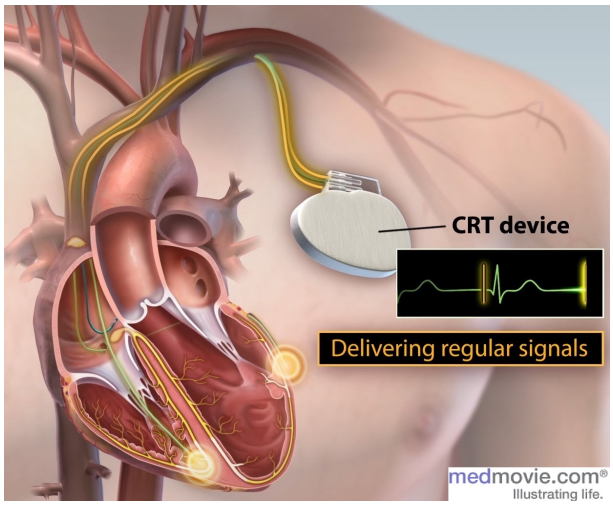

Figure 1.12: Pacemaker implantation. One lead is placed in the right ventricle. A second one inserted in the coronary sinus, passing though the right atria, for left ventricular pacing.

This procedure is currently the gold-standard for the treatment of this disease. Even though clear improvement of patient condition have been demonstrated, there are still 1/3 whom are non-respondent. In addition, several limitations are inherent to this surgical procedure:

- Newborn patients and patients with infections cannot be implanted.
- Operating room and medical staff have to be available. This can be problematic when patients arrive in emergency.
- During pacemaker replacement, patient is not paced anymore.

As of now, for clinical contraindications mentioned earlier, temporary pacing has to be performed to prevent patients death. Indeed, the two most common reasons for using temporary pacing is to maintain an optimal cardiac output when patients have developed a symptomatic bradycardia or are asystolic. Two temporary pacing methods are currently available in clinic [34]:

Temporary pacing using a catheter. An electrical lead is inserted through vascular routes to pace the heart [35]. However, several complications are observed during long duration catheter pacing. The two greatest are: a loss of capture as the catheter in not in contact with the myocardium, and the risk of heart perforation if the catheter is inserted too far into the cavity.

Transcutaneous cardiac electrical pacing. This procedure consists in stimulating the heart using electrodes positioned on the patient's chest [36, 37]. Simulation in this manner, is often not well accepted by patient due to discomfort of muscle stimulation.

1.3.2.2 Non-invasive cardiac pacing using HIFU

One application of mechanical effect of ultrasounds on the heart is to produce premature cardiac contractions [19, 20]. Its application would benefit highly in clinical cardiology and electro-physiology as it would allow non-invasive stimulation of targeted areas of the myocardium using an extra-corporeal non electric energy and could be used for diagnostic as well as therapeutic purposes. Such an ultrasound system, with all of its components external to the body, would not require any surgical or catheterization procedures, implanted receivers, or intra-vascular leads. It could hence, dramatically reduce device related complications, including vascular rupture, infection, and need for extraction.

1.4 Challenges of cardiac application of HIFU therapies

During this thesis, we have envisioned fully non-invasive applications of therapeutic ultrasounds on the heart. Two applications are targeted: non-invasive cardiac ablation and non-invasive cardiac stimulation. However fully non-invasive cardiac applications of ultrasounds are particularly challenging as they combine two well-known limitations of ultrasounds: namely motion of the target and the capacity of ultrasounds to propagate through the thoracic cage.

1.4.1 Motion

The motion of the heart is complex and has two main components: one due to the respiration and an other due to cardiac contractions. Both motion components are asynchronous with different amplitudes, directions and speeds.

1.4.1.1 Respiratory motion

The heart lays upon the liver which moves with the respiration due to inhalation and exhalation of air in lungs. Breathing induces predominantly a translation of the heart in the head-feet direction at a rate ranging from 10 to 15 breaths per minute with amplitudes from 1 to 2 cm [38].

1.4.1.2 Cardiac motion

Cardiac contractions occur at about one beat per minute. As compared to respiratory motion, cardiac motion is more complex. There are three components of motion in cardiac contraction: first a radial and longitudinal component of contraction combined with a twist along its longitudinal direction [39]. Note that the heart is at resting state during a limited period of time, around 200-300 ms during the diastole.

1.4.2 Anatomical structures and acoustic windows

Many anatomical structures, with very poor ultrasound propagation capabilities, are included in the beam path, before reaching the heart. The main constrain is the thoracic cage, which surrounds the heart and acts as an aberration, decreasing the focusing quality of the ultrasonic beam [40, 41]. Other organs such as lungs, positioned from each side of the heart, and on its posterior side, reduce even more the acoustic window available. In summary, only intercostal acoustic windows could propagate ultrasound waves with a good efficiency. Nevertheless, the acoustic window varies greatly during respiratory cycle and also change according to the position of the patient. This adds more complexity to target a precise location of the heart.

1.4.3 Review of cardiac therapeutic ultrasound

Cardiac applications of therapeutic ultrasounds have been explored since early 90's. Table 1.1 sums up some of cardiac applications of HIFU, divided in two categories: thermal applications and mechanical applications.

Cardiac ablation using HIFU could potentially bridge current limitations of radiofrequency ablations (as introduced in section 1.3.1.2). However, only two studies have demonstrated the feasability of a fully non-invasive cardiac ablation in vivo, in dog [42, 43]. This observation highlights the complexity of non-invasive approaches on the heart (limited acoustic window, anatomical structures, motions). This is all the more so, when long duration HIFU exposures are required. In others in vivo studies, a mini-invasive approach is preferred (Trans-oesophagus [44] or catheters [26]) or midline sternotomy [45]. These approaches allow to circumvent transthoracic sonications and optimize the ultrasound power deposition. Nevertheless, catheter apart, ultrasound ablations might remain suboptimal in absence of physiological motion compensations and real-time update of the focus position.

Several mechanical applications of ultrasounds have been proposed in the literature. Overall, they also suffer from the same aforementioned limitations. Note that some applications such as the treatment of thrombolysis or angiogenesis [46, 47], tend to be cumulative over sonication repetitions. In these cases, the delivery of therapeutic ultrasounds should hence be easier to achieve. For cardiac stimulations, several studies have investigated the feasibility on small animal models. Nevertheless, given the acoustic power needed to depolarize the heart, it may require some ingenuity and technological developments to translate this application toward large animal models.

	Authors	Methods
Thermal effect	Bessiere et al. 2016 [44]	In vitro Trans-oesophagus prob for cardiac ablation
	Zheng et al. 2014 [42]	In vivo (dog) HIFU myocardial ablation and biological response
	Laughner et al 2012 [48]	Ex vivo HIFU myocardial ablation on wedge prep
	Schopka et al. 2010 [45]	In vivo (Humain patients) AF ablation with ultrasound probe
	Strickberger et al. 1999 [49]	Ex vivo HIFU myocardial ablation
Mechanical effect	Unger et al. 2014 [14]	Cardiovascular drug delivery with ultrasound and microbubbles (clinical trial)
	Livneh et al. 2014 [19]	In vivo (rat) cardiac stimulation and passive cavitation detection
	Hanawa et al. 2009 [47]	Pulsed Ultrasound Induces Angiogenesis and Ameliorates Left Ventricular Dysfunction (pig)
	Wright et al. 2012 [46]	In vitro and in vivo HIFU thrombolysis (rabbit)
	Dalecki et al 1991 [50]	In vivo (frog) cardiac stimulation

Table 1.1: Publications in the field of cardiac applications of therapeutic ultrasounds

1.5 Context of this thesis

This thesis was granted by the company Image Guided Therapy via a CIFRE contract with "L'Institut de RYthmologie et Modélisation Cardiaque" in Pessac. This institute is one of the six "Institut Hospitalo-Universitaire" in France, and it is dedicated to heart diseases. The bulk of the thesis work, focused on the application of MRgHIFU on the heart using fully non-invasive HIFU devices. At the beginning of the thesis, an HIFU

device and an MRI were available but without any technological development toward this application. The thesis can be coarsely divided in two parts.

Cardiac stimulation: Investigation of the clinical applications of using HIFU to perform non-invasive cardiac stimulation in a preclinical large animal model (**Chapter 3**).

Methodological developments: These developments were required for non-invasive cardiac ablation and stimulation. It consisted first, in novel monitoring methods combining MR-temperature and MR-ARFI (**Chapter 4**) for ablations monitoring and/or safety assessments. The second methodological development concerned the management of the physiological motions during MR-thermometry monitoring and correction of the focus position for MRgHIFU applications on moving organs (**Chapter 5**).

1.6 References

[1] Jean-Michel Escoffre and Ayache Bouakaz, eds. *Therapeutic Ultrasound*. Advances in Experimental Medicine and Biology. Cham: Springer International Publishing, 2016.

[2] Bruno Quesson et al. "Real-time volumetric MRI thermometry of focused ultrasound ablation in vivo: a feasibility study in pig liver and kidney". en. In: *NMR in Biomedicine* (Feb. 2011).

[3] Nathan McDannold and Stephan E. Maier. "Magnetic resonance acoustic radiation force imaging". In: *Medical Physics* (2008).

[4] T. Leslie et al. "High-intensity focused ultrasound treatment of liver tumours: post-treatment MRI correlates well with intra-operative estimates of treatment volume". en. In: *British Journal of Radiology* (Jan. 2012).

[5] P. N. T. Wells. "Absorption and dispersion of ultrasound in biological tissue". In: *Ultrasound in Medicine & Biology* (Mar. 1975).

[6] Stephen A. Sapareto and William C. Dewey. "Thermal dose determination in cancer therapy". In: *International Journal of Radiation Oncology*Biology*Physics* (Apr. 1984).

[7] Samantha Ellis et al. “Clinical applications for magnetic resonance guided high intensity focused ultrasound (MRgHIFU): Present and future: Clinical applications for MRgHIFU”. en. In: *Journal of Medical Imaging and Radiation Oncology* (Aug. 2013).

[8] Baudouin Denis de Senneville et al. “Real-time adaptive methods for treatment of mobile organs by MRI-controlled high-intensity focused ultrasound”. en. In: *Magnetic Resonance in Medicine* (Feb. 2007).

[9] Mario Ries et al. “Real-time 3D target tracking in MRI guided focused ultrasound ablations in moving tissues”. en. In: *Magnetic Resonance in Medicine* (Dec. 2010).

[10] W. Apoutou N’Djin et al. “An ultrasound image-based dynamic fusion modeling method for predicting the quantitative impact of in vivo liver motion on intraoperative HIFU therapies: Investigations in a porcine model”. In: *PloS one* (2015).

[11] Zarko Celicanin et al. “Real-time method for motion-compensated MR thermometry and MRgHIFU treatment in abdominal organs: MRgHIFU Treatment Method in Abdominal Organs”. en. In: *Magnetic Resonance in Medicine* (Oct. 2014).

[12] Philippe Lourenço de Oliveira et al. “Rapid motion correction in MR-guided high-intensity focused ultrasound heating using real-time ultrasound echo information”. en. In: *NMR in Biomedicine* (Nov. 2010).

[13] H. G. Flynn. “Generation of transient cavities in liquids by microsecond pulses of ultrasound”. In: *The Journal of the Acoustical Society of America* (Dec. 1982).

[14] Evan Unger et al. “Cardiovascular drug delivery with ultrasound and microbubbles”. en. In: *Advanced Drug Delivery Reviews* (June 2014).

[15] Kathryn E. Hitchcock et al. “Ultrasound-Enhanced rt-PA Thrombolysis in an ex vivo Porcine Carotid Artery Model”. en. In: *Ultrasound in Medicine & Biology* (Aug. 2011).

[16] Saurabh Datta et al. “Ultrasound-Enhanced Thrombolysis Using Definity® as a Cavitation Nucleation Agent”. en. In: *Ultrasound in Medicine & Biology* (Sept. 2008).

[17] Alison Burgess and Kullervo Hynynen. “Drug delivery across the blood–brain barrier using focused ultrasound”. en. In: *Expert Opinion on Drug Delivery* (May 2014).

[18] Fabrice Marquet et al. “Real-Time, Transcranial Monitoring of Safe Blood-Brain Barrier Opening in Non-Human Primates”. en. In: *PLoS ONE* (Feb. 2014). Ed. by Stefan Liebner.

[19] Amit Livneh et al. “Extracorporeal acute cardiac pacing by High Intensity Focused Ultrasound”. en. In: *Progress in Biophysics and Molecular Biology* (Aug. 2014).

[20] Anat Hersch and Dan Adam. “Premature cardiac contractions produced efficiently by external high-intensity focused ultrasound”. eng. In: *Ultrasound in Medicine & Biology* (July 2011).

[21] Thomas Deffieux et al. “Low-intensity focused ultrasound modulates monkey visuomotor behavior”. eng. In: *Current biology: CB* (Dec. 2013).

[22] E. Rezayat and I. Ghodrati Toostani. “Review Paper: A Review on Brain Stimulation Using Low Intensity Focused Ultrasound”. In: *Basic and Clinical Neuroscience Journal* (2016).

[23] Michel Haïssaguerre et al. “Spontaneous Initiation of Atrial Fibrillation by Ectopic Beats Originating in the Pulmonary Veins”. In: *New England Journal of Medicine* (1998).

[24] David J Wilber et al. *Catheter ablation of cardiac arrhythmias: basic concepts and clinical applications*. English. OCLC: 608624157. Malden, Mass.: Blackwell, 2008.

[25] Simon Schopka et al. “Ablation of atrial fibrillation with the Epicor system: a prospective observational trial to evaluate safety and efficacy and predictors of success”. In: *Journal of cardiothoracic surgery* (2010).

[26] Babak Nazer et al. “Epicardial Catheter Ablation Using High-Intensity Ultrasound”. In: *Circulation: Arrhythmia and Electrophysiology* (2015).

[27] Aravindan Kolandaivelu et al. “Cardiovascular magnetic resonance guided electrophysiology studies”. en. In: *Journal of Cardiovascular Magnetic Resonance* (2009).

[28] De Senneville et al. “Feasibility of fast MR-thermometry during cardiac radiofrequency ablation”. en. In: *NMR in Biomedicine* (Apr. 2012).

[29] Solenn Toupin et al. “Feasibility of real-time MR thermal dose mapping for predicting radiofrequency ablation outcome in the myocardium in vivo”. In: *Journal of Cardiovascular Magnetic Resonance* (Jan. 2017).

[30] Hubert Cochet et al. “Steam pop during radiofrequency ablation”. In: *Circulation: Arrhythmia and Electrophysiology* (2014).

[31] Jacob S. Koruth et al. “Unusual complications of percutaneous epicardial access and epicardial mapping and ablation of cardiac arrhythmias”. eng. In: *Circulation. Arrhythmia and Electrophysiology* (Dec. 2011).

[32] Kenneth A. Ellenbogen, ed. *Clinical cardiac pacing, defibrillation, and resynchronization therapy*. eng. 4. ed. OCLC: 774433798. Philadelphia, PA: Elsevier/Saunders, 2011.

[33] F. Delahaye et al. “[Epidemiology and prognosis of cardiac insufficiency]”. fre. In: *Archives Des Maladies Du Coeur Et Des Vaisseaux* (Dec. 2001).

[34] Michael D. Gammage. “Temporary cardiac pacing”. In: *Heart* (2000).

[35] Robert G. Tancredi et al. “Temporary transvenous catheter-electrode pacing of the heart”. In: *Circulation* (1967).

[36] B. Gamrath et al. “Noninvasive pacing: what you should know”. eng. In: *Journal of emergency nursing: JEN: official publication of the Emergency Department Nurses Association* (June 1998).

[37] E Rosenthal et al. “Transcutaneous pacing for cardiac emergencies.” In: *Pacing and clinical electrophysiology : PACE* (1988).

[38] S. C. Davies et al. “Ultrasound quantitation of respiratory organ motion in the upper abdomen”. In: *The British journal of radiology* (1994).

[39] Tetsuya Horiuchi et al. “Heart motion measurement with three dimensional sonomicrometry and acceleration sensing”. In: IEEE, Oct. 2012.

[40] Hao-Li Liu et al. “Focal beam distortion and treatment planning in abdominal focused ultrasound surgery”. In: *Medical Physics* (2005).

[41] Svetlana Bobkova et al. “Focusing of High-Intensity Ultrasound Through the Rib Cage Using a Therapeutic Random Phased Array”. en. In: *Ultrasound in Medicine & Biology* (June 2010).

[42] Minjuan Zheng et al. “High-Intensity Focused Ultrasound Ablation of Myocardium In Vivo and Instantaneous Biological Response”. en. In: *Echocardiography* (Oct. 2014).

[43] Shunkang Rong et al. “Septal Ablation Induced by Transthoracic High-Intensity Focused Ultrasound in Canines”. In: *Journal of the American Society of Echocardiography* (Oct. 2013).

[44] Francis Bessiere et al. “Ultrasound-Guided Transesophageal High-Intensity Focused Ultrasound Cardiac Ablation in a Beating Heart: A Pilot Feasibility Study in Pigs”. en. In: *Ultrasound in Medicine & Biology* (Aug. 2016).

[45] Simon Schopka et al. “Research article Ablation of atrial fibrillation with the Epicor system: a prospective observational trial to evaluate safety and efficacy and predictors of success”. In: (2010).

[46] Cameron Wright et al. “In Vitro and In Vivo High-Intensity Focused Ultrasound Thrombolysis:” en. In: *Investigative Radiology* (Apr. 2012).

[47] Kenichiro Hanawa et al. “Low-Intensity Pulsed Ultrasound Induces Angiogenesis and Ameliorates Left Ventricular Dysfunction in a Porcine Model of Chronic Myocardial Ischemia”. en. In: *PLoS ONE* (Aug. 2014). Ed. by Costanza Emanueli.

[48] J. I. Laughner et al. “Three Potential Mechanisms for Failure of High Intensity Focused Ultrasound Ablation in Cardiac Tissue”. en. In: *Circulation: Arrhythmia and Electrophysiology* (Apr. 2012).

[49] S. Adam Strickberger et al. “Extracardiac ablation of the canine atrioventricular junction by use of high-intensity focused ultrasound”. In: *Circulation* (1999).

[50] D. Dalecki et al. “Thresholds for premature ventricular contractions in frog hearts exposed to lithotripter fields”. eng. In: *Ultrasound in Medicine & Biology* (1991).

CHAPTER 2

Materials and methods

Contents

2.1 Materials

2.1.1 MRI system

Two preclinical MRI scanners, dedicated exclusively for research purposes, are available at IHU-LIRYC institute. Most part of this research thesis has been performed on a

1.5T Aera (Siemens, Germany) scanner. This scanner is particularly suited for interventional MRI as it is provided with a large bore magnet (70 cm), allowing more space for devices manipulation inside the magnetic field.

For research purposes, the MRI vendor provided us with a programming environment (IDEA, Siemens, Germany) to modify and compile (C++ language) MR-sequences. Source code from several commercial sequences were available through research collaboration agreement between IHU-Liryc and Siemens, such as echo-planar imaging and MR-navigator modules.

2.1.2 MR-data reconstruction

MR-data reconstruction was performed on the MR-scanner or using a home made external server on which an open source framework of reconstruction called The Gadgetron [1] was installed. The Gadgetron framework embeds a large variety of tools to reconstruct cartesian and non-cartesian data using different algorithms already published in the literature (e.g. kt-sense, cine breath-hold, GRAPPA, EPI,...). The Gadgetron works as a chain of black boxes (called Gadgets) that can be implemented in Matlab or Python for rapid prototyping or in C++ (CPU, GPU) when higher reconstruction performances are required, such as for real-time interventional MRI. Each gadget operates on the incoming data and then, sends processed data downstream to the next gadget, with standardized input/output and description header, depending on manipulated data type (k-space lines or images). Both headers use a generic template called ISMRM Raw Data (ISMRMRD) Format for standardization purposes.

2.1.3 MR-compatible HIFU system

2.1.3.1 Technological considerations

An HIFU device is composed of several piezoelectric materials (transducers). A piezoelectric material has two regimes, one in emission and another in reception (see Figure 2.1). If voltage is applied on two opposite faces of piezoelectric materials, a mechanical deformation (shortening, elongation or shear) is produced. These variations in length will generate acoustic waves that will propagate in the medium. On the other hand, if its opposite faces are mechanically deformed, a voltage is generated between the two faces of the transducer (see Figure 2.1). For therapeutic ultrasound devices, transducers are made so that they can emit high acoustic powers. Nevertheless, they can also be used in reception with a rather good sensitivity, as presented in Chapter 5 of this thesis.

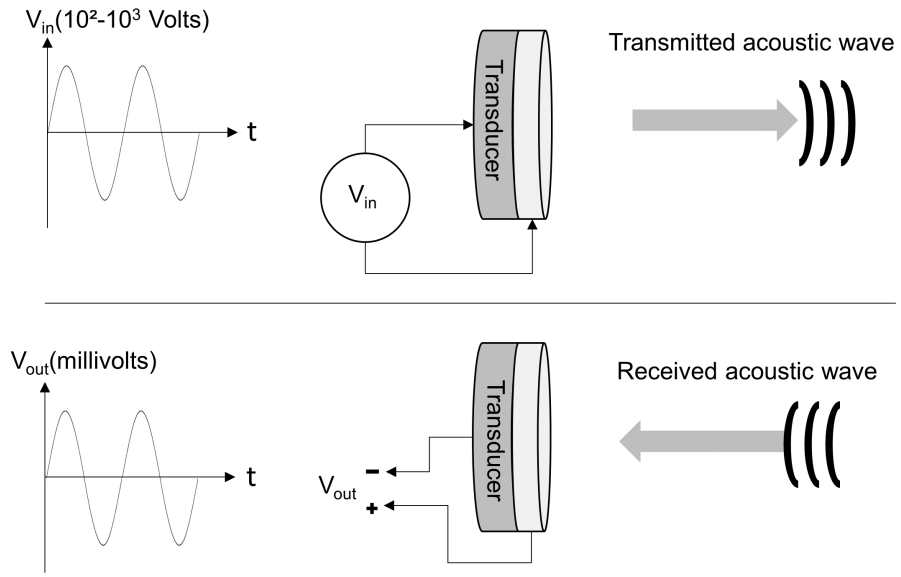

Figure 2.1: Transducer. A piezoelectric material can operate as a transmitter (top) if voltage is applied to its opposite faces, or it can operate as a receiver by transforming the pressure applied on its faces into voltage (bottom).

Therapeutic HIFU devices often embed several piezoelectric transducers distributed on a concave surface. This organization allows to focus the ultrasound beam emitted from the different transducer and deposit most part of the emitted energy at the natural focus. From the diffraction theory, the characteristics of the focus (see Figure 2.2) can be estimated as:

$$\begin{cases} l \approx \lambda \frac{F}{D} & \text{transversal dimension} \\ \\ L \approx 7\lambda (\frac{F}{D})^2 & \text{longitudinal dimension} \end{cases} \tag{2.1}$$

where λ is the wave length of ultrasounds. F and D are the focal distance and the transducer aperture, respectively. Hence the theoretical wave length and size of the focus, for F = 1 MHz and F/D = 0.9, is λ = 1.5 mm and l x L=1.4 x 8.5 mm^2, respectively.

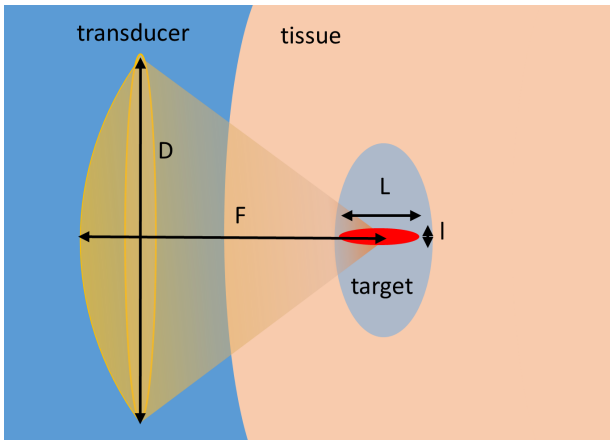

Figure 2.2: HIFU focus size. Illustration of the transducer characteristics and the resulting focus size. The focus size is represented in red and depicts where most part of the ultrasound energy is delivered.

2.1.3.2 Large animal platform

The HIFU platform used in the context of this thesis was provided by Imaged Guided Therapy company (Pessac, France). It consists of a 256 element transducer operating at 1 MHz, with a natural focus at F=13 cm from the surface of the circular transducer (D=14.5 cm in diameter). It is embedded in a mechanical positioning system allowing 2D horizontal displacement using two step-by-step piezo-electric motors (Image Guided Therapy, Pessac, France) (see Figure 2.3). The transducer was powered by a 1.1 kW electric generator (Image Guided Therapy, Pessac, France). Frequency, duration and amplitude of each electrical channel can be adjusted from the Thermoguide^{TM} software (Image Guided Therapy, Pessac, France) or using a dedicated library (Image Guided Therapy, Pessac, France) available in python, c++ or Matlab^{TM}.

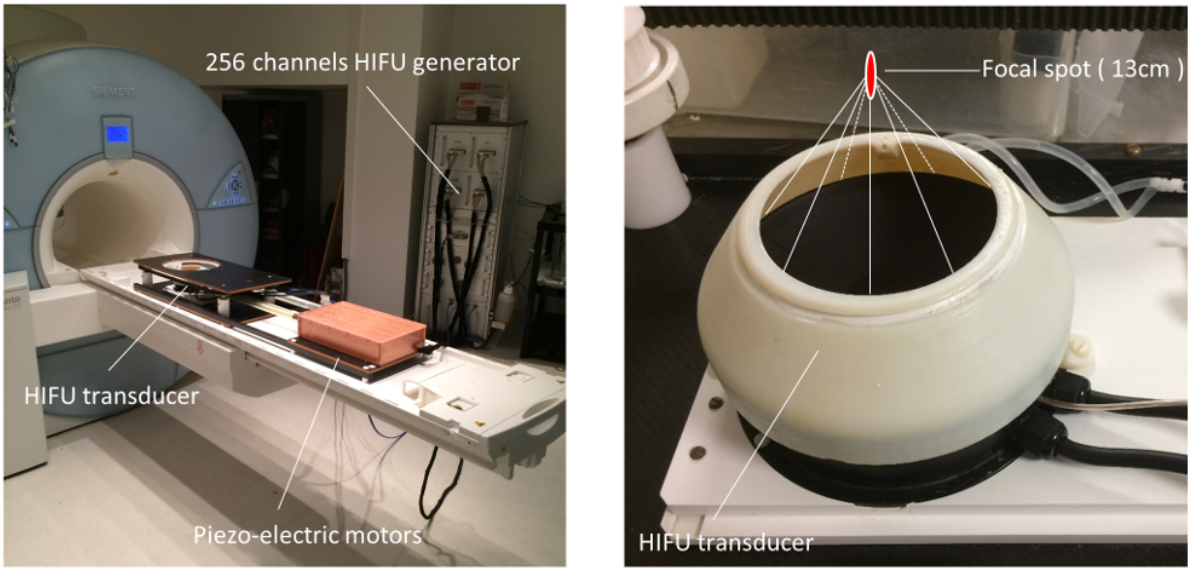

Figure 2.3: 256 elements, large animal HIFU platform.

Our transducer was calibrated using a 0.5 mm diameter needle hydrophone (Precision Acoustics, Dorchester, UK) in a deionized and degassed water tank. We have calibrated the focus size of the transducer at low acoustic power (40 W acoustic, 5 % of the maximal electrical amplitude of the generator) in order to avoid damaging the hydrophone. The focus was measured at -6 dB to be 1.8 mm wide in the focal plane and 12.6 mm wide along the focal axis. In addition, the linearity of the acoustic pressure in function of the pulse amplitude, and acoustic pressure loss during electronic steering were also investigated.

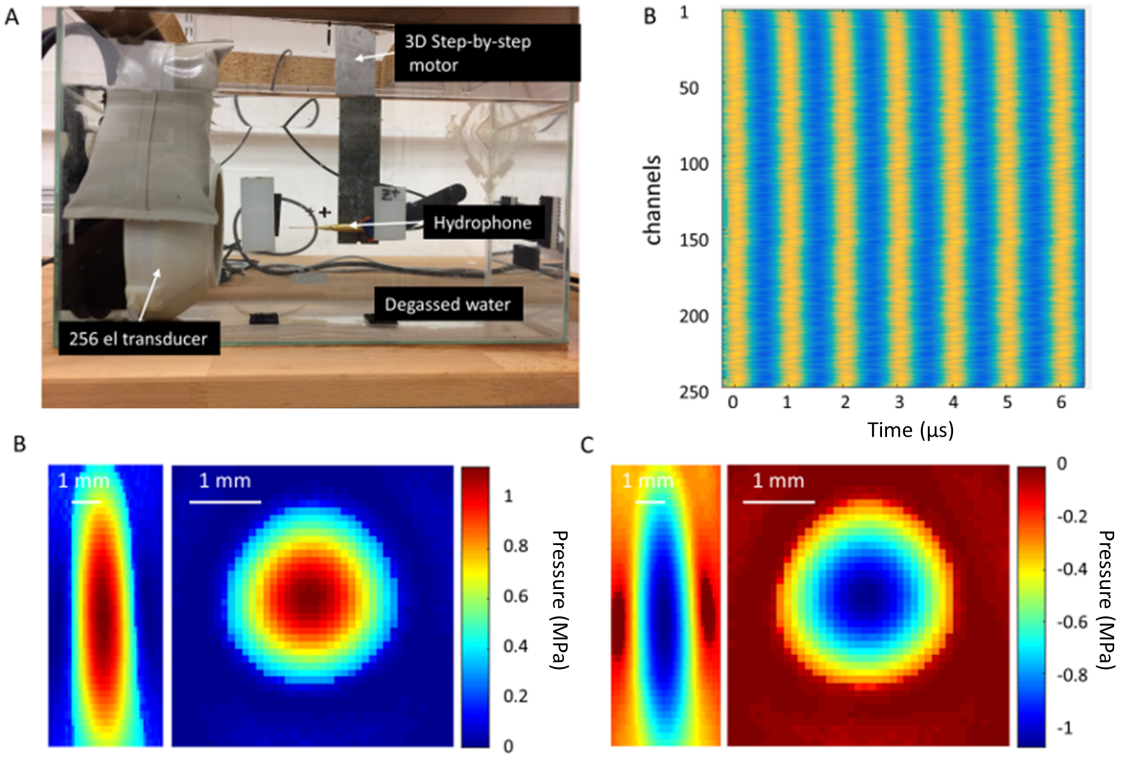

Figure 2.4: Calibration of the 256 channel transducer. A) shows the experimental setup for the calibration of the transducer. B) displays an element by element map of the signal of a 7 *mus* HIFU shot acquired at the focus . Time of flight has been cropped and blue and yellow correspond to the negative and positive pressures, respectively C) and D) represents the 2D map of the peak positive and peak negative pressures at 40 W acoustic, respectively

2.1.4 Thermoguide software

Thermoguide^{TM} software is also provided by Image Guided Therapy company (Pessac, France) and is used for image display, real-time image computation and to control HIFU sonication. It embeds two parts: 1) a monitoring interface and 2) an HIFU control tab.

1) Monitoring interface. This interface allows receiving images on the fly reconstructed by the MRI or through the Gadgetron, displays them and compute temperature maps that can be overlaid in colour onto magnitude images (see Figure 2.5). Home-made software modules can also be implemented in this interface to provide specific

image processing pipelines. In addition, Thermoguide^{TM} has several tools that are useful during the monitoring for manipulating the data such as:

- Draw region of interests and display a graphic of average, min, max or standard deviation in this region along time.
- Draw a pixel of interests and display its value along time.
- ...

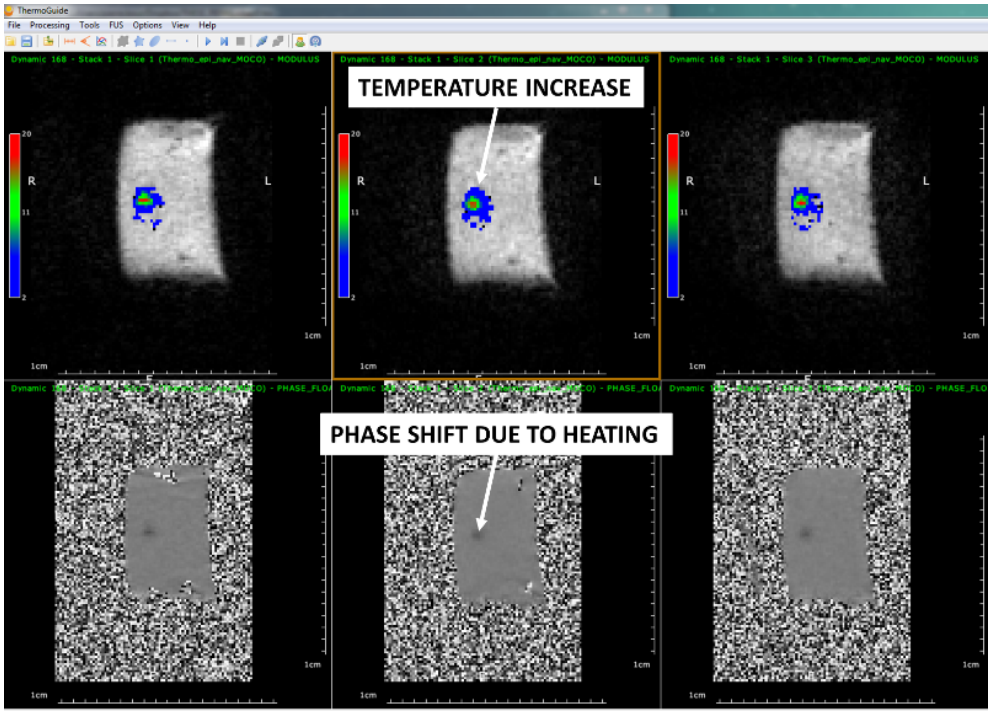

Figure 2.5: Monitoring interface. Screen capture of the monitoring interface during a temperature monitoring on a gel phantom. The top row displays the magnitude of three slices with the temperature increase in overlay. The bottom row shows the corresponding subtracted phase images for the same three slices.

2) HIFU control tab. This HIFU control tab allows connecting a remote computer to the generator in order to initialize the motors position and to prepare the planning step. Once the motors are initialized, the user can load a 3D volume to locate the transducer and localize the focus position in the image space. Then a series of HIFU pulses can be prepared using a predefined shape (e.g. square, spiral, circle, single point) with defined amplitudes, pulse durations and delays between sonications. During the thesis, complex sonication patterns were performed from Matlab^{TM} using the dedicated IGTFUS library (Image Guided Therapy, Pessac, France) .

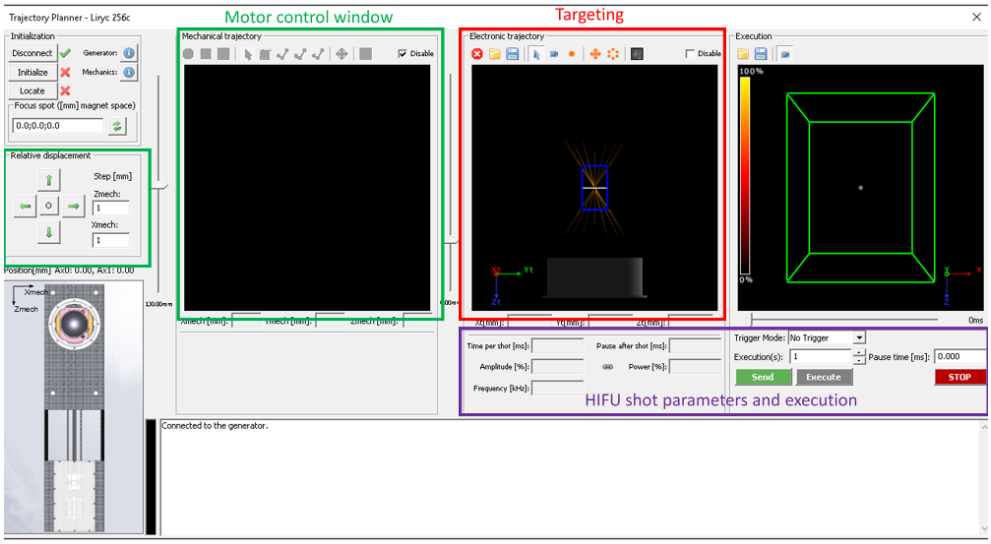

Figure 2.6: HIFU control tab. Screen capture of the HIFU control tab using our large animal platform. Green box show the motor initialization and motors trajectory planning interface, respectively. Red box represents a 3D rendering of HIFU sonication, where anatomical reference images can be overlaid, for a precise targeting. Purple box is the HIFU shot parametrization tab.

2.1.5 Acquisition board and ultrasound receiver

A single-element passive cavitation detector (PCD, model Y133_ MR, 10kHz – 20 MHz bandwidth, 5 mm active diameter, unfocused MR-compatible hydrophone, Sonic Concepts, WA, USA) (Figure 2.7A) was used to record backscattered signals from HIFU pulses interacting with tissue The PCD was connected to a digitizer (Oscar, 12-bit, 100MHz sampling frequency, Gage Applied Technologies, DynamicSignal LLC, IL, USA)(Figure 2.7B) through a 20 dB preamplifier (PA133_ MR, 100 kHz to 15 MHz operating band down to -3 dB from max amplification, Sonic Concepts, WA, USA)(Figure 2.7A)the complete chain of acquisition was MR-compatible.

Figure 2.7: Passive cavitation detection A) shows on the left the wide-band frequency hydrophone and the pre-amplifier on the right. B) The acquisition of the signal was performed using a GaGe Oscar (Oscar, 12-bit, 100 MHz sampling frequency, Gage Applied Technologies, DynamicSignal LLC, IL, USA) which can acquire up to 4 channels at 100 MHz.

2.1.6 Overview of the MRgHIFU platform at LIRYC

Figure 2.8 shows the organization of the different tools and devices that are available at IHU-LIRYC for the monitoring of MRgHIFU procedures. We have developed MR-acquisition sequences dedicated to MR-thermometry and/or MR-ARFI with the possibility to enable an navigator echo for 3D motion compensation, on every sequences. MR-rawdata were transferred on the fly by a TCP/IP connection to our reconstruction server, where the Gadgetron has been installed. On this server, all the reconstruction algorithms and data post-processing pipelines were implemented. After reconstruction images were sent black to the scanner or/and to the remote computer for image display and manipulation. The remote computer was used as a monitoring station, where images were displayed on the fly and sonication were performed. In addition, a four channels Gadge acquisition card (Oscar, 12-bit, 100 MHz sampling frequency, Gage Applied Technologies, DynamicSignal LLC, IL, USA) has been integrated to the remote computer for ultrasound signal acquisitions (used in Chapter 3 and 5), allowing multiple data manipulation in a single console.

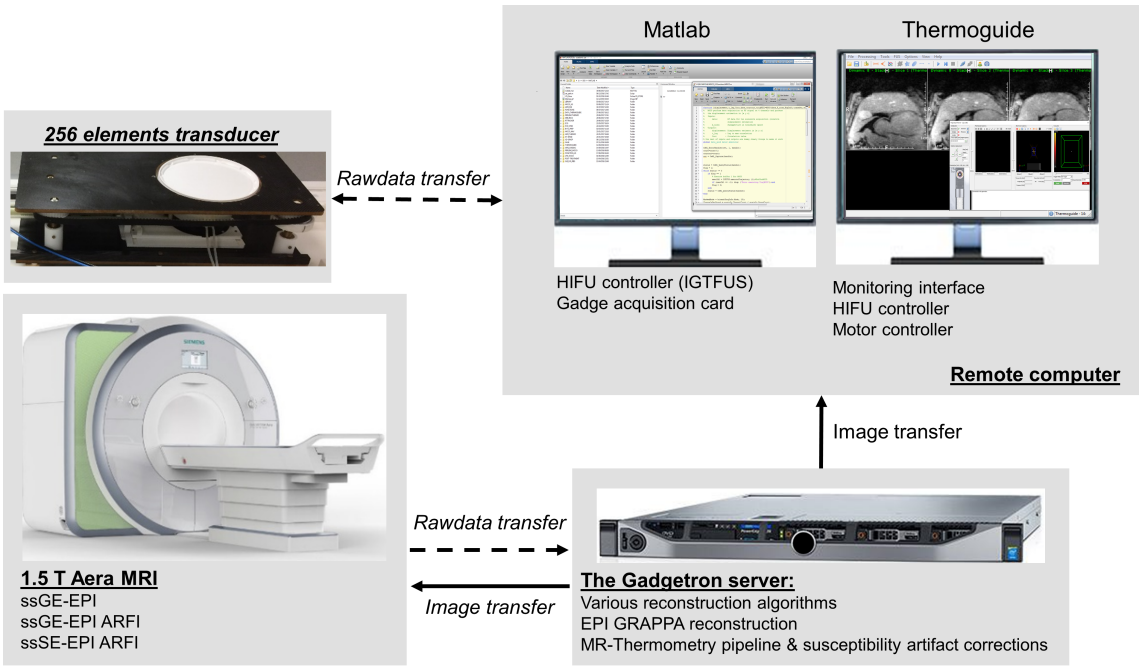

Figure 2.8: MRgHIFU platform at IHU-LIRYC

2.2 Methods

2.2.1 Basics of magnetic resonance imaging

The purpose of this chapter is not to provide physical details on MRI physics, since this topic is widely covered by abundant literature [2, 3]. Only basic principles of image formation are provided to understand the technical developments performed in this thesis.

Basically, MRI is providing a 1D (profile), 2D (image) or 3D (volume) map of the net magnetization from protons of water and fat molecules sumitted to a static magnetic field B0. To produce an image, the MR-signal is spatially encoded in the frequency domain (k-space) using magnetic gradient fields that can be applied in any physical axis with programmable timings. Since the precession frequency of the magnetization is proportional to the magnetic field, the presence of a magnetic gradient field superposed to the static B0, induces a spatially dependent frequency of the MR-signal. The sum of all contributions from each individual magnetization rotating at different frequencies depending on their position, is collected by one or several sensors called receiver coil(s) usually positioned around the patient and near the region of interest. Then, Fourier transformation is applied on the acquired signal to separate in frequency (thus in position) the individual magnetization and retrieve a spatial profile. In 2D (or 3D), two (three) gradients are applied in orthogonal directions to acquired a Fourier transform of the image (volume) called "k-space". The central parts of the k-space encode the low spatial frequencies and have the highest signal amplitude due to less gradient-dependent dephasing. These low spatial frequencies define the broad contrast observed in the resulting image whereas the outer portions of k-space encode the higher spatial frequencies (details) and have the lowest amplitude (due to greater gradient dependent dephasing). After Fourier transform of the k-space, two images can be generated from the complex k-space matrix: the magnitude and the phase image (see Figure 2.9). In this thesis, both images will be exploited.

Different trajectories can be performed to cover this k-space (through different combinations of gradient amplitudes and durations in different axes), such as a line-by-line cartesian reading, spiral, radial, arbitrary... However, this process can be time consuming and several strategies have been proposed to reduce the number of data to acquire. As an example, the use of multiple receiver coils positioned at different locations was exploited to acquire 1 line over N and thus accelerate the acquisition by a factor of N. Several reconstruction algorithms have been proposed to reconstruct images of identical spatial resolution and field-of-view as if a full k-space had been acquired using redundant information acquired simultaneously. These are known as parallel imaging techniques,

whose most used algorithms are SENSE and GRAPPA [4, 5] and rely on the spatial modulation of the signal dependent of each receiver coil sensitivity relative to the field of view.

Very recently, other strategies have been proposed to further reduce the number of data to collect and reduce acquisition time. Images of good quality are then reconstructed with iterative algorithms [6, 7]. Other methods rely on simultaneous excitation of several slices simultaneously [8]. Again, using redundancy from the same signal acquired from multiple coils and exploiting the different coil sensitivities, it is possible to reconstruct images from several slices excited simultaneously from a single acquisition. These fields are of central interest in the research community to further accelerate image acquisition while maintaining exploitable image quality.

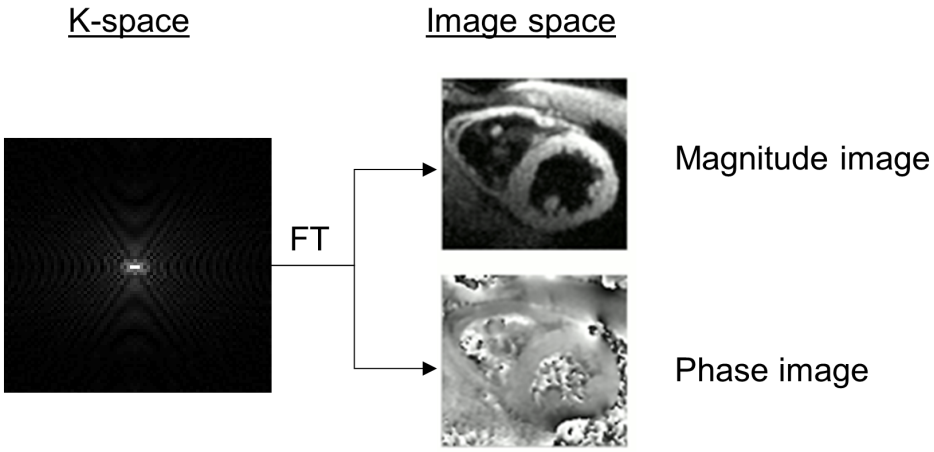

Figure 2.9: Fourier transform of k-space. By applying the Fourier transform operator (FT) to the complex k-space image, a complex image in image space can be generated. From this complex image, magnitude and phase images can be retrieved by tacking the absolute value and the argument of this complex image, respectively.

2.2.2 From MR-sequence to biomarker monitoring

An MR-sequence is a precise and temporal organization of radiofrequency excitations and magnetic gradients that are played to fill the k-space. As introduced in the precedent section, phase and magnitude images are derived from k-space, after Fourier transform. These images are sensitive to different characteristics of the object (proton density, tissue properties, temperature, displacement, ...). During MRgHIFU procedures, these biomarkers will vary and their monitoring is of particular interest to define a therapy end-point and/or assess the safety of the procedure. To this end, we have developed at IHU-LIRYC an entire pipeline from the MR-acquisition to the monitoring display, through the reconstruction of MR-rawdata. We have focused our interest on two biomarkers, firstly the

temperature and secondly the displacement, since both of them can be modulated by appropriate use of HIFU sonications.

2.2.2.1 Echo planar imaging

Several sequences are available in MRI and methods are constantly improved by the research community to increase the spatial resolution and reduce acquisition times. In this thesis, in perspective of a cardiac applications, our choice was to use a fast sequence in order to limit motion artifacts during acquisitions (this part is discussed in more details later in this chapter). Single shot Gradient Echo Echo-Planar Imaging sequences (ssGE-EPI) is one of the fastest MR-acquisition available. This sequence was first introduced in 1991 by Stehling et al. [9] and since then, it has been exploited for numerous applications [10]. As compared to conventional MR-acquisitions, which acquire one line only after each radiofrequency excitation, ssGE-EPI acquires all the k-space lines after a single radiofrequency excitation (see Figure 2.10A and C). Note that other EPI sequences called segmented-EPI acquire several lines at each excitation. Despite a gain in signal to noise ratio [11], segmented-EPI sequences have a lower temporal resolution and are incompatible with cardiac applications.

Advantages:

- Widely-used sequence for numerous applications (fMRI for example). . Its characteristics are well-established.
- High temporal resolution ($<$ 100 ms for a single-shot acquisition). Hence, risks of intra-scan motion artifacts for cardiac imaging.
- Compatible with parallel imaging and/or simultaneous multislice acquisitions.

Disadvantages:

- Susceptible to B0 field inhomogeneities and off-resonance effects.
- Geometric distortions effects.
- Blurring effects.

A variant of this sequence is the single shot Spin-Echo Echo-Planar Imaging sequence (ssSE-EPI). A 180 ° refocusing pulse is added at the half of the echo time (TE) in order to compensate for B0 inhomogeneities (see Figure 2.10B and D). Its temporal resolution is slightly lower as compared to the ssGE-EPI due to the refocusing pulse. However, it produces images less sensitive to field inhomogeneities. In the context of this thesis, the

spin-echo sequence is of interest for displacement monitoring sequences as it improves displacement profiles and robustness to bulk motion and background phase distortions [12]. Note that due to the refocussing pulse, it is not possible to perform MR-thermometry with this type of sequence. **To synthesise,during this thesis, when temperature mapping was performed we used ssGE-EPI sequences and when displacement alone was monitored, we used ssSE-EPI sequences.**

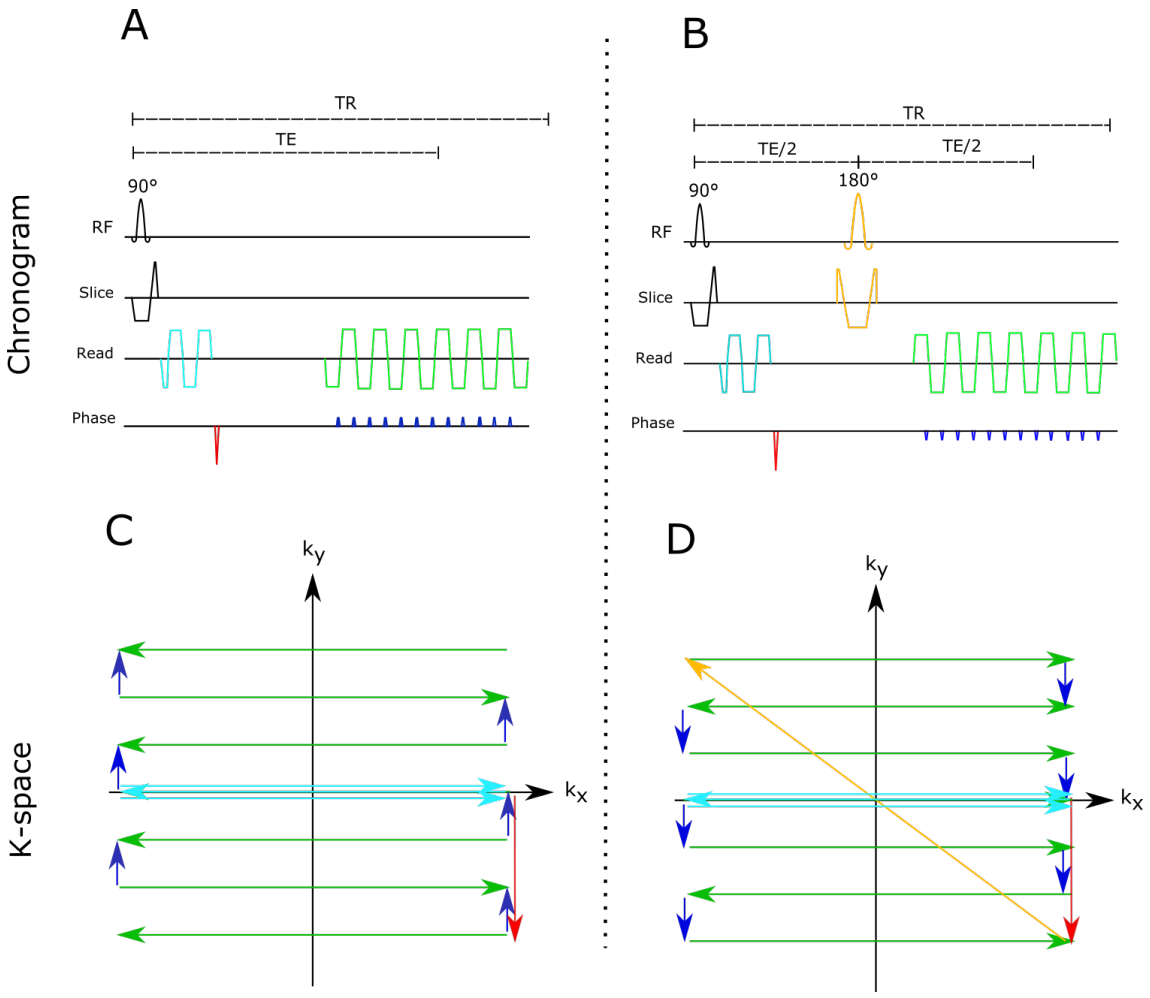

Figure 2.10: Echo planar imaging sequence. A and B show chronogram of an gradient echo and a spin-echo EPI sequence, respectively. C and D show a representation of the path in the k-space for both gradient and spin-echo EPI sequences, respectively. After the slice selection, tree lines are acquired at the center of the k-space (light blue). These lines are used to correct an offset in phase between positive and negative readouts. Then a phase shift is applied to travel to the border of the k-space (red). The readout of EPI is performed using an echo train (green) with a blip gradient in the phase encoding direction (blue) between two echoes, in order to run thought of the ky dimension. For spin-echo EPI a refocussing pulse (yellow) is inserted between the phase shift (red) and the readout. As the refocussing pulse reverses the magnetization (yellow arrow in C), the readout and gradient blips are inverted in polarization.

2.2.2.2 Generalized auto-calibrating partially parallel acquisitions

In order to reduce the acquisition time of an image, all EPI sequences presented in this thesis were acquired with a parallel imaging technique called Generalized Autocalibrating

Partially Parallel Acquisitions (GRAPPA) [4]. GRAPPA is a multi-coil parallel imaging techniques. Like other parallel methods, GRAPPA undersamples the acquisition in the phase-encoding direction. This phase undersampling reduces imaging time by a factor called the acceleration factor (usually 2). The counterpart of phase undersampling is aliasing in the image domain that must be untangled (see Figure 2.11).

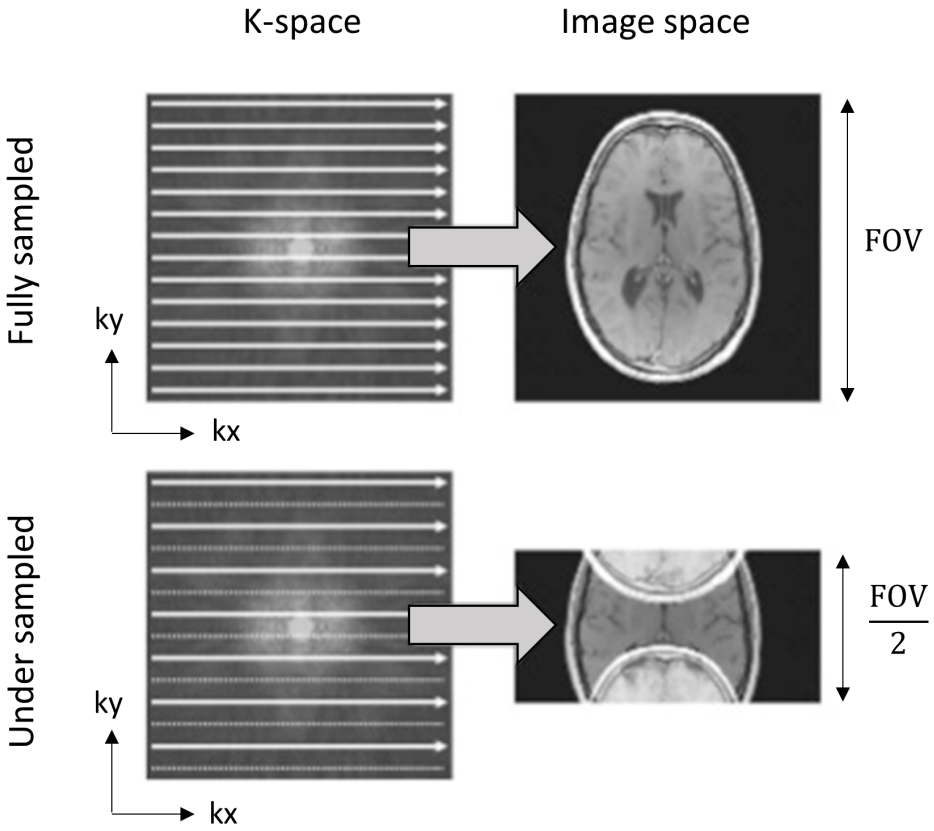

Figure 2.11: Image aliasing. Top row shows an acquisition of a fully sampled k-space, resulting in a full FOV image after Fourier transformation. The bottom row shows the same object undersampled (dashed lines represent non acquired data) in the phase encoding direction (acceleration factor = 2), resulting in aliased image.

In order to unfold the image, an autocalibration scan is performed at the beginning of the time series with several lines acquired around the center of the k-space (see ACS in Figure 2.12. The number of ACS lines used is usually 24. Measurements from the autocalibration acquisitions are used to calculate a kernel, for each coil. This kernel is filled with weighting factors (see w in Figure 2.12 extracted from [13]).) which reflect how each coil distorts, smears, and displaces spatial frequencies within the full FOV. Then, to reconstruct undersampled acquisitions, missing k-space points are estimated in an iterative fashion using a convolution between the kernel and acquired k-space.

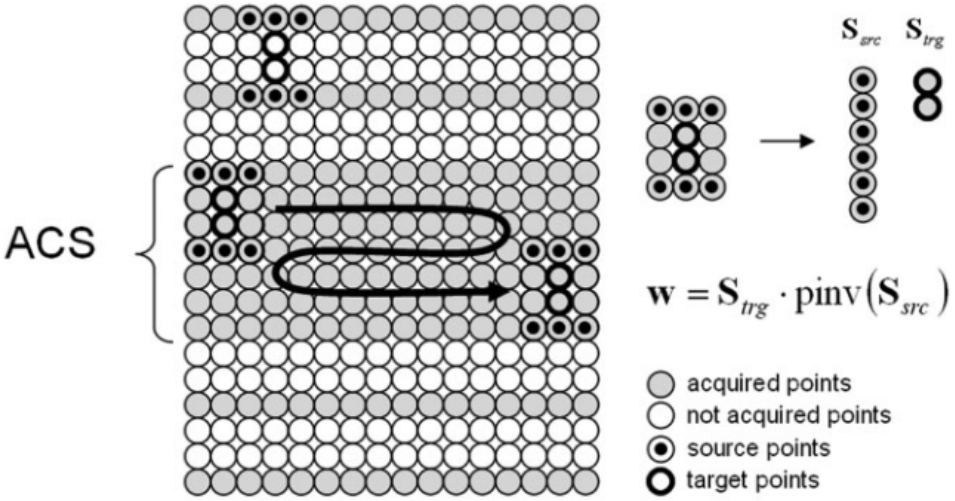

Figure 2.12: Schematic description of GRAPPA weights determination: According to the undersampling scheme (here R = 3), a GRAPPA reconstruction kernel is defined (here 2x3) in which source and target points are identified (coil dimension omitted). The kernel is slid through the ACS data and all the kernel repetitions are collected in a source matrix S_{src} and target matrix S_{trg}. The GRAPPA reconstruction weights (w) are then derived by solving w=S_{trg}.pinv(S_{src}) .

The GRAPPA reconstruction algorithm, results in a loss of signal to noise ratio, which is proportional to $\frac{1}{\sqrt{A}}$, where A is the acceleration factor. However, this loss is partially balanced with shorter TE and thus lower T2* weighting.

2.2.2.3 Reconstruction using the Gadgetron

GRAPPA EPI rawdata were reconstructed using the Gadgetron with the pipeline called *generic_EPI_grappa.xml* (see Figure 2.13).

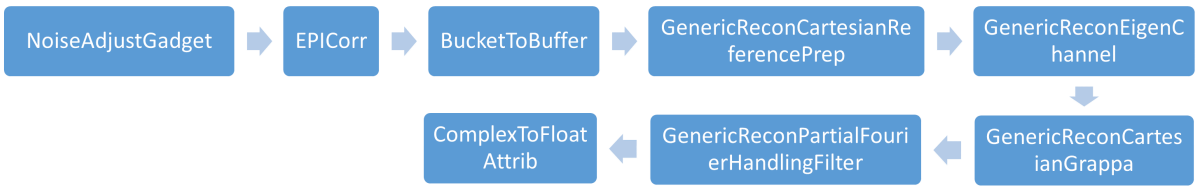

Figure 2.13: Pipeline of reconstruction. Schematic representation of the *generic_EPI_grappa.xml* pipeline. Each blue box represent a single gadget.

Noise Adjustment: Normalize each individual coil based on the amount of coherence in the signal. For coils located close to the region to image, the coherence of the signal will be higher than a coil located far from the object. Doing so, we preserve coils with low signal to noise ratio (located far form the region to image or potentially broken coils), to propagate noise into the following gadgets and degrade final image quality.

EPI cor: Performs the B0 phase correction and odd-even readout phase correction.

These corrections are based on the three lines acquired at the center of the k-space (see Figure 2.11). B0 phase correction handles the phase difference between consecutive odd or even navigators whereas odd-even readout phase correction handles the phase difference between odd and even navigators. Overall, this gadget deals with ghosting artifact observed in the phase encoding direction. The acquired data are used to provide correction of distortions in the resulting image.

GenericReconEigenChannel: Compute eigenvector on acquired data for every dynamic acquisition [14]. 1) Transform the receiver coils into virtual coils (using principal component analysis), ordered by their information content. 2) Reduce the number of coils to improve downstream performance and resulting image quality.

GenericReconCartesianGrappa: Exports prepared calibration lines (GenericReconCartesianReferencePrep) and process data for GRAPPA reconstruction. In addition, coil map sensitivity for multicoil reconstruction is performed using a coil map estimation proposed by Souheil J Inati et al. [15, 16].

GenericReconPartialFourierHandlingFilter: Handles partial Fourier acquisitions using a projection onto convex set method.

ComplexToFloatAttrib: Allows to retrieve from complex images, the magnitude and the phase image.

The Gadgetron allows a full flexibility on the reconstruction as it is fully opensource. It is hence convenient to implement and modify the pipeline of reconstruction for research purposes. In addition, the Gadgetron is updated with recent reconstruction algorithms, available in the literature that often bridge current lacks in the reconstructions provided by the MRI vendor. As an example, Figure 2.14 shows the reconstruction (phase and magnitude) of the same ssGE-EPI rawdata acquired on an ex vivo muscle sample, using either a reconstruction available on MR-system or the Gadgetron (Figure 2.14). Two main differences can be noted between both reconstructions: 1) on magnitude and 2) on phase images. 1) Differences in image pixilation is particularly visible on the magnitude image. These differences result mainly from differences in k-space filtering and on the implementation of GRAPPA reconstruction algorithm. 2) On the phase image, differences are more obvious. As compared to the Gadgetron, the phase image reconstructed by the MRI vendor shows numerous spatial wraps and phase singularities (see phase images on

Figure 2.14). The difference between both reconstruction pipelines steps mainly in the estimation of coil sensitivity maps. Indeed, the Gadgetron uses methods proposed in Souheil J Inati et al. [15, 16] that allow to generate a flat phase image without the need of spatial phase unwrapping, which is particularly convenient when the information is encoded in the phase image (such as temperature for example).

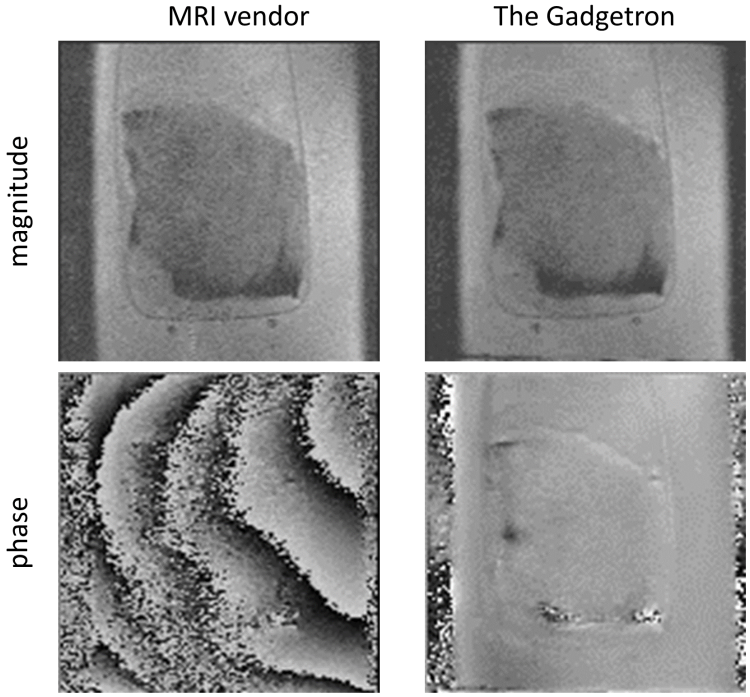

Figure 2.14: MRI vendor versus the Gadgetron. Image reconstruction of the same ssGE-EPI raw dataset using either our MRI vendor or the Gadgetron reconstruction pipeline. Image of magnitude and phase are shown for both pipelines.

2.2.3 MR-temperature

As introduced earlier, the temperature is a key biomarker to monitor during MRgHIFU procedures. Temperature variations in a medium can be monitored by MRI in a non-invasive way. The change in temperature affects several MR-parameters such as the T1, T2 and T2* relaxation times, the diffusion coefficient and the water proton resonance frequency. For non-faty tissues, the latter method is by far the most widely used method and is called the proton resonance frequency shift(PRFS) method [17]. This method relies on the linear relationship between the proton resonance frequency and the temperature. The phase variation $\Delta\varphi$ between current phase φ_{TEMP} and a reference φ_{REF} is proportional to the temperature variation ΔT between these two time points:

$$\Delta T = \frac{\Delta\varphi}{\gamma.\alpha.B_0.TE} = \frac{\varphi_{TEMP} - \varphi_{REF}}{\gamma.\alpha.B_0.TE} \tag{2.2}$$

where γ = 267.5 rad.s^{-1}.T^{-1} is the gyromagnetic ratio , α = -0.0094 ppm.°C^{-1} is the PRFS temperature coefficient, B_0 is the magnetic field strength and TE is the echo time of the MR-sequence.

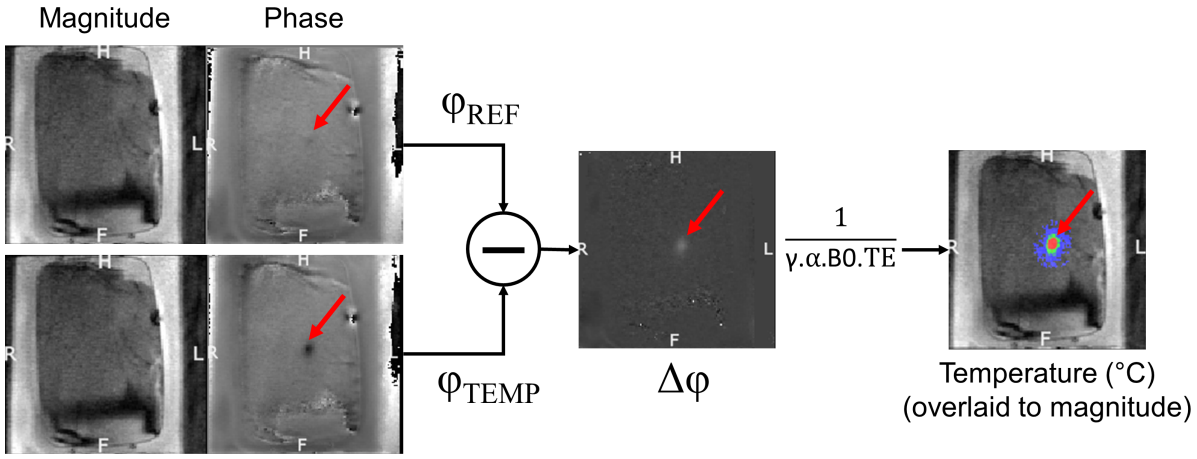

Figure 2.15: MR-Thermometry.

The PRFS has become the gold-standard temperature monitoring method for numerous applications [18, 19, 20]. Nevertheless, the main drawback of this method is the bias induced by the presence of fat, which corrupts the aforementioned linear relationship [21]. Fortunately, fat suppression or spectral selective excitation can be used to image only water protons, thereby enabling accurate PRFS thermometry in tissue where both fat and water protons are present. In fatty tissues, for instance breasts, temperature can be monitored using other temperature dependent parameters like T1, T2 or T2* [22].

2.2.3.1 Thermal dose

During thermal treatments, the determination of the therapy end-point is crucial. In the literature, one of the widely used surrogate for cell death, is the calculation of the thermal dose. Since works performed by Sapareto et al.[23], the death of cells have been related to the temperature increase and the duration of exposure. The thermal dose commonly used is defined as:

$$TD = \begin{cases} \int_0^t 4^{T(t)-43} & if \quad T(t) < 43°C \\ \int_0^t 2^{T(t)-43} & if \quad T(t) \geq 43°C \end{cases} \tag{2.3}$$

Where T(t) = $T_{REF} + \Delta T$ is the absolute temperature at the time t, T_{REF} is the reference temperature and ΔT is the temperature change measured by MR-thermometry. Since 1994, the lethal threshold for cell necrosis has been shown to be tissue dependent [24]. In a more recent publication [25], the cumulative equivalent exposure time expressed in

minutes at 43 °C has confirmed this tissue dependency.

The relevance of the thermal dose is highly dependent on the temperature to noise ratio as the exponential form easily overestimates the actual thermal dose. A correction to incorporate the temperature noise into the computation of the thermal dose has been proposed in [26].

2.2.4 MR-ARFI

2.2.4.1 Radiation force

One other biomarker of interest to monitor during MRgHIFU procedures is the displacement induced by the radiation force. Radiation pressure accompanies any wave that propagates in soft tissue. This force is proportional to the acoustic intensity I divided by the speed of the sound wave c,

$$F = \frac{2.\alpha.I}{c} \tag{2.4}$$

where α is the absorption coefficient of a given tissue.

At the focus, this force will result in a tissue displacement (Figure 2.16A) in the direction of the beam path in the order of tens of micrometers. During MRgHIFU procedures, this displacement can be used in different manners:

- As the displacement occurs only at the focus, monitoring this displacement can give information about the spatial localization of the focus. This is of particular interest during the planning step, to precisely position the focus on the targeted tissue [27, 28].
- If we consider that the force applied is constant, then any variation in the resulting displacement depends on a tissue stiffness change. A parallel can be drawn when clinician exercises a constant pressure (the force) to fill an abnormal tissue stiffness (the displacement) in the patient. Hence, monitoring the displacement can give insight of the focal tissue stiffness [29, 30].
- The longitudinal displacement induced at the focus generates strain waves in the transvers plan of the focus (see Figure 2.16B). These waves then propagate radially from the focus with a celerity characterized by the tissue stifness [31, 32].Ultrasound-based shear wave imaging relies on this principle.

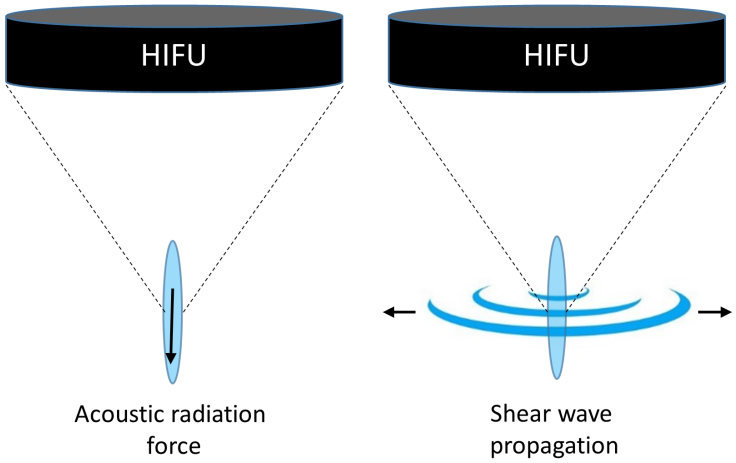

Figure 2.16: Displacement and shear wave generation. During an HIFU pulse, the radiation pressure induces a displacement at the focus A). In addition shear waves are generated B) in the transverse plan.

2.2.4.2 Monitoring the focal displacement with MRI

In MRI, the displacement induced at the focus is encoded in the phase of an MR-acquisition using bipolar Motion Encoding Gradients (MEG). The local displacement induces a phase shift φ of the MR-signal at the position $\vec{r}$ as follows:

$$\varphi(\vec{r}) = \gamma \int_0^T \vec{G(t)} * \vec{u}(\vec{r}, t)dt \tag{2.5}$$

with G the gradient strength , T the gradient duration ,$\vec{u}$ the displacement and γ the gyromagnetic ratio.

The relationship of motion relative to the duration of the ultrasound pulse and the spatial distribution of the radiation force was investigated in details by several authors [33, 34]. For an over-damped response, the transient displacement u(t) at the focus, for a shot duration T_{HIFU} synchronized at t=0, can be written as follow:

$$u(t, r=0) = \begin{cases} 0, & t < 0 \\ A.(1 - e^{-t/\tau_{rise}}), & 0 \leqslant t \leqslant T_{HIFU} \\ u(T_{HIFU}, r=0).(e^{-t/\tau_{decay}}), & T_{HIFU} \leqslant t \end{cases} \tag{2.6}$$

where A is the maximum displacement amplitude and τ_{rise} and τ_{decay} are the visco-elastic properties of the tissue [33]. In the transverse plan the generated shear waves propagate with a delay $\delta t(r) = \frac{r}{c}$ where c is the celerity of the wave.

MR-ARFI displacement maps results from the spatial convolution of the displacement

profiles and the MEG. Hence, displacement amplitudes and spatial profiles depend on the synchronization time regarded to MEG, on tissue visco-elastic properties (see τ_{rise} and τ_{decay} in eq. 2.6) and on the shear wave velocity. Other parameters such as the HIFU focus size are also involved.

From equation 2.5, MR-ARFI displacement map (D) is computed as:

$$D = \frac{\Delta\varphi}{\gamma.T.G} = \frac{\varphi_{FUS} - \varphi_{REF}}{\gamma.B0.T.G} \tag{2.7}$$

where G the absolute amplitude of the MEG. φ_{FUS} represents a phase image where an HIFU sonication is synchronized with MEG and φ_{REF} is a reference image without sonication. The phase subtraction is aimed to remove the background phase that does not account for tissue displacement encoding.

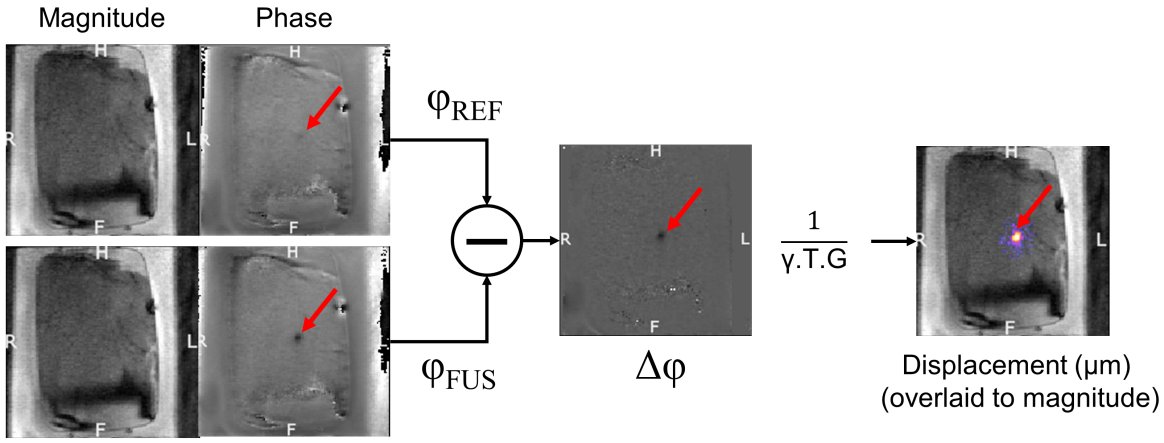

Figure 2.17: MR-ARFI.

In the literature several sequences have been proposed to monitor the ARFI displacement. They are mainly divided in two categories: spin-echo and gradient-echo sequences. Note that the optimal bipolar gradient shape and polarity have been inverstigated by Chen et al. [12].

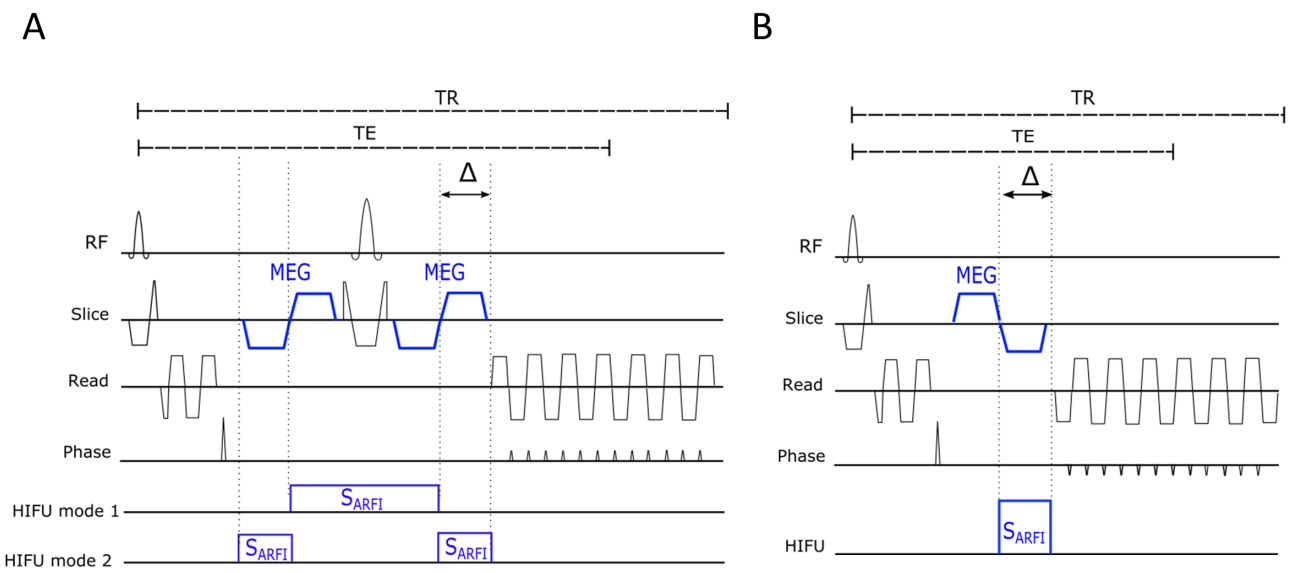

Figure 2.18: Examples of rapide ARFI sequences. Two implementations of MR-ARFI sequences using a spin-echo A) or a gradient echo B) EPI sequence. MEG are represented in blue on the slice gradient axis. HIFU sonications are synchronized on each side of the refocusing pulse for the spin-echo implementation A) and on the second lobe for the gradient echo sequence B).

2.2.5 Motion correction in MRI

2.2.5.1 Introduction

Physiological motion during MR-interventional procedures is a source of artifact in the magnitude and phase image that has to be corrected to monitor effectively the temperature and/or the displacement information. Motion artifacts in MRI are commonly coarsely divided into two categories, intrascan and interscan motion artifacts, based on the timescale of the motion as compared to the imaging.

Intrascan motion occurs when motion is observed during acquisition of the k-space. It results in blurred images if the motion time scale is in the order of the acquisition time. However, a simple way to limit these blurring effects is to use fast MR-acquisitions such as the ssGE-EPI sequences. Indeed, its temporal resolution ($\sim$ 100 ms) is short enough as compared to time scales of respiratory (5 sec or more) and cardiac motions (approximately 1 sec at rest).

Interscan motion is the motion between successive images acquired in a time series. For instance, this respiratory motion induces a translation of the heart in the head-feet direction for a coronal acquisition. This artifact can be reduced using gating strategies [35], motion corrections on image [36], or using a navigator echo [37]. Echo navigator provides a method to track motion by measuring the change in position

of an interface between tissues with high contrasts (e.g. liver and lung). Slice positions can then be corrected accordingly and online to track the respiratory motion. Note that navigator can avoid in-plane or through-plane motions, depending on the orientation of the navigator echo as compared to the slice orientation.

Despite the aforementioned tricks to limit intra and inter scan motions, the latter do not correct for the magnetic susceptibility artifact that corrupt the information of temperature/displacement encoded in the phase image. Without corrections, the phase experiences strong variations due to the inhomogeneity of the static magnetic field along the path of the displacement. Hence, phase of each pixel varies along time, with the same period as the motion. In the literature, several methods have been proposed to correct for this artifact:

Multi-baseline correction [38]. In the multi-baseline method, a set of baseline images covering the respiratory and/or cardiac cycle, are acquired before the treatment. The phase difference is then calculated between the current image acquired during heating and the baseline image with the best matching. Baseline image matching can be performed using navigator echoes or navigator echoes or by maximal intercorrelation coefficients between the current magnitude image and each magnitude images found stored in the lookup table [39].

Referenceless thermometry [40]. The referenceless method estimates background phase from the current image itself and, therefore, does not require baseline images to be acquired prior to heating. The assumption is that the background phase surrounding the heated region changes smoothly so that the phase at the hotspot can be modelled and subtracted using a low-order polynomial fitting.

Optical flow and Principal Component Analysis [41, 42]. This approach uses an optical flow analysis to learn motion patterns based on images acquired during a preoperative learning step performed before using HIFU. Subsequently, Principal Component Analysis is used to find the eigenvectors of the observed set of flow fields. Then, during hyperthermia, individual flow fields are represented as a linear combination of the basis flows, where the coefficients of the linear combination are estimated using a least square fit. Finally a synthetic phase is generated and subtracted to the current phase image. The first image is set as the reference and the following are subtracted to the reference in order to compute the temperature distribution as described in equation 2.2.

2.2.5.2 Strategies for motion compensation in interventional MRI

MR-Temperature imaging in the heart during radio-frequency ablation is one of the research fields developed by the imaging team at IHU-LIRYC. Several strategies have been investigated and validated to correct for motion and magnetic susceptibility artifact on the phase image. These developments can directly benefit MRgHIFU for interventions on mobile organs (heart, liver, kidney), one example is presented in Chapter 5. During my thesis, I have taken part of the development of these developments mainly in MR-sequence programming. I have developed several EPI sequences, designed for MR-thermometry and/or MR-ARFI, which integrated the possibility to activate an echo navigator to correct the slice position according to the motion of the liver/lung interface. These sequences embedded a crossed pair navigator which consisted to acquire a column by the intersection of consecutive slice-selective planar excitations with intersecting 90° and 180° excitations (see Figure 2.19).

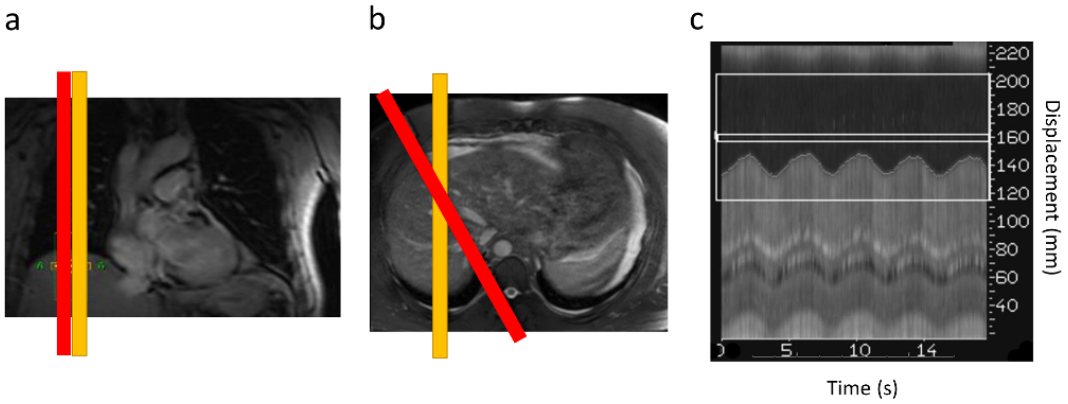

Figure 2.19: Crossed-pair echo navigator a) shows an axial view where the red and orange box represent the 90 ° and 180 ° slice selection, respectively. b) represents red and orange slice excitations in transverse orientation. c) shows successive navigator signal during free breathing condition. The liver lung interface is depicted by the arrow.

During my thesis work, two different approaches were validated for cardiac radio-frequency ablations. The first approach was validated by Ozenne et al.[43] and the second was validated by Toupin et al. [44]. Both strategies employed the optical flow and principal component analysis method, introduced in the precedent section. Physiological motions were compensated using diastolic cardiac gating and non-rigid optical flow algorithms to correct respiratory motion. Then, a PCA-based susceptibility artifact correction was performed to extract temperature information, as shown in Figure 2.20.

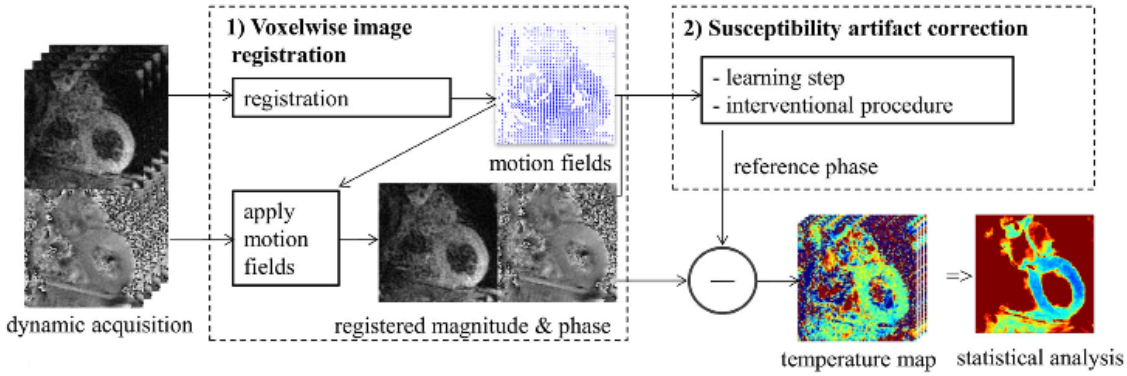

Figure 2.20: Susceptibility artifact corrections. Intrascan motions are compensated for using a nonrigid registration algorithm: Estimation of displacements on a pixel-by-pixel basis results from the analysis of intensity conservation between incoming magnitude image and a reference image. Motion fields are then applied to phase images to follow specific voxel temperature elevation. To address respiratory-induced susceptibility changes, the LUT method or synthetic modeling phase PCA is initialized during a pretreatment period. These reference data are then subtracted from the incoming registered phase during the interventional procedure.

Slice orientation: The first validation of the thermometry pipeline was performed by Ozenne et al. (see Figure 2.21 extracted from [43]), who proposed to use a coronal strict acquisition to limit through-plane motion. Despite good temperature stabilities reported in this study, this method lacked of flexibility in slice positioning (limited to coronal and sagittal strict acquisitions), which might not allow to monitor temperature in every regions of the heart.

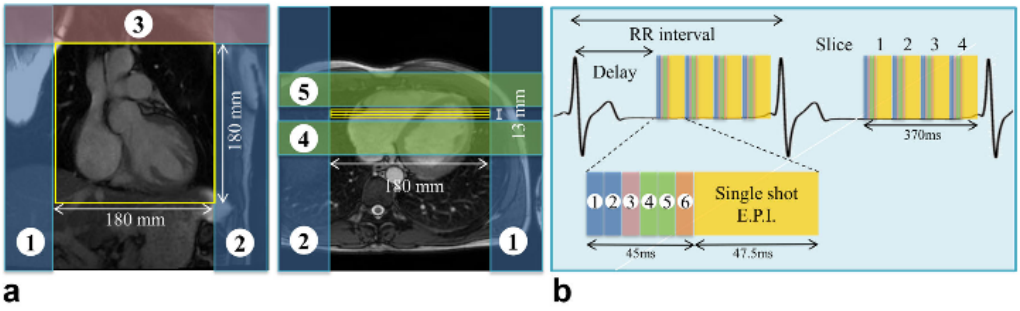

Figure 2.21: MR-Thermometry in a specific slice orientation. (a) bSSFP images in coronal and transversal orientation on a volunteer showing slice and sat band positioning for cardiac thermometry in coronal orientation. Two saturation slabs are positioned along the FOV (labeled 1 and 2) in the phase-encoding direction. Additional saturation bands (3, 4, and 5) are set parallel and perpendicular to the imaging slice to reduce the signal from blood. The gap between the sat slabs 4 and 5 and slice stack is 5 mm. (b) Timing of MR-thermometry acquisition relative to the RR interval. Labels 1, 2, 3, 4, and 5 on the insert are the saturation slabs and label 6 represents the fat saturation.

Echo navigator: A more elaborated method exploited an echo navigator to compensate for respiratory motion. This method was first porposed by Senneville et al. [45] and more recently in Toupin et al. (see Figure 2.22 extracted from [44]). Compared

to Ozenne et al., the slice orientation and position were not constrained anymore. During the procedure the slice positions were updated according to the echo navigator readings, positioned at the liver/lung interface. A slice shift factor of 0.6 was then set between liver and heart motions. Residual in plane-motions were corrected by an optical flow algorithm and the pipeline of susceptibility artifact corrections described in Ozenne et al., allowed to retrieve the temperature information.

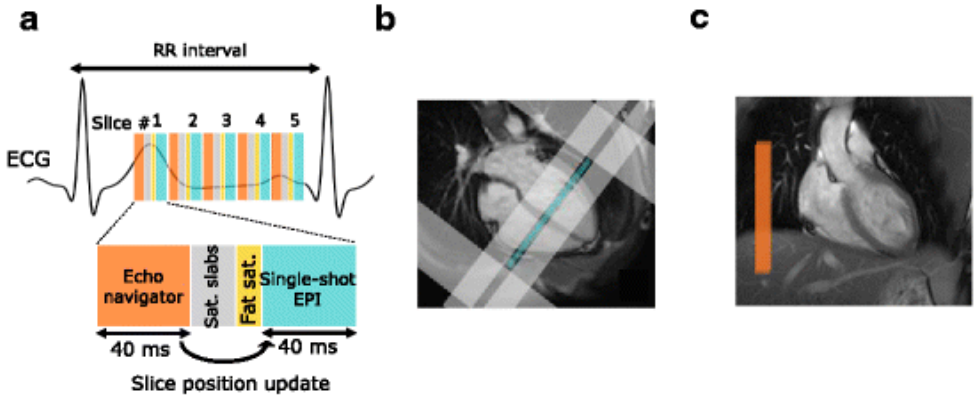

Figure 2.22: MR-Thermometry using an echo navigator (a) Up to 5 slices were acquired depending on heart cycle duration. On healthy volunteers, imaging slices were positioned in short axis orientation (4 chambers view b, blue rectangle) and surrounded by saturation slabs (image b, gray rectangles): 2 along the FOV in the phase encoding direction to limit aliasing effect and 2 parallels to the imaging slices to reduce the signal of blood. A crossed-pair navigator was positioned on the dome of the liver (image c, orange rectangle on coronal view) to monitor respiratory motion at the lung/liver interface. The echo-navigator pulse sequence was run before each slice and the detected breathing stage was used to update the position of the following slice

2.2.6 Cavitation detection

2.2.6.1 Theory

As introduced earlier, cavitation is a phenomenon intrinsic to sonication in tissues and this section will introduce it in more details. Cavitation describes dissolved gaz bubble oscillation in tissues when a negative pressure of sufficient amplitude is applied. Two regimes can coexist depending on the acoustic pressure, namely the stable and the inertial cavitation (see Figure 2.23).

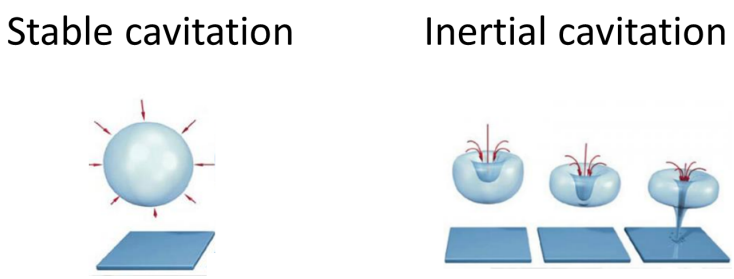

Figure 2.23: Cavitation. On the left, is represented a schematic of the inertial cavitation which describes the oscillation of the diameter of the bubble in the presence of ultrasound. When the pic negative pressure of ultrasound reaches a certain threshold, the oscillation is increased and can induce a collapse of the bubble (on the right), this process is called inertial cavitation

Stable cavitation is characterized by sustained small amplitude oscillations of the bubble about its equilibrium. The bubble's oscillations radiate pressure to the surrounding fluid, which generates flow around the bubble termed microstreaming. Microstreaming has the potential to promote beneficial bioeffects such as drug delivery [46], thrombolysis [47], disruption of the blood brain barrier [48] and cardiac stimulation [49], without irreversibly injuring the underlying tissue.

Inertial cavitation describes the collapse of bubbles. At the collapse climax, the generated peak pressure and temperature may reach extremely high values. Pressures exceeding several hundred atmospheres and temperatures on the order of several thousand Kelvin degrees have been reported. Furthermore, high speed jets may reach values close to 1000 $m.s^{-1}$. The strong mechanical stresses applied on the cell membranes and the associated high temperature may easily destroy it.

Hence, monitoring of these ultrasound-related bio-effects during the procedure seems to be compulsory depending on the desired therapeutic objective (inducing damage or creating transient reversible effects). The risk of cavitation bubbles generation during the ultrasonic radiation depends on the magnitude of the negative pressure (PNP) associated with the propagating wave and the wave's frequency (f). A mathematical relation named the mechanical index (MI) was suggested. It is defined by:

$$MI = \frac{PNP}{\sqrt{f}} \tag{2.8}$$

Based on this formalism, cavitation can be enhance in two ways: first by increasing the negative pressure (PNP) or by decreasing the ultrasound wave frequency (f). Note that currently the Food and Drug Administration, stipulates that diagnostic ultrasound cannot exceed a MI of 1.9. However, for some therapeutic ultrasound applications, this

threshold might be exceeded.

In any case, for the safety of the procedure harmful effects of inertial cavitation have to be monitored and controlled in real-time. In the literature, several methods have been proposed to quantify and characterize the cavitation effects. Some are using the MRI [50] and orther are using an ultrasound receiver [51] to characterize the backscattered ultrasound signals from the tissue. Despite the recent developments of cavitation monitoring methods under MRI, the latter technique using an ultrasound receiver is now by far the most popular and is referred as Passive Cavitation Detection (PCD). In the scoop of the thesis, PCD has been investigated for instance, to monitor thermal lesion [52] or to monitor cavitation effects during noninvasive cardiac stimulation [49].

PCD characterizes the cavitation activity by analyzing the ultrasound signal backscattered from the focus. This activity is illustrated in Figure 2.24, extracted from [53].

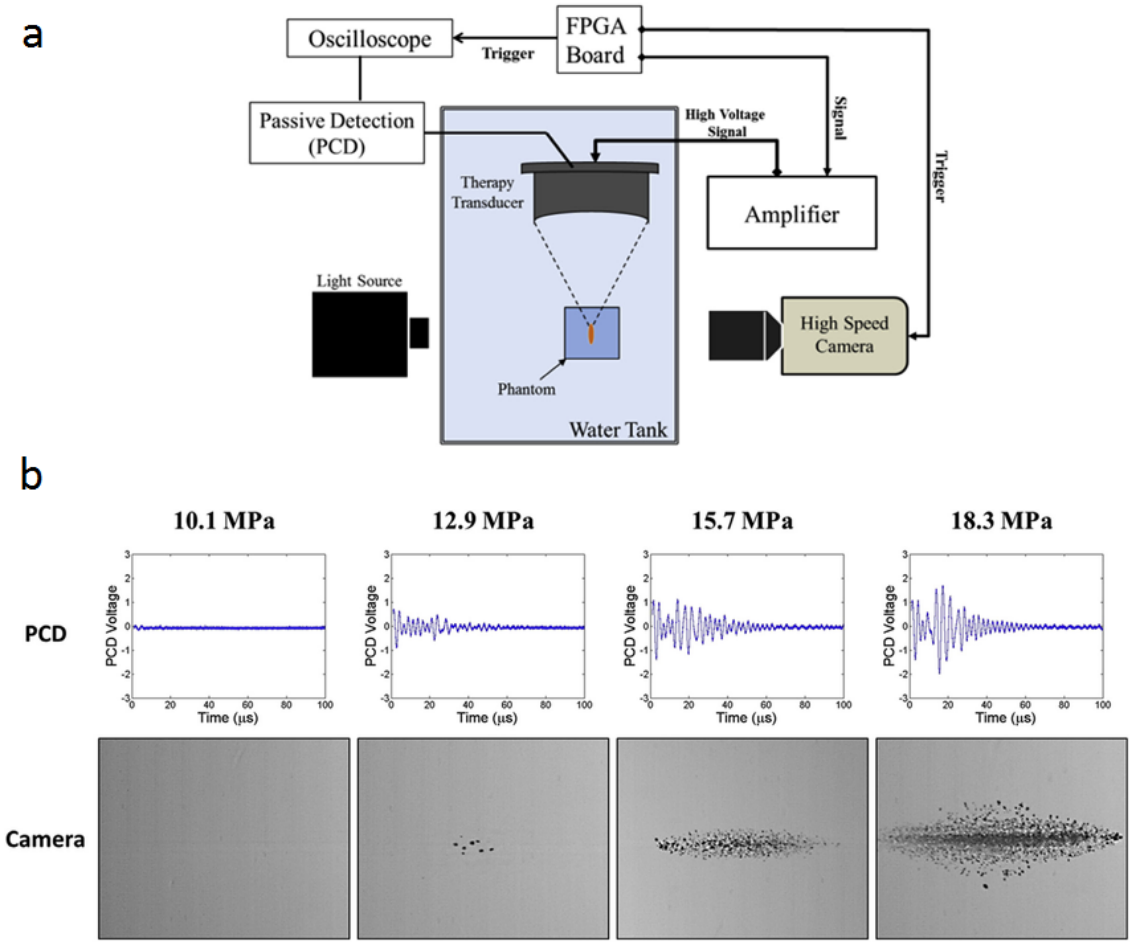

Figure 2.24: Cavitation detection. A: Experimental setup showing the focus of the histotripsy transducers aligned inside tissue phantoms containing perfluoropentane, perfluorohexane or no nanodroplets. Cavitation was monitored with high-speed optical imaging and passive cavitation detection using one of the therapy elements. FPGA 5 field-programmable gate array,PCD 5 passive cavitation detection B: Sample passive cavitation detection (PCD) signals (top) and high-speed optical imaging (bottom) were used for cavitation detection for cavitation threshold experiments. Results indicated good agreement between the two methods. Representative images shown above are from application of 1.5-MHz histotripsy pulses to tissue phantoms containing perfluorohexane nanodroplets.

On Figure 2.24, the PCD signal amplitude is correlated to the amount of cavitation observed by the camera. There are several different ways to interpret the signals acquired by PCD, i.e. to distinguish between stable cavitation and inertial cavitation. On the one hand, stable cavitation is closely related to ultrasound frequency harmonic power. This metric has been correlated to the treatment efficacy in several studies without damaging the underlying tissue [54]. On the other hand, the root-mean-square amplitude, in the frequency domain, of the broadband noise within a frequency window located between the harmonic peaks was introduced as a descriptor of the inertial cavitation. This metric was correlated to endothelial cell damage and hemolysis in vivo in several studies [55, 56].

2.3 Signal processing

Time-frequency maps were derived from the backscattered temporal signal using a customized spectrogram function (Hamming window, 98 % overlap, 1024-point Fast Fourier Transform in MATLAB 2015b, Mathworks, MA, USA). Because bubble oscillations along the acoustic excitation are non-linear (stable cavitation) the PCD will detect harmonic modes in the frequency spectrum. Bubble collapse and jet, more generally described as inertial cavitation, induces broadband noise. Therefore, detection of broadband response is the signature of inertial cavitation. The frequency spectra of backscattered acoustic emissions were used to infer the cavitation behavior of the microbubbles in the focal region. This was performed within the 1.2–40 MHz frequency band (f_1-f_2) in order to avoid perturbation induced by the fundamental frequency.

The Stable cavitation dose was defined as:

$$SCD = \int_{t=0}^{T} \sum_{i>f_1}^{f_2} \sqrt{S_i^2(t)} dt \tag{2.9}$$

where $S_i(t)$ is the amplitude of the i-th harmonic on the time-frequency map, T the total duration of the ultrasonic pulse. To better represent the temporal variation and the transient characteristic of the cavitation activity during the ultrasonic exposure two other metrics SCD_{min} and SCD_{max} where defined as follows:

$$SCD_{min} = \sum_{i>f_1}^{f_2} \min_t \left(\sqrt{S_i^2(t)} \right) .T \tag{2.10}$$

$$SCD_{max} = \sum_{i>f_1}^{f_2} \max_t \left(\sqrt{S_i^2(t)} \right) .T \tag{2.11}$$

In order to remove the harmonic (n.f_0, n is a positive integer), sub-harmonic ($\frac{f0}{n}$) and ultra-harmonic ($\frac{k.f0}{2}$, k is an odd positive integer) frequencies produced by stable cavitation, the response within a 200-kHz bandwidth around each harmonic and each sub- and ultra-harmonic frequency were filtered out in order to obtain the broadband signal $S_{bb}(f,t)$.

The Inertial cavitation dose and two derived metrics were defined as:

$$ICD = \int_{t=0}^{T} \int_{f=f_1}^{f_2} \sqrt{S_{bb}^2(f,t)} .df.dt \tag{2.12}$$

$$ICD_{min} = \int_{f=f_1}^{f_2} \min_t \left(\sqrt{S_{bb}^2(f,t)} \right) .df.T \tag{2.13}$$

$$ICD_{max} = \int_{f=f_1}^{f_2} \max_t \left(\sqrt{S_{bb}^2(f,t)} \right) .df.T \tag{2.14}$$

In Chapter 3, we have investigated PCD as a surrogate for cavitation effects and a possible predictor of the success-rate of cardiac stimulation.

2.4 References

[1] Michael Schacht Hansen and Thomas Sangild Sørensen. "Gadgetron: An open source framework for medical image reconstruction". en. In: *Magnetic Resonance in Medicine* (2013).

[2] Matt A. Bernstein et al. *Handbook of MRI pulse sequences*. eng. Amsterdam: Elsevier, Academic Press, 2004.

[3] Robert W Brown et al. *Magnetic resonance imaging: physical principles and sequence design*. English. 2014.

[4] Mark A. Griswold et al. "Generalized autocalibrating partially parallel acquisitions (GRAPPA)". In: *Magnetic Resonance in Medicine* (June 2002).

[5] Klaas P. Pruessmann et al. "SENSE: sensitivity encoding for fast MRI". In: *Magnetic resonance in medicine* (1999).

[6] Martin Uecker et al. "ESPIRiT-an eigenvalue approach to autocalibrating parallel MRI: Where SENSE meets GRAPPA". en. In: *Magnetic Resonance in Medicine* (Mar. 2014).

[7] Michael Lustig and John M. Pauly. "SPIRiT: Iterative self-consistent parallel imaging reconstruction from arbitrary k-space". en. In: *Magnetic Resonance in Medicine* (2010).

[8] Markus Barth et al. "Simultaneous multislice (SMS) imaging techniques: SMS Imaging". en. In: *Magnetic Resonance in Medicine* (Jan. 2016).

[9] Michael K. Stehling et al. "Echo-planar imaging: magnetic resonance imaging in a fraction of a second". In: *Science* (1991).

[10] Mehdi Poustchi-Amin et al. "Principles and applications of echo-planar imaging: a review for the general radiologist". In: *Radiographics* (2001).

[11] Robert Frost et al. "Scan time reduction for readout-segmented EPI using simultaneous multislice acceleration: Diffusion-weighted imaging at 3 and 7 Tesla: blipped-CAIPI rs-EPI". en. In: *Magnetic Resonance in Medicine* (July 2015).

[12] Jing Chen et al. “Optimization of encoding gradients for MR-ARFI”. In: *Magnetic Resonance in Medicine* (Apr. 2010).

[13] Felix A. Breuer et al. “General formulation for quantitative G-factor calculation in GRAPPA reconstructions”. en. In: *Magnetic Resonance in Medicine* (Sept. 2009).

[14] Tao Zhang et al. “Coil compression for accelerated imaging with Cartesian sampling”. en. In: *Magnetic Resonance in Medicine* (Feb. 2013).

[15] Souheil J Inati et al. *A Fast Optimal Method for Coil Sensitivity Estimation and Adaptive Coil Combination for Complex Images*.

[16] Souheil J Inati et al. *A Solution to the Phase Problem in Adaptive Coil Combination*.

[17] John De Poorter. “Noninvasive MRI thermometry with the proton resonance frequency method: study of susceptibility effects”. In: *Magnetic Resonance in Medicine* (1995).

[18] Claudia Weidensteiner et al. “Stability of real-time MR temperature mapping in healthy and diseased human liver”. eng. In: *Journal of magnetic resonance imaging: JMRI* (2004).

[19] Bruno Quesson et al. “Magnetic resonance temperature imaging for guidance of thermotherapy”. en. In: *Journal of Magnetic Resonance Imaging* (Oct. 2000).

[20] Bruno Quesson et al. “Real-time volumetric MRI thermometry of focused ultrasound ablation in vivo: a feasibility study in pig liver and kidney”. en. In: *NMR in Biomedicine* (Feb. 2011).

[21] Paul Baron et al. “Correction of proton resonance frequency shift MR-thermometry errors caused by heat-induced magnetic susceptibility changes during high intensity focused ultrasound ablations in tissues containing fat”. en. In: *Magnetic Resonance in Medicine* (2014).

[22] Nick Todd et al. “Hybrid proton resonance frequency/T1 technique for simultaneous temperature monitoring in adipose and aqueous tissues”. en. In: *Magnetic Resonance in Medicine* (2013).

[23] Stephen A. Sapareto and William C. Dewey. “Thermal dose determination in cancer therapy”. In: *International Journal of Radiation Oncology*Biology*Physics* (Apr. 1984).

[24] W. C. Dewey. “Arrhenius relationships from the molecule and cell to the clinic”. en. In: *International Journal of Hyperthermia* (Jan. 1994).

[25] Gerard C. van Rhoon et al. "CEM43\textdegree\C thermal dose thresholds: a potential guide for magnetic resonance radiofrequency exposure levels?" In: *European radiology* (Aug. 2013).

[26] Claudia Weidensteiner et al. "Real-time MR temperature mapping of rabbit liver in vivo during thermal ablation". In: *Magnetic resonance in Medicine* (2003).

[27] Kathryn Nightingale et al. "Acoustic radiation force impulse imaging: in vivo demonstration of clinical feasibility". In: *Ultrasound in Medicine & Biology* (2002).

[28] Elena A Kaye et al. "Rapid MR-ARFI method for focal spot localization during focused ultrasound therapy". en. In: *Magnetic Resonance in Medicine* (Mar. 2011).

[29] Yoni Hertzberg et al. "Rapid method for assessing relative tissue stiffness using MR acoustic radiation force imaging". en. In: *International Journal of Imaging Systems and Technology* (Mar. 2014).

[30] Jonathan Vappou et al. "Quantitative viscoelastic parameters measured by harmonic motion imaging". In: *Physics in Medicine and Biology* (June 2009).

[31] Rémi Souchon et al. "Transient MR elastography (t-MRE) using ultrasound radiation force: Theory, safety, and initial experiments in vitro". In: *Magnetic resonance in medicine* (2008).

[32] Tao Wu et al. "MR imaging of shear waves generated by focused ultrasound". In: *Magnetic resonance in medicine* (2000).

[33] Samuel Callé et al. "Temporal analysis of tissue displacement induced by a transient ultrasound radiation force". In: *The Journal of the Acoustical Society of America* (Oct. 2005).

[34] S. D. Swanson et al. "MRI detection of shear wave propagation: remote palpation with focused ultrasound". In: *Proceedings of the 6th ISMRM Annual Meeting, Sydney, Australia*. 1998.

[35] Olivier Seror et al. "Real time monitoring of radiofrequency ablation based on MR thermometry and thermal dose in the pig liver in vivo". In: *European radiology* (Feb. 2008).

[36] S Toupin et al. "Combination of principal component analysis and optical-flow motion compensation for improved cardiac MR thermometry". In: *Physics in Medicine and Biology* (Feb. 2017).

[37] Samuel Pichardo et al. “In vivo optimisation study for multi-baseline MR-based thermometry in the context of hyperthermia using MR-guided high intensity focused ultrasound for head and neck applications”. eng. In: *International Journal of Hyperthermia: The Official Journal of European Society for Hyperthermic Oncology, North American Hyperthermia Group* (Dec. 2014).

[38] De Senneville et al. “Atlas-based motion correction for online MR temperature mapping”. In: *Image Processing, 2004. ICIP'04. 2004 International Conference on.* IEEE, 2004.

[39] Baudouin Denis De Senneville et al. “Real-time adaptive methods for treatment of mobile organs by MRI-controlled high-intensity focused ultrasound”. In: *Magnetic Resonance in Medicine* (2007).

[40] Viola Rieke et al. “Referenceless PRF shift thermometry”. en. In: *Magnetic Resonance in Medicine* (June 2004).

[41] B. D. de Senneville et al. “MR-Guided Thermotherapy of Abdominal Organs Using a Robust PCA-Based Motion Descriptor”. In: *IEEE Transactions on Medical Imaging* (Nov. 2011).

[42] Gregory Maclair et al. “PCA-based magnetic field modeling: Application for online MR temperature monitoring”. In: *International Conference on Medical Image Computing and Computer-Assisted Intervention*. Springer, 2007.

[43] Valéry Ozenne et al. “Improved cardiac magnetic resonance thermometry and dosimetry for monitoring lesion formation during catheter ablation”. In: *Magnetic resonance in medicine* (2017).

[44] Solenn Toupin et al. “Feasibility of real-time MR thermal dose mapping for predicting radiofrequency ablation outcome in the myocardium in vivo”. In: *Journal of Cardiovascular Magnetic Resonance* (Jan. 2017).

[45] De Senneville et al. “Feasibility of fast MR-thermometry during cardiac radiofrequency ablation”. en. In: *NMR in Biomedicine* (Apr. 2012).

[46] Kathryn E. Hitchcock et al. “Ultrasound-enhanced delivery of targeted echogenic liposomes in a novel ex vivo mouse aorta model”. eng. In: *Journal of Controlled Release: Official Journal of the Controlled Release Society* (June 2010).

[47] Saurabh Datta et al. “Ultrasound-Enhanced Thrombolysis Using Definity® as a Cavitation Nucleation Agent”. en. In: *Ultrasound in Medicine & Biology* (Sept. 2008).

[48] K. Hynynen et al. “Noninvasive MR imaging-guided focal opening of the blood-brain barrier in rabbits”. eng. In: *Radiology* (Sept. 2001).

[49] Amit Livneh et al. “Extracorporeal acute cardiac pacing by High Intensity Focused Ultrasound”. en. In: *Progress in Biophysics and Molecular Biology* (Aug. 2014).

[50] Hsu-Hsia Peng et al. “Real-time monitoring of inertial cavitation effects of microbubbles by using MRI: In vitro experiments: Monitoring Microbubble Cavitation Effects Using MRI”. en. In: *Magnetic Resonance in Medicine* (Dec. 2015).

[51] S. I. Madanshetty and R. E. Apfel. “Acoustic microcavitation: enhancement and applications”. eng. In: *The Journal of the Acoustical Society of America* (Sept. 1991).

[52] ¿C. C. Coussios et al. “Role of acoustic cavitation in the delivery and monitoring of cancer treatment by high-intensity focused ultrasound (HIFU)”. en. In: *International Journal of Hyperthermia* (Jan. 2007).

[53] Eli Vlaisavljevich et al. “Effects of Droplet Composition on Nanodroplet-Mediated Histotripsy”. en. In: *Ultrasound in Medicine & Biology* (Apr. 2016).

[54] Fabrice Marquet et al. “Real-Time, Transcranial Monitoring of Safe Blood-Brain Barrier Opening in Non-Human Primates”. en. In: *PLoS ONE* (Feb. 2014). Ed. by Stefan Liebner.

[55] Joo Ha Hwang et al. “Correlation between inertial cavitation dose and endothelial cell damage in vivo”. eng. In: *Ultrasound in Medicine & Biology* (Oct. 2006).

[56] Wen-Shiang Chen et al. “A comparison of the fragmentation thresholds and inertial cavitation doses of different ultrasound contrast agents”. In: *The Journal of the Acoustical Society of America* (2003).

CHAPTER 3

Non-invasive cardiac pacing under MRI

Contents

3.1 Introduction

This chapter presents the proof of feasibility of non-invasive cardiac pacing, using short pulses of HIFU. This technique could potentially bridge the current need of a non-invasive pacing device for patients in heart failure without the need of surgical procedures. The principal investigator of this project was Fabrice Marquet, postdoctoral researcher at LIRYC institute and I closely worked with him to develop this new application of HIFU, mainly on technological point-of-view.

Personal contributions:

- Participation in the study design.
- Realizing of all electronic components and signal acquisition setup for EP recordings.
- Implementation of the MR-ARFI se-ssEPI sequence.
- Participation to all ex vivo and animal experimentations.
- ARFI displacement data post-treatment and production of figures.
- Participation in the PCD design and data acquisitions.

3.1.1 Literature

In current literature, ultrasounds have been shown, since 1929 [1] to be capable to produce Premature Ventricular Contractions (PCV). Since then, several studies described ultrasound effect on the myocardium on frogs [2], rats [3],[4] and piglets [5].

Initially, most of the studies were aimed to set safety thresholds for cardiac ultrasound imaging, especially when an injection of ultrasound contrast agent (UCA) is performed. It is only in 2014 that Livneh et al. [3] were the first to identify clinical applications of PVC. This ultrasound bioeffect on the heart is still not well established, however two actors could play a predominant role [6]: namely cavitation and the acoustic radiation force, both acting on the reversibility of the electromechanical compling of cardiomyocytes. At the cardiomyocyte level, stretch-activated ion channels present on the cell membrane are though to open in response to mechanical deformation induced by ultrasound steaming [7]. This channel opening could trigger cells depolarization, confirming the active role of cavitation processes in cardiac stimulation. These observations are confirmed at the

macroscopic level, where UCA have been shown to lower the required acoustic pressure to induce PVC [8]. Alternatively to cavitation effects, a recent study [9] shows the possibility to pace the heart by mechanically poking the heart. This study could corroborate the active role of macro displacements and the action of the acoustic radiation force in cardiac stimulation.

From a clinical perspective non-invasive cardiac stimulation responds to a real need to have a non-invasive cardiac pacing device and could be applied in various situations:

- For hemodynamic studies in order to analyze the possible benefits of atrial chamber pacing in obstructive cardiomyopathy or of optimal atrio-ventricular delay programming in complete atrio-ventricular block patients. This technique could also be used in CRT, to optimize the RV and LV leads placement and assessing efficacy of programming settings (atrio-ventricular delay and interventricular interval).
- For temporary pacing in patients suffering from bradycardia or any clinical condition with risks of cardiac asystole. As the ultrasound beam can be focused on very specific cardiac zones, temporary pacing could be applied to the atrium in case of sinus node disease, to the ventricle in case of atrio-ventricular block or even at both sites to restore atrio-ventricular synchronization in patient whom hemodynamic support must be achieved.
- In the context of electrophysiology for terminating tachyarrhythmia that compromise hemodynamics, or for examining the inducibility of tachyarrhythmia.

For this application two stages of development can be identified. Firstly cardiac pacing in case of bradycardia. This involves to pace the heart anywhere in the ventricles. This stage only requires to have enough ultrasound energy at the focus to induce a cardiac stimulation. Secondly multisite pacing in the context of resynchronization therapies. This could potentially screen the 1/3 of patients who are non-respondent to the therapy and undergo an heavy surgical procedure without any health benefit. For the respondents, lead placements could be optimized to produce the maximum hemodynamic response. For this advanced stage, motion compensation strategies and management of the acoustic windows to target different heart cavities will be required.

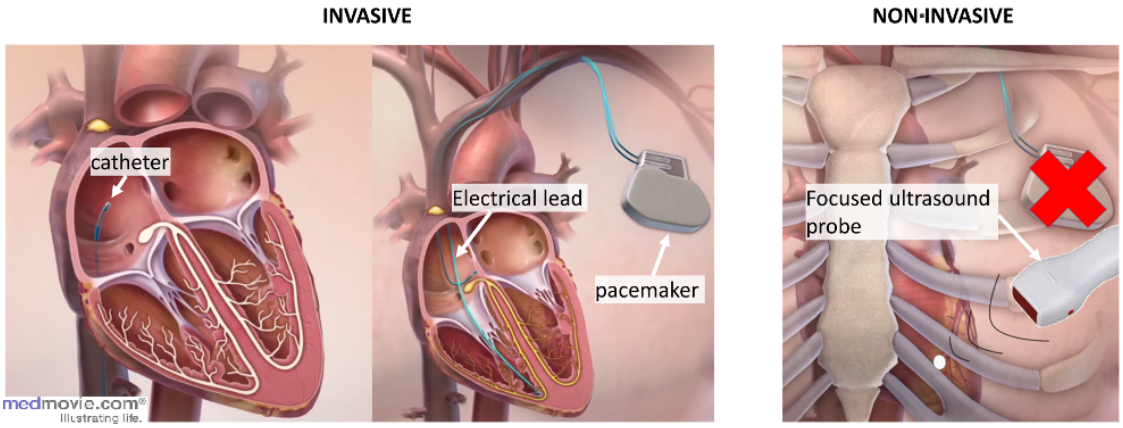

Figure 3.1: Non-invasive cardiac pacing On the left is a representation of the current invasive procedure to pace the heart. On the right is what we aim for: non-invasive pacing using focused ultrasounds.

As of now, the potential benefit of non-invasive stimulation is well-established however the clinical applicability is still difficult to assess because small animal models artificially circumvent technical difficulties such as the limited acoustic window (acoustic reflection/absorption by the rib cage and the lungs) or respiratory and cardiac motions.

3.1.2 Objectives

The objective of this research project is to develop contactless cardiac pacing instrumentation and methods and to validate this non-invasive approach on large animals and prepare the transfer of this technology to patients. Improvement of current therapeutic practices through the use focused ultrasound technology as a non-invasive temporary stimulation device may offer new approaches for the treatment of heart rhythm disorders, with the objective of improving therapeutic efficacy. In addition, during this study we have identified two biomarkers of interest for both safety and procedure monitoring purposes.

3.2 Materials and methods

3.2.1 Isolated heart perfusion in Langendorff mode

In LIRYC institute, an MR-compatible Langendorff heart setup has been developed by Vaillant et al.[10] (see Figure 3.2). This setup allows a heart from large animal to beat inside the magnet and allows monitoring of pressure and EP signals, besides conventional cardiac MR-acquisitions. This model was the model of choice to determine stimulation thresholds inside the myocardium:

1. It avoids respiratory motion and optimize the ultrasonic acoustic window.
2. It allows to estimate the acoustic pressure at the focus without anatomical structures in the beam path (ribs, lungs).
3. It allows monitoring of EP and cardiac pressures in an easier way than in vivo.

3.2.1.1 Animal preparation

The protocol was approved by the local Animal Research Ethics Committee (Comité d'Ethique en Expérimentation Animale de Bordeaux - CEEA50) and all experiments were performed in accordance with the approved guidelines. Pigs (Large White x Landrace, ∼40 kg, 10 animals for ex vivo validation, 4 animals for in vivo proof of concept) were premedicated with ketamine (20 $mg.kg^{-1}$) and acepromazine (1 $mg.kg^{-1}$) injected IM.Induction of anesthesia was realized with intravenous bolus of ketamine (15 $mg.kg^{-1}$) and midazolam (1.5 $mg.kg^{-1}$). After induction of anesthesia, animals were intubated and ventilated, and received an injection of heparin (2.5 $mg.kg^{-1}$). Anesthesia was maintained with ketamine and midazolam (40 $mg.kg^{-1}.h^{-1}$ and 2 $mg.kg^{-1}.h^{-1}$ respectively). During the in vivo experiments the animals were injected with ultrasound contrast agents using SonoVue (Bracco, Italy), mean terminal half-life: 12 min, range from 2 min to 33 min. Two consecutive 0.1 $mL.kg^{-1}$ boli intravenous injection were performed in each animal.

3.2.1.2 Heart extraction and surgery preparation

The thorax was opened and blood from each animal was col- lected (∼ 3 L) via an 8Fr introducer inserted in the right jugular vein. Vascular filling was performed using Voluven IV infusion at a pace corresponding to the debit of the blood collected via the femoral vein. Cardiac arrest was induced in vivo by crossclamping of the ascending aorta and direct injection in the aortic root of 1 L of cold (4 °C) cardioplegic Celsior (Genzyme, Saint-German-en-Laye, France) solution, following by a rapid excision and immersion in a cold 0.9 % saline solution. The extraction protocol was based on standard clinical extraction [11].

3.2.1.3 Isolated heart perfusion in Langendorff mode.

The aorta and the pulmonary artery were cannulated. The pulmonary veins and the inferior and superior vena cava were sutured to limit leaks. The entire coronary flow goes into the coronary sinus, the right atrium and ventricle, and was collected through the pulmonary artery. The hearts were then placed onto a polyurethane membrane (transparent to ultrasound) in a plexiglas thermoregulated tank and reperfused in the Langendorff

mode at 60–70 mmHg of coronary perfusion pressure. When necessary, hearts were defibrillated at 10–30 J. This setup offers loaded ventricles with the perfusion medium from the coronary vascular bed, resulting in an isovolumetric contraction. Perfusion of the heart was realized with autologous blood diluted with a Tyrode buffer (v/v: 1/3, gassed with O_2/CO_2= 95/5 %, pH 7.4) maintained at 38 °C. Tyrode buffer contains physiological concentrations of hormones (8 nM insulin, 5 nM epinephrine) and metabolic substrates (16 mM glucose, 0.5 mM pyruvate, 1 mM lactate)[12].

3.2.1.4 Ultrasonic characteristics

In situ focal pressures were determined taking into account absorption in the diluted blood and heart tissue (respectively 0.20 dB.MHz^{-1}.cm^{-1} and 0.52 dB. MHz^{-1}.cm^{-1}) and acoustic loss due to electronic deflection applied during the experiment to steer the beam away from the transducer natural focus (attenuation of 2.50 dB.cm^{-1} laterally and 0.45 dB.cm^{-1} axially, measured by hydrophone in a water tank).

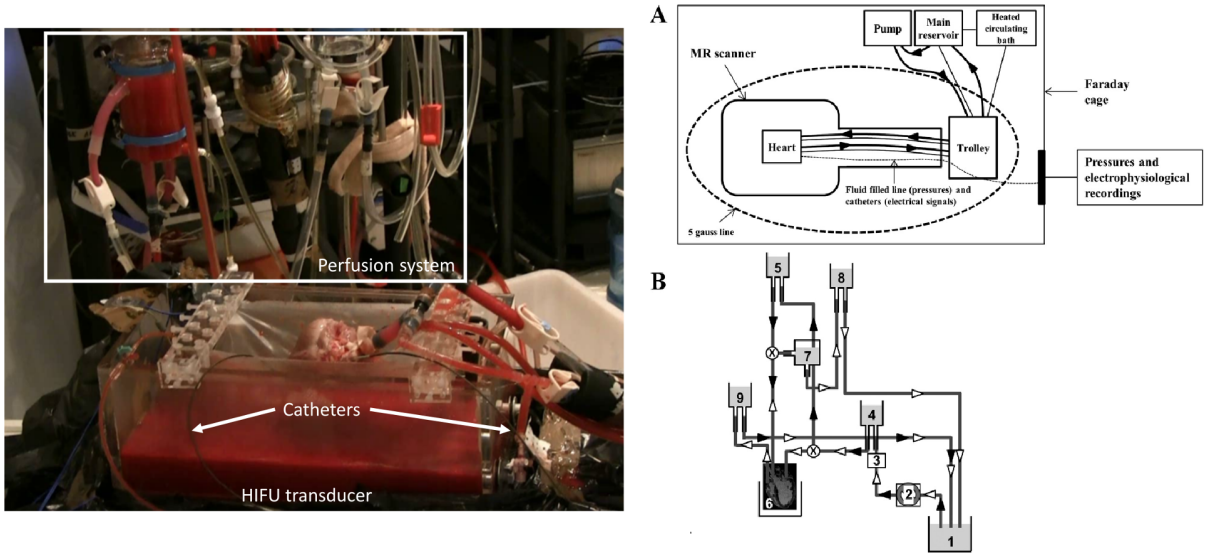

Figure 3.2: Langendorff setup..
Schematic view of the MR-compatible setup for the isolated working heart. A: complete setup inside the Faraday cage. The electrical equipment (pump and heated circulating bath) was placed outside the 5-gauss line (dashed line). The pressures (intraventricular pressure, preload, and afterload) were connected via fluid-filled line to pressure transducers located outside the Faraday cage. The reservoirs for working perfusion were placed on a trolley, which were fixed to the MR scanner bed. B: working perfusion setup in detail:1: main reservoir,2:pump,3: oxygenator,4: preload,5:Langendorff reservoir,6: heart chamber,7: compliance chamber,8: left ventricle (LV) afterload,9: right ventricle (RV) afterload. The reperfusion is started in the Langendorff mode (black arrow heads) and is switched in working mode (white arrow heads) after cardiac stabilization. In the working mode, the perfusate from the main reservoir (1) is pumped (2) through the oxygenator (3) and enters into the left atrium (LA) with a LA preload of 10–15 mmHg (4). At each atrial systole, perfusate flows into the LV and is ejected through the aorta during the ventricular contraction. The perfusate enters into the compliance chamber (7) and then into the LV afterload (8), which is settled at 60–70 mmHg. The coronary flow goes into the coronary sinus, the right atrium (RA), and then the RV. At each ventricular contraction, the coronary flow is ejected into the pulmonary artery. For the unloaded RV group, the RV afterload (9) was 0 mmHg, and, for the loaded RV group, the RV afterload was 10–15 mmHg

3.2.2 Physiological response monitoring

3.2.2.1 Electrical measurements

The EP signals were monitored using either three dipole MR-compatible pacemaker leads or three quadri-polar MR-compatible catheters inserted into the right ventricle, the left ventricle and the right atrium. The recoding was performed on a clinical Bard system (Bard Inc., NJ, USA). In order to prevent artifacts on MR-images and limit the electric power received by the Bard system during MR-acquisition, we have designed band-rejecter filters at 64 MHz (see Figure 3.3) which is the proton resonance frequency at 1.5 T. Each transmission line was filtered.

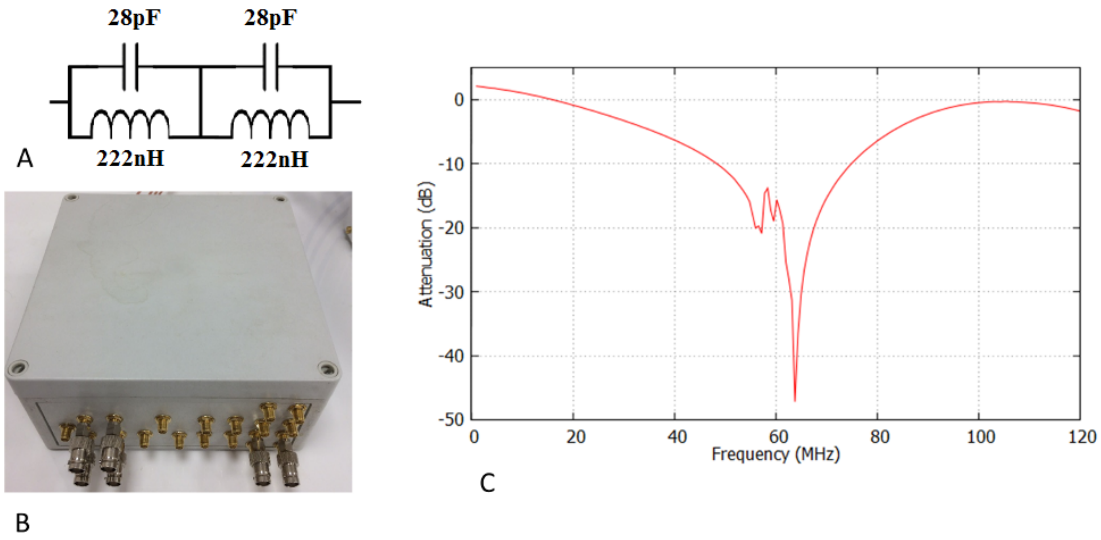

Figure 3.3: 64 MHz band rejecter filter. A) LC band rejecter filter circuit B) Box of 20 band-rejecter filters C) Typical attenuation curve obtained after filtering

In this study, we needed to synchronize the sonication on cardiac cycle. To this end, we have developed a custom trigger generator (see Figure 3.4) which can be set to synchronize the ultrasonic emissions and the desired delay to the electric signal of any heart cavities. This prototype can be divided in two parts, firstly a differential two stages operational amplifier circuit (see red box on Figure 3.4) and secondly, a Schmitt trigger circuit to produce the trigger (see green box on Figure 3.4). An additional electronic component was added to avoid multiple trigger generation (not shown on Figure 3.4).

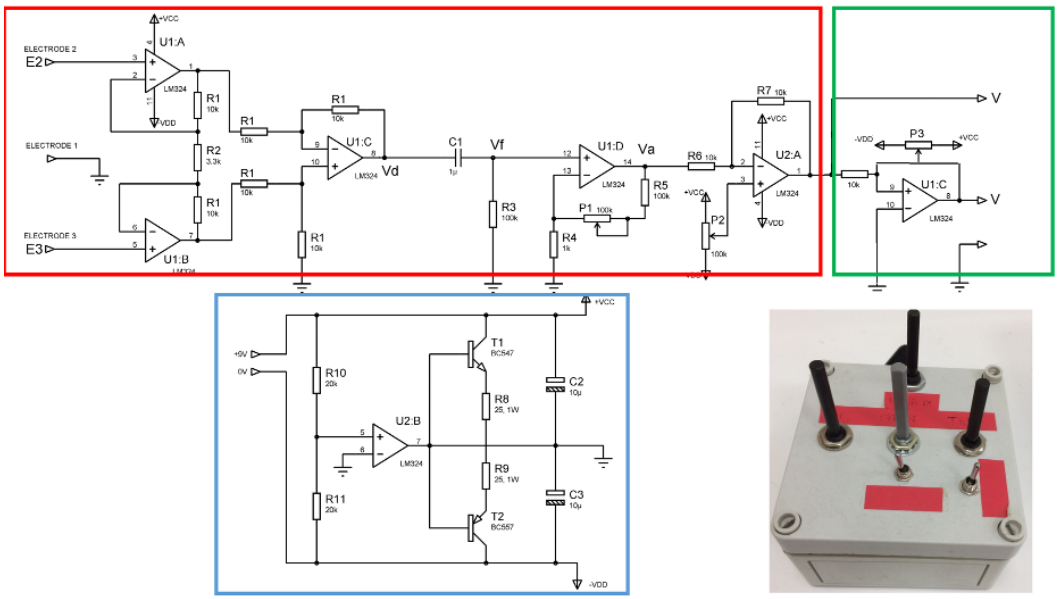

Figure 3.4: ECG prototype. The Blue box shows the power supply circuit, the red box shows the two stages differential circuit and the green box shows the Schmitt trigger circuit which generates the trigger

In this study, electrophysiological recording reported in figures were not performed

during MR-acquisitions due to artifacts generated by the MR pulse sequence.

3.2.2.2 Intraventricular pressure measurements

Cardiac contraction was attested by intracardiac pressure measurements. An home-made intraventricular pressure catheter was inserted into the left ventricle via the apex and connected to a fluid-filled piezoelectric pressure transducer for continuous monitoring of left ventricular pressure (EMKA-IOX2 data acquisition system, EMKA Technologies, VA, USA).

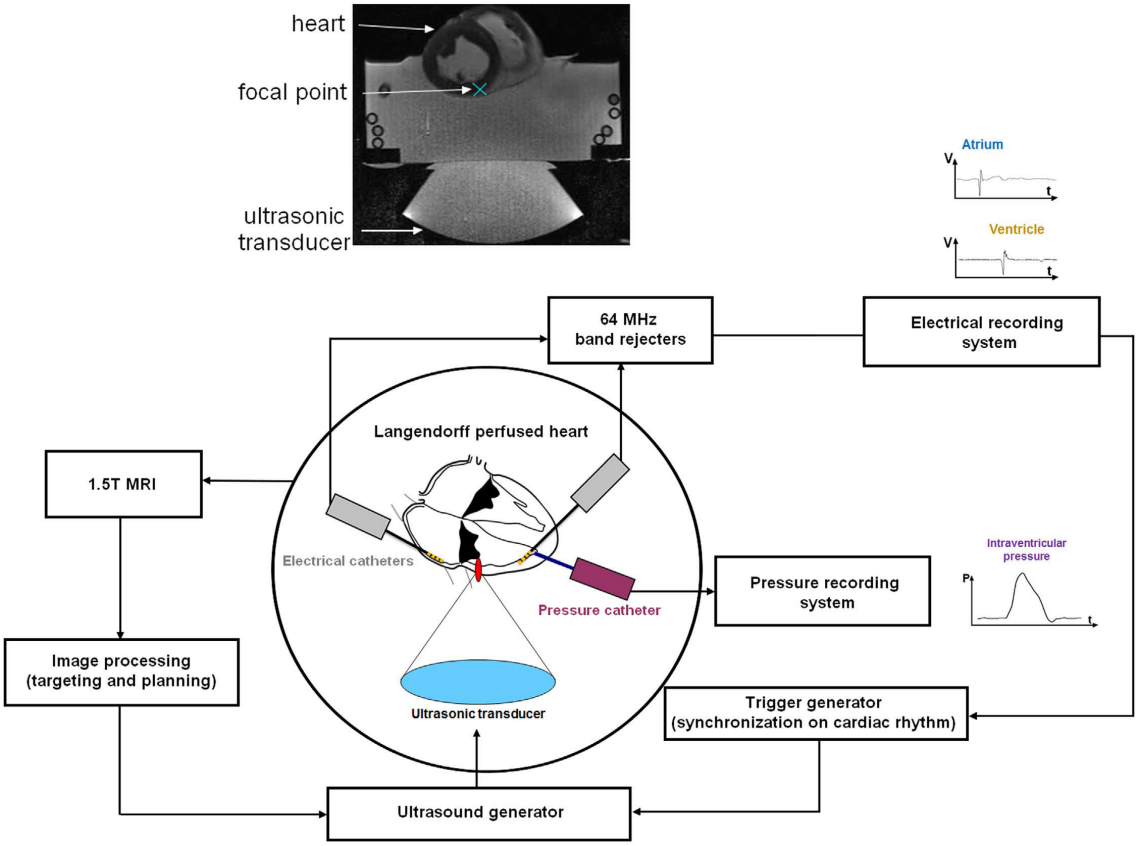

Figure 3.5: Schematic of the ex vivo experimental setup and corresponding MR image. A beating pig heart (Langendorff perfusion) is set in a tank filled with a mix of Tyrode buffer and autologous blood. The ultrasonic probe (256 elements phased-array operating at 1 MHz) is positioned underneath and can sonicate the different heart cavities through the acoustic window. This setup is placed inside a 1.5T MR scan for image guidance. Electrical and intraventricular recordings are recorded in the different heart cavities from MRI compatible catheters and the ultrasound pulses are synchronized on the heart cycle with adjustable delays.

3.2.3 Experimental protocol

3.2.3.1 Ex vivo and in vivo stimulation

Ex vivo acoustic stimulation threshold was determined performing 756 sonications in the right atrium (83 sonications), the left (431 sonications) and the right ventricles

(242 sonications) in 10 ex vivo beating hearts from pigs. Ex vivo continuous pacing was performed 11 times in 3 different pig hearts. Ventricular tachycardia was induced 6 times in 2 different pig hearts. Multisite stimulation was performed 15 times in 2 different hearts.In vivo non-invasive stimulation proof of concept was shown performing 314 sonications in 4 anesthetized pigs including 42 sonications without ultrasound contrast agent in the first two animals. Correlation of cardiac susceptibility to stimulation with ultrasound contrast agent pharmacokinetic was performed in the last two animals (total of 84 sonications). Preliminary comparison of short and long ultrasonic pulses was performed in the last animal (total of 74 sonications).

During in vivo and ex vivo experiments, the stimulation protocol followed these steps:

1. Targeting: MR images were recorded using a balanced steady-state free precession sequence (TE/TR/FA/BW = 1.36 ms/493 ms/80°, 1149 Hz.pixel^{-1}, spatial resolution 1x1 mm^2, slice thickness 3 mm, 256x256, 40 slices, 3 stacks acquired in transverse, sagittal and coronal orientations) to select the location of the stimulation site and to adjust beam focusing characteristics (mechanical positioning and electronic beam steering)

2. Sonication: the focus position was adjusted on the myocardium with a amplitude above the simulation threshold. If the heart didn't capture, we switched the position of the focus of several millimetres until consistent capture.

3.2.3.2 Data analysis

Ultrasound induced depolarization were identified by the following chain of events: ultrasound trigger representing the emission of the ultrasonic pulse, depolarization seen in the electrical recordings and mechanical contraction seen in the pressure recordings. To determine the stimulation thresholds, different values of stimulation acoustic amplitudes and durations were tested. Acoustic amplitudes ranged from 1.3 MPa to 10 MPa peak negative, and pulses duration ranged from 30 μs to 10 ms. For each amplitude-duration set, the success rate of inducing a premature ventricular contraction was measured. The stimulation was considered reliable when at least 90% success was observed for each amplitude-duration set, defining a stimulation threshold.

3.2.4 Feasibility of cardiac MR-ARFI monitoring

A ssSE-EPI ARFI sequence was implemented on the scanner. Similarly to the ssGE-EPI ARFI sequence presented in section 2.2.4, two bipolar MEG were inserted from each

side of the refocusing pulse (see Figure 3.7). Several parameters were available from the user interface (see Figure 3.6)

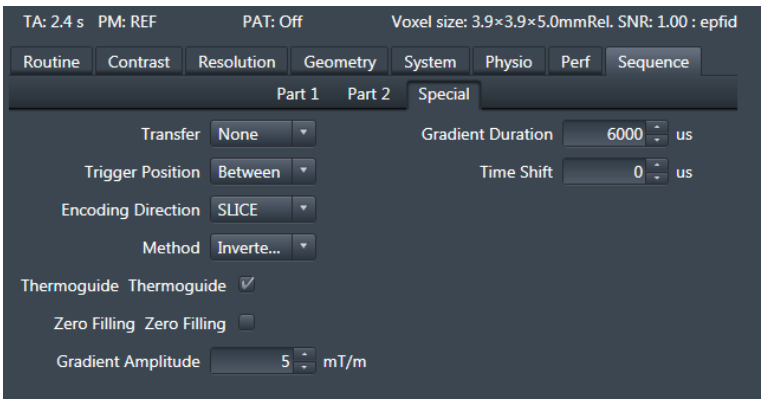

Figure 3.6: Sequence user interface:
Transfer: choose to reconstruct images on Siemens or with the Gadgetron
Thermoguide: activate the transfer from the Gadgetron to Thermoguide (visualization software)
Trigger Position: choose "when" to synchronize the ultrasound emission ["None" (no trigger), "Before" the MEG, "Between" the first and second lobe of MEG]
Encoding Direction: chose the direction of MEG ["READ","SLICE","PHASE"]; Method: ["ARFI" no MEG alternation, "Gradient alternation", "Trigger alternation"
Time Shift: additional delay between the first and second lobe of MEG
Trigger Time Shift: shift in time the position of the trigger from its initial position defined by Trigger Position

Sonication was performed on MEG from both sides and during the refocusing pulse (see Fig 3.11A). The sequence was then synchronized on the heart cycle and an additional delay could be adjusted to synchronize the sequence in the refractory or in the non-refractory period of the heart, respectively. The proof of feasibility of displacement monitoring was performed on three langendorff hearts. For each experiment, one coronal slice was position at the focus (see yellow box on Figure 3.11B). One acquisition slice was performed every heart beat with a specific delay from the R wave detection. Displacement map and physiological response (LV pressure and LV electrical activity) of the heart were recorded continuously. To observe elasticity variations along the cardiac cycle, MR-acquisitions were triggered from the R wave detection to the end of the cardiac cycle, by 20 ms steps, before the T wave, and by 50 ms steps after. For each step, 20 measurements were performed for a statistical relevance.

Sequence parameters were: FOV = 252x252 mm^2 Resolution = 2.25x2.25x5 mm^3 TE/TR = 50 ms/78 ms. The duration of MEG was $\Delta = 3$ and S_{ARFI} (see Figure 3.7 HIFU pulse was 12 ms (2 x Δ + Refocusing Time) at 420 W acoustic power.

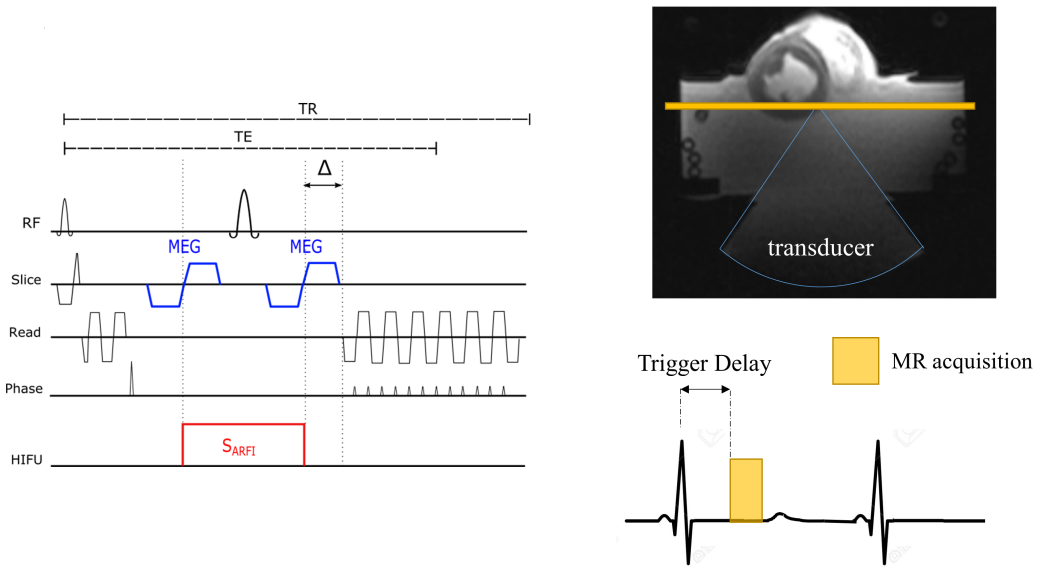

Figure 3.7: ARFI monitoring on the heart. A) shows the chronogram of the ssSE-EPI sequence with MEG represented in blue. Sonication is performed during the central lobe from both sides of the reofcussing pulse. B) shows an image of the heart where a single slice in coronal orientation is represented in yellow. The slice acquisition was synchronised on the ECG trace to freeze cardiac motions.

3.3 Results

Using the setup described previously, ultrasound-induced extra systole can be achieved. An example can be seen in Figure 3.8. On these recordings, three contractions in sinus rhythm are displayed before an ultrasonic stimulation attempt was made (5 MPa peak negative, 5 ms pulse length). This mechanical stimulus induced a ventricular depolarization followed by a retrograde conduction in the atrium, resulting in a PVC (peak-to-peak time delay of 580 ms compared to 650 ms in sinus rhythm) and lower maximum pressure (42 mmHg compared to 54 mmHg in sinus rhythm).

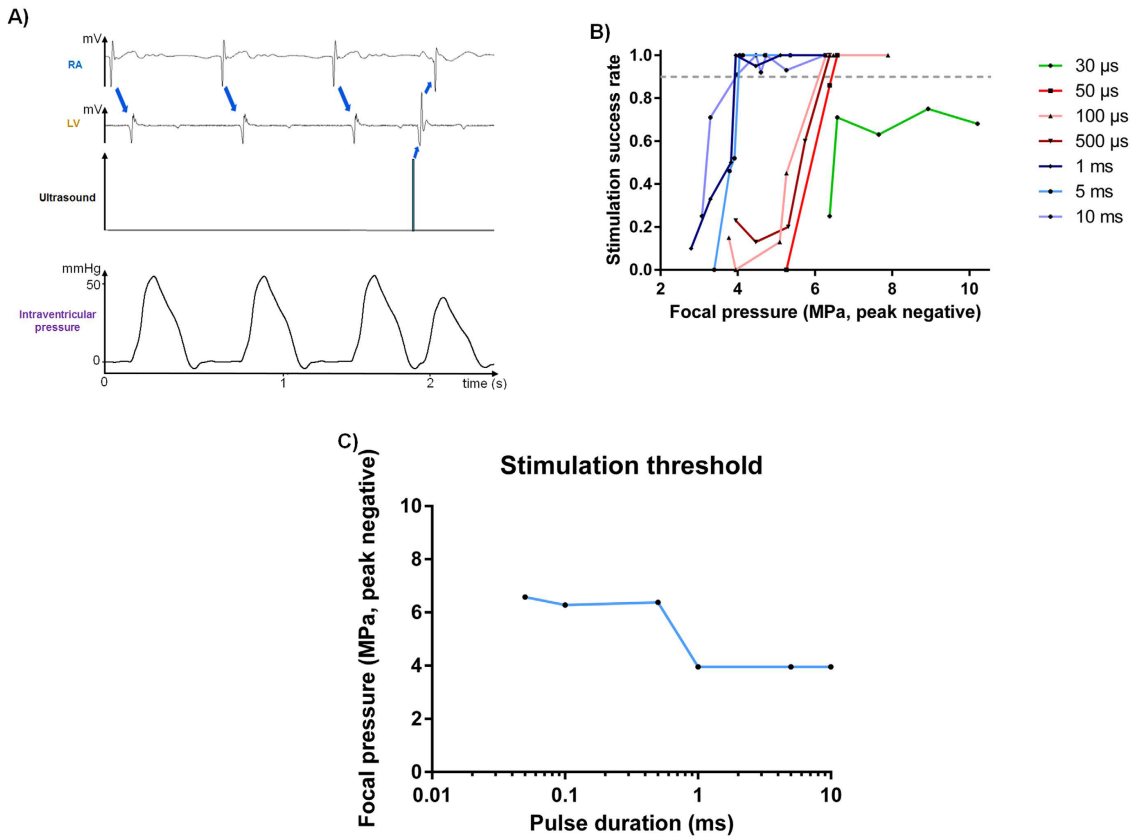

Figure 3.8: Example of ultrasound-induced premature ventricular contraction. Figure reports electrocardiograms for RA and LV, focus ultrasound signal and left intraventricular pressure. After three sinus rhythm beats, an ultrasonic pulse is sent after the absolute refractory period of the ventricle. A ventricular depolarization can be observed. Actual ultrasound-induced heart contraction was confirmed by intraventricular pressure measurements recorded simultaneously. (B) Stimulation success rate for different ultrasound pulse durations as a function of the acoustic pressure at focus. The grey dashed line shows the 90 % success rate threshold chosen. (C) Stimulation threshold ensuring at least 90 % stimulation in peak negative pressure reported as a function of the pulse duration.

The results of the 756 stimulation sites performed in the right atrium (RA, 83 sonications), and the left and right ventricles (431 and 242 sonications respectively) in 10 ex vivo beating hearts from pigs are depicted in Figure 3.8B. The success rate of stimulation for different pulse durations is plotted as a function of the acoustic pressure at the focus (peak negative). For each HIFU pulse duration tested ranging from 30 s to 10 ms, the success of stimulation increases with the acoustic pressure at focus. To determine the stimulation pressure threshold, the pressure values associated with a stimulation success rate of at least 90 % are reported as a function of pulse duration (Figure 3.8C). Two different pressure thresholds are highlighted: one around 4 MPa peak negative for HIFU pulse durations above 1 ms and one around 6 MPa peak negative for HIFU pulses ranging from 50 μs to 1 ms. For HIFU pulse durations shorter than 50 μs, the 90 % stimulation threshold was not reached in this study (10 MPa peak negative, maximal success rate around 70 %). The pressure values associated with a stimulation success rate observed a

similar decrease trend as compared to electrical pacing (see Figure 3.9)

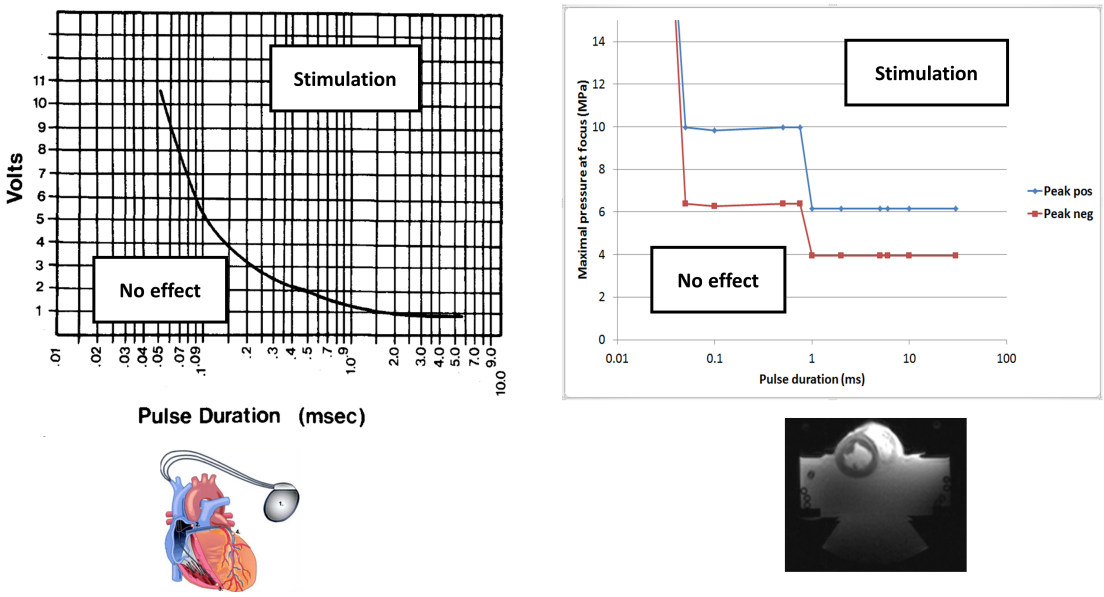

Figure 3.9: Comparison of stimulation threshold with conventional electrical pacing. On the left is represented electrical thresholds to induce a cardiac stimulation. The curve decreases as function of the pulse duration and the voltage applied. On the right is represented the curve of ultrasound thresholds for cardiac stimulation as function of pulse duration and acoustic pressure estimated at the focus. This curve was obtained using 10 ex vivo heart and more than 700 stimulation trials on different cardiac cavities.

3.3.1 Various ultrasound-induced electrical effects

An example of HIFU continuous pacing is depicted in Figure 3.10A. Spontaneous rate was around 100 bpm and the heart was paced at 120 bpm. As ECG gating was not used, the first pulse did not result in capture of the ventricles as it fell during the absolute refractory period after the spontaneous ventricular depolarization. Ventricular pacing was efficient from the second pulse. The actual mechanical contraction was again confirmed by the intraventricular pressure measurement. The first two rapid paced beats exhibited lower systolic pressure, then circulation progressively adjusted to the faster pace with restoration of the previous pressure after 6–7 beats. It has already been demonstrated that ventricular tachycardia can be induced by stimulation during the ventricular vulnerable refractory period18, a phenomenon also observed in our ultrasonic experiments as illustrated in Figure 3.10B. Before stimulation, sinus rhythm was around 85 bpm. Ultrasonic stimulation induced a ventricular tachycardia up to 165 bpm (2nd trace from the top in Figure 3.10B) with atrio-ventricular dissociation (top trace in Figure 3.10B) resulting in impairment of hemodynamics (3rd trace from top in Figure 3.10B). Consecutive stimulations of the RA and the RV with the desired delay can be achieved using a single

ultrasonic emitter (example in Figure 3.10C), exploiting the beam steering capability of our phased-array ultrasound transducer. The yellow HIFU pulse was targeted in the RA while the red HIFU pulse was targeted in the RV. The interpulse delay was set to 0 ms, 40 ms and 120 ms (from top to bottom in Figure 3.10C), demonstrating the ability to

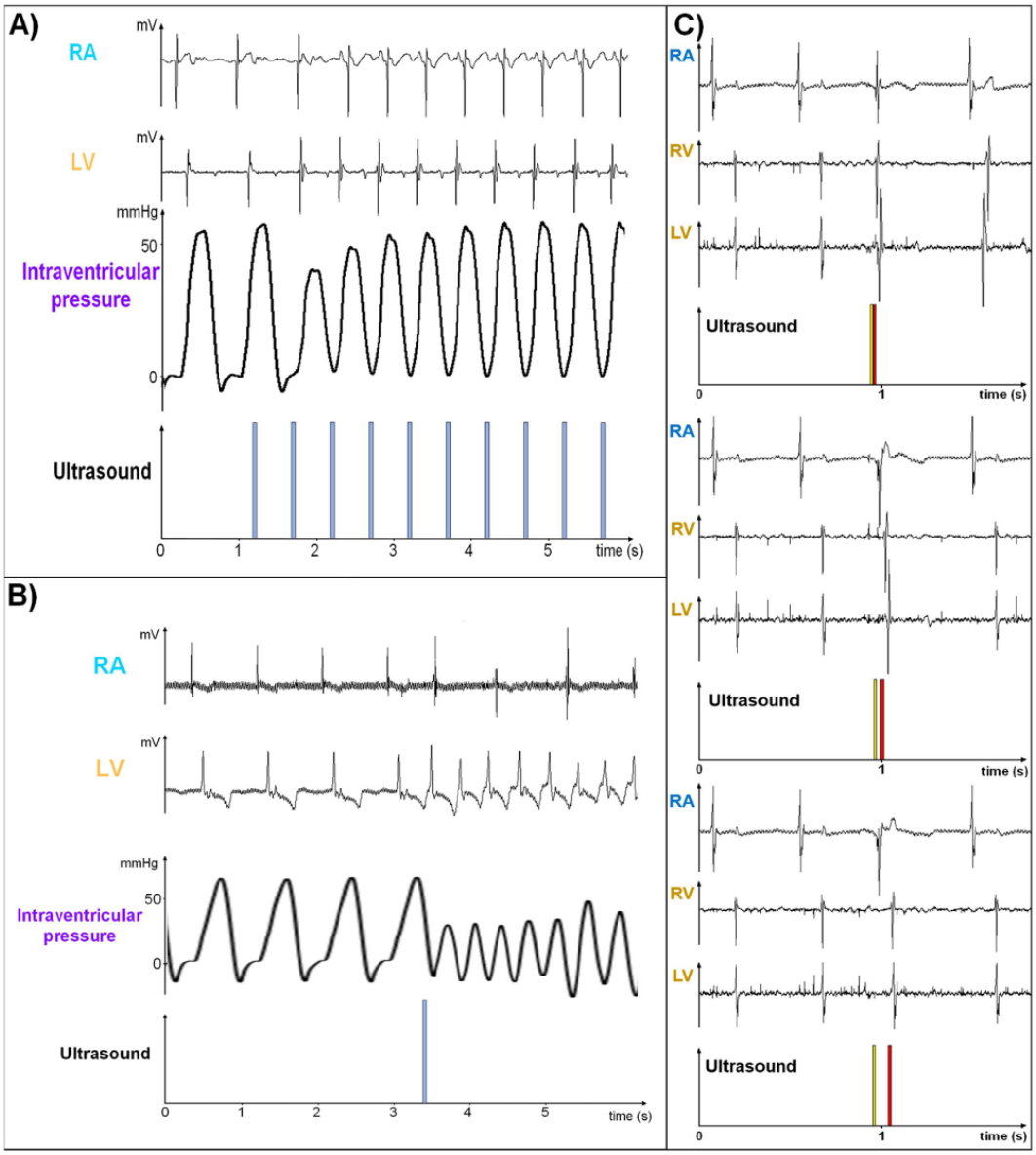

Figure 3.10: Displacement monitoring during focus steering(A) Electrical and hemodynamic recordings of continuous ultrasonic pacing of the heart at 120 bpm (sinus rhythm: 100 bpm). (B) Electrical and hemodynamic recordings of ultrasound-induced ventricular tachycardia (165 bpm, sinus rhythm 85 bpm) after triggering the acoustic pulse during the relative refractory period. (C) Example of atrioventricular stimulation with a single ultrasonic probe. Phased array transducer enables consecutive stimulation of the RA (yellow pulse) and the RV (red pulse) with a programmed delay (from top to bottom: 0 ms, 40 ms and 120 ms interpulse delay, respectively).

3.3.2 Feasibility of cardiac MR-ARFI monitoring

ARFI displacement has been monitored successfully in the heart. As expected, when the sequence was triggered during the refractory period (yellow box on Figure 3.11) no premature heart contraction was observed, neither on the LV electrophysiology nor in LV pressure recordings. ARFI displacement confirmed that the shot was performed in the myocardium and a maximal displacement of 28 μm was observed (Figure 3.11B). With the same acoustic pressure and the sequence triggered in the non-refractory period of the heart, an extra systole was observed on both LV electric and pressure signals (see green arrow on Figure 3.11). ARFI displacement confirmed that the shot was performed in the myocardium and a maximal displacement of 41 μm was measured.

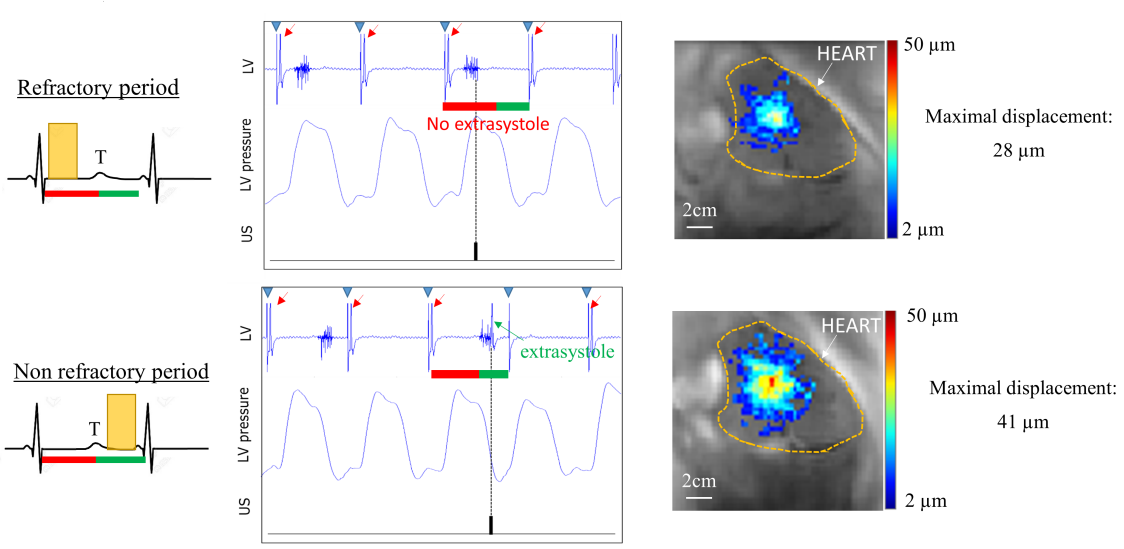

Figure 3.11: Monitoring of displacement during cardiac stimulation A shows electrical and pressure recording of the LV. Gradient artifact of the MR-acquisition can be seen on the electrical signal (see black arrow). The heart is paced (blue triangles) and ventricular response is visible on both electrical and pressure signal (red arrow).B shows displacement maps.

Figure 3.12 shows the ARFI displacement curve in blue and the LV pressure in red along a cardiac cycle. When the heart is contracting, the slope of the pressure curve is positive and a lower displacement amplitude was observed. During the resting state of the cardiac cycle, the displacement was found constant around 20 μm.

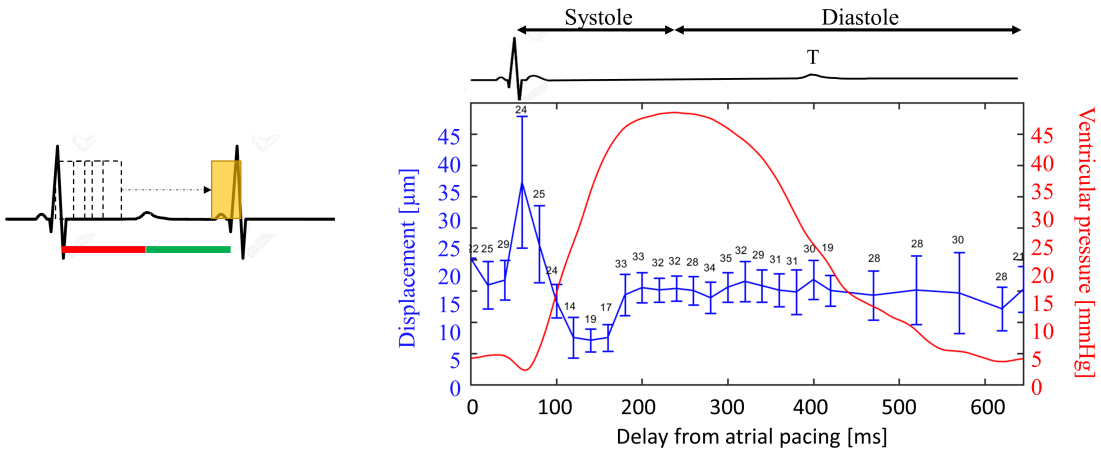

Figure 3.12: Monitoring of displacement along the cardiac cycle Displacement variations for successive increment of the trigger delay from the R wave detection.

Figure 3.13 shows successive phase images during cardiac stimulation using electronic steering on a Langendorff heart. For the four shot locations (stimulation attempts), the phase increased due to the displacement encoding. These positions were in agreement with the planning step (see localization image on Figure 3.13).

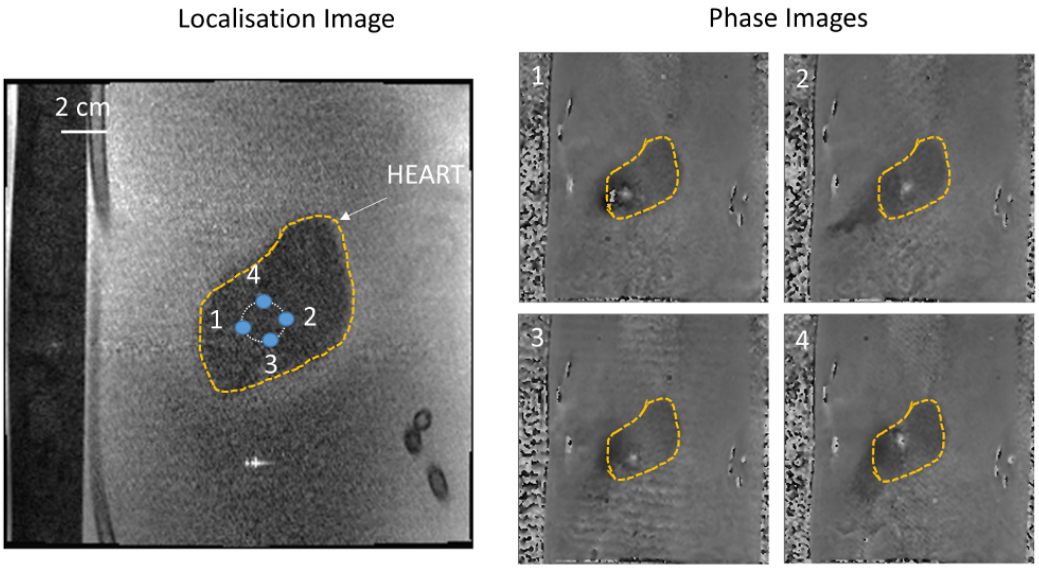

Figure 3.13: Displacement monitoring during electronic steering Localization image with the spatial position of the four stimulation attempts, labelled 1 2 3 4. Yellow dashed line represents the heart segmentation. Phase images display the displacement encoding for the 4 successive shots.

3.3.3 In vivo proof of feasibility of HIFU stimulation

The minimal stimulation threshold of 4 MPa negative pressure at the focus (as determined from ex vivo experiments) could not be reached with our current in vivo setup. The maximal peak negative pressure was estimated to be around 2 MPa in situ, due to the limited acoustic window (see Materials and Methods section). At this pressure level,

stimulation of the LV was observed but with an insufficient success rate. To overcome this limitation and demonstrate in vivo feasibility, ultrasound contrast agents were injected intravenously to enhance HIFU mechanical effects on tissue, hence decreasing the stimulation threshold. Figure 4 shows examples of in vivo data. Complete electrical recordings in both the RA and the LV using the same MR-compatible catheters as well as surface ECG were available. Using this protocol, consistent cardiac stimulation was achievable for up to 1 hour sessions in 4 different animals.

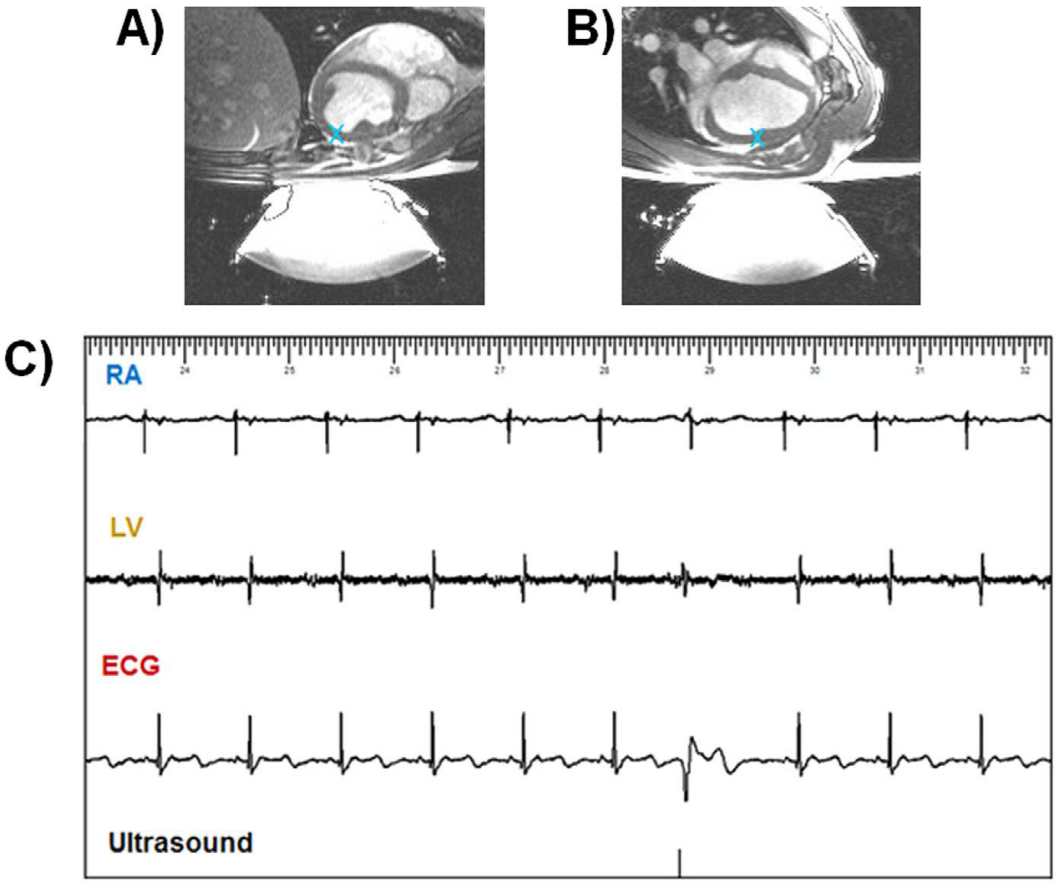

Figure 3.14: In vivo proof of concept of non-invasive cardiac stimulation. (A,B) Sagittal and transverse MR-images of the anesthetized pig (blue cross depicts targeted region). Using our current setup, adjunction of ultrasound contrast agent was necessary to consistently induce PVCs in vivo. (C) shows an example of such stimulation in the second animal with complete electrical recordings in both RA and LV as well as surface ECG. The acoustic pulse induced a premature ventricular depolarization observed as a premature QRS complex on the ECG with a different morphology as compared to the conducted QRS.

For the last two animals, a preliminary investigation of the effects of ultrasound contrast agent concentration on stimulation threshold was performed. The lowest HIFU pressure to induce cardiac depolarization was determined using a pulse duration of 5 ms. 5 peak negative pressure steps were defined for animal #3 (0.6, 0.8, 1.0, 1.4 and 1.9 MPa after taking the total attenuation into account) and 4 for animal #4 (0.55, 0.75, 1.1 and 1.6 MPa after taking total attenuation into account). The results are depicted in Figure

3.15A. Differences in in situ pressure levels can be explained by slightly different animal orientation and anatomy leaving a different surface of the acoustic beam intercepted by the ribs and the lungs. A preliminary comparison of short and long pulses (100 μ s and 5 ms) was also performed on the last animal. Three different pressure levels were applied across time to check whether pulse duration had an effect on ultrasonic stimulation. Results are shown in Figure 3.15B. As opposed to the ex vivo case without adjunction of ultrasonic contrast agents, the pulse duration did not have any effect on the stimulation threshold in the presence of microbubbles.

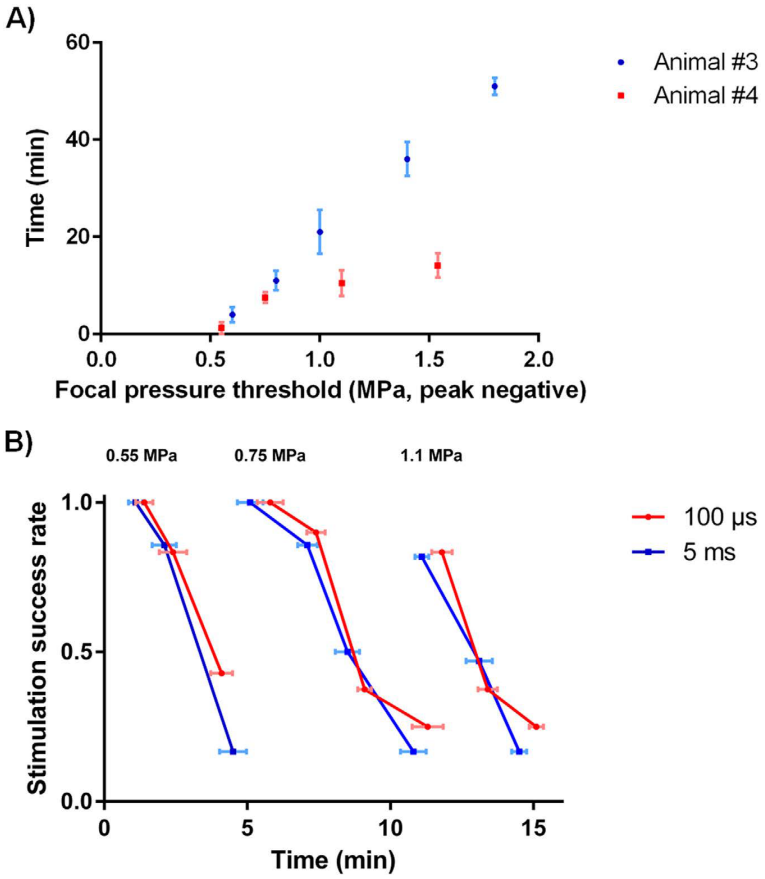

Figure 3.15: (A) Time when it was necessary to increase the acoustic amplitude to induce consistent cardiac depolarization as a function of the peak negative pressure in situ due to ultrasound contrast agent clearance. (B) Evolution of the stimulation success rate according to time of application for short and long pulses (100 μ s and 5 ms respectively) at different pressure levels (0.55 MPa, 0.75 MPa and 1.1 MPa peak negative).

3.3.4 Passive cavitation detection

Results for 2 out of 240 remote stimulations in vivo with the adjunction of contrast agent (SonoVue, Bracco, Italy) can be seen in Figure 3.16D and F (0.7 MPa and 1.3 MPa peak negative). Because of the screening effect of the rig cage and lungs, the stimulation threshold could not be reached with the equipment used (maximum estimated

focal pressure: 1.8 MPa peak negative). Two consecutive 0.1 $mL.kg^{1}$ boli intravenous injections were performed in each animal based on the contrast agent half-life time (mean 12 min, ranging from 2 min to 33 min). The same protocol was followed regarding treatment planning, targeting the left ventricle (see Figure 3.16D), electrograms and intraventricular pressure recordings. Figures 3.16E and 3.16F show those local electrograms, ultrasound trigger output and intraventricular pressure resulting from the two different pressure levels. Because of the ultrasound contrast agent pharmacokinetic, the stimulation threshold decreases along time as highlighted by Figure 3.15. All the in vivo PCD measurements were performed few minutes after the microbubbles injection when the stimulation threshold was around 0.6 MPa. Figures 3.16B and 3.16C show local electrograms, ultrasound trigger output and intraventricular pressure resulting from the two different pressure levels. The two displayed cases were therefore performed at threshold and at two-fold threshold respectively.

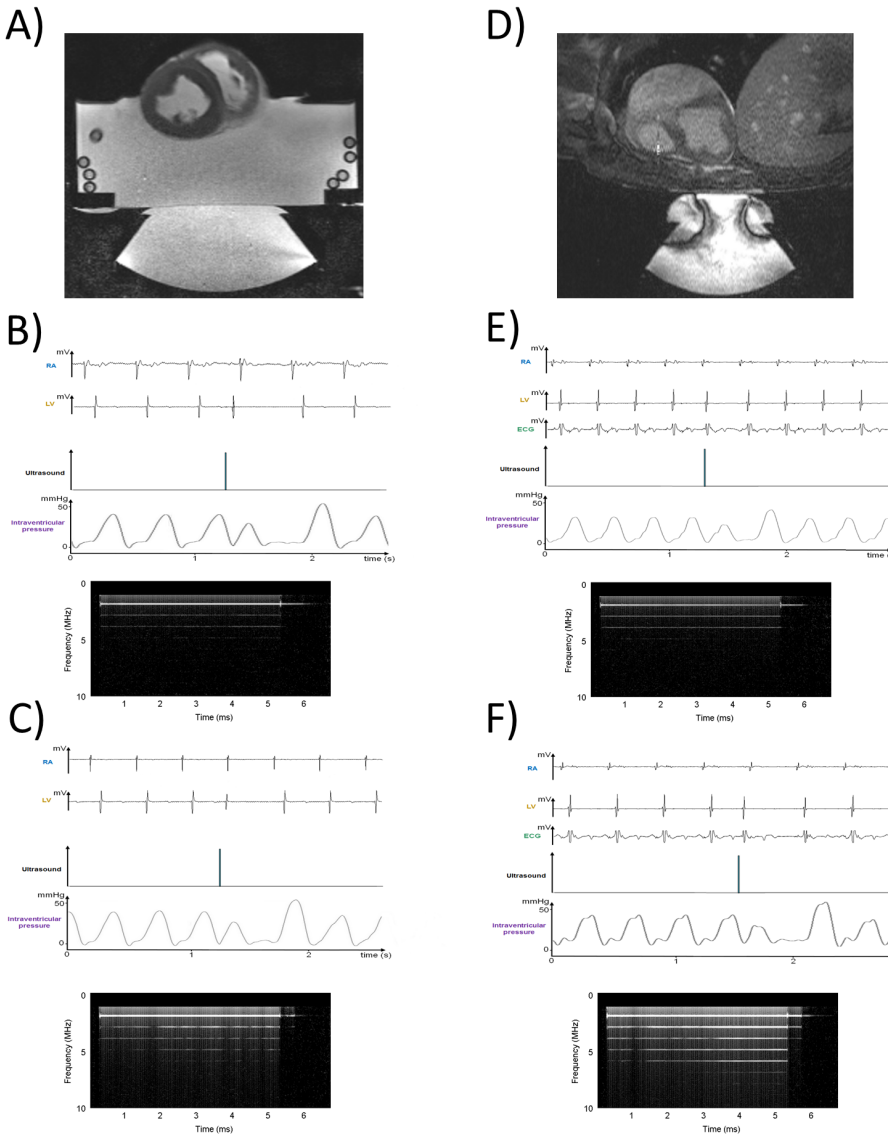

Figure 3.16: Cardiac stimulation monitored by PCD. Transverse MR image of the ex vivo beating pig heart, blue cross depicts targeted region (A). Examples of recordings acquired during non-invasive cardiac pacing at stimulation threshold (B) and at two-fold threshold (C). These recordings include electrocardiograms for RA and LV, focus ultrasound signal, left intraventricular pressure and PCD spectrograms (fundamental removed). Sagittal MR image of the anesthetized pig, blue cross depicts targeted region (D). Examples of recordings acquired during non-invasive cardiac pacing at stimulation threshold (E) and at two-fold threshold (F). These recordings include electrocardiograms for RA and LV, surface ECG, focus ultrasound signal, left intraventricular pressure and PCD spectrograms (fundamental removed).

For all the applied pressures, the stable and inertial were computed and an unpaired two-tailed Student's t-test was used to determine if measured SCD and ICD were significantly higher ($p < 0.05$) than the noise for each pressure. The combined results of SCD and ICD for both ex vivo and in vivo can be seen in Figure 3.18. During the ex vivo experiments, stable cavitation was found significant for peak negative pressures above 1.1 MPa while inertial cavitation was found significant for peak negative pressures above 2.2 MPa. During the in vivo experiments using ultrasound contrast agents, stable cavitation

was found significant for peak negative pressures above 0.2 MPa while inertial cavitation was found to be significant for peak negative pressures above 0.7 MPa. Figure 3.18 sums up all the cases displaying the ratio of computed doses over noise. The specific stimulation thresholds were added in green dotted line (0.6 MPa) for the in vivo cases with ultrasound contrast agents and in red dotted line (4 MPa) for the ex vivo cases.

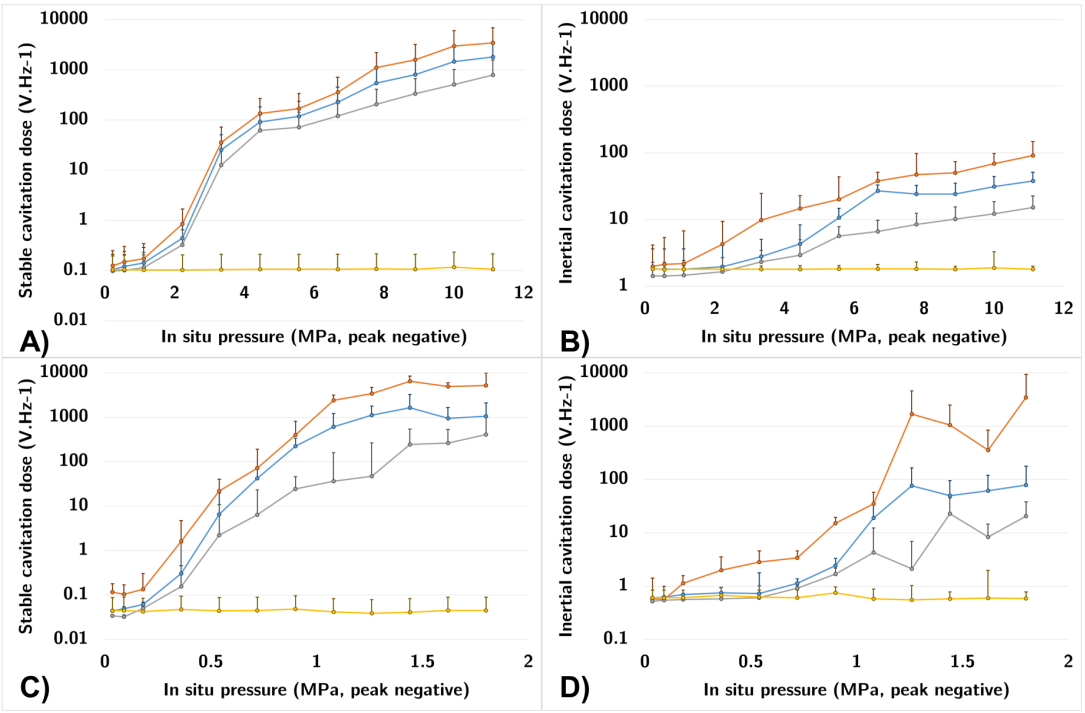

Figure 3.17: Cavitation metrics. Cavitation metrics (doses, min and max as well as noise levels) as a function of the in situ pressure measured during all experiments. Graphs depict stable cavitation (A) and inertial cavitation metrics (B) for the ex vivo cases as well as stable cavitation (C) and inertial cavitation metrics (D) for the in vivo cases with adjunction of ultrasound contrast agent.

For the ex vivo cases, SCD dramatically increases near threshold (SCD ratio over noise from 241.1 to 856.0 while increasing the pressure from 3.5 MPa to 4.4 MPa peak negative). The same pattern occurs for the in vivo cases with microbubbles (SCD ratio over noise from 149.6 to 946.9 while increasing the pressure from 0.5 MPa to 0.7 MPa). Moreover both ex vivo SCD and in vivo SCD are of the same order of magnitude near threshold. SCDmax and SCDmin values are consistent with SCD for all the pressure range. Regarding inertial cavitation, its dose is marginal near threshold for both ex vivo and in vivo cases (ICD ratio over noise of 2.4 at 4.4 MPa peak negative and of 1.9 at 0.7 MPa peak negative respectively). Increasing the pressure further will dramatically increase the ICD both ex vivo (ratio over noise of 14.8 at 6.6 MPa) and in vivo (ratio over noise of 138.1 at 1.1 MPa).

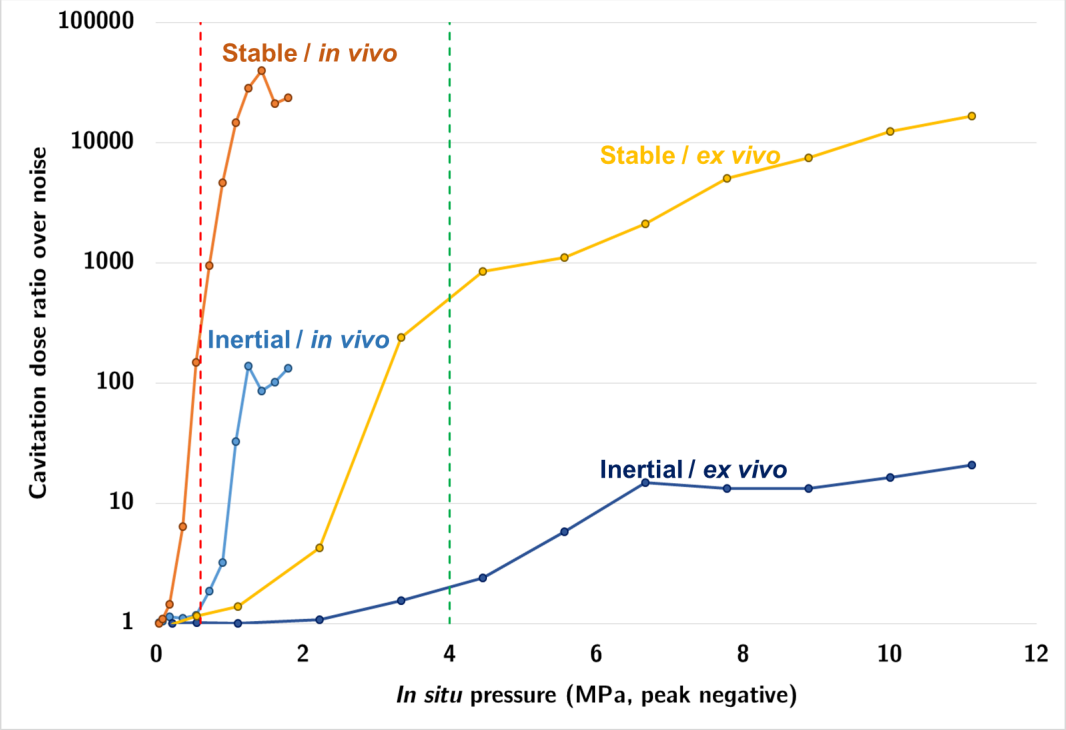

Figure 3.18: Passive cavitation tresholds for sucessfull stimulation. Ratio of stable and inertial cavitation doses over noise as a function of the in situ pressure. The green dashed line represent the stimulation threshold (0.6 MPa peak negative) with the adjunction of microbubbles during the time period of PCD data acquisition. The red dashed line represents the stimulation threshold (4 MPa peak negative) without the adjunction of ultrasound contrast agent for the pulse length (5 ms) used in this study.

3.3.5 Preliminary safety assessment

Preliminary safety assessment was performed for all the 10 ex vivo and 4 in vivo cases. Figure 3.19 shows examples of safety assessment for one of the four in vivo cases. No damage was observed in inversion-recovery MR-sequences performed in vivo in the 4 animals (Figure 3.19A). No signal increase can be seen in the myocardium in the delayed-enhancement MR images that would indicate irreversible injury. Gross pathology (Figure 3.19B) and Masson's staining (Figure 3.19C) revealed no differences between stimulated and control regions, for all the cases for which samples were collected (4 ex vivo and 4 in vivo). No evidence of coagulative necrosis, hemorrhage or interstitial edema was found in the samples. For the in vivo cases, no damage was noted at visual inspection on the skin, esophagus, lungs and rib cage. Therefore, no further histological analysis was conducted on these organs.

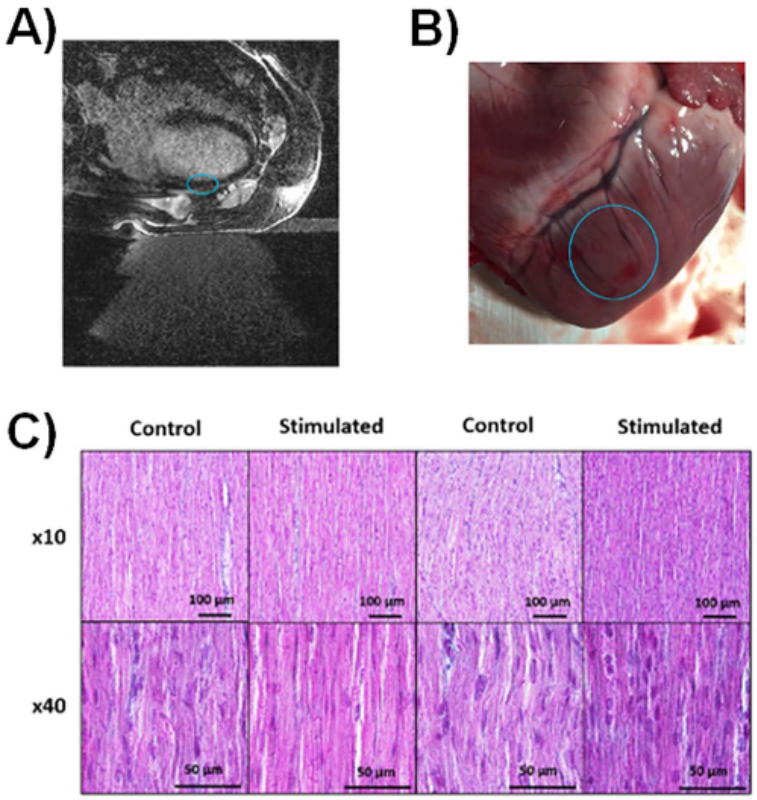

Figure 3.19: Examples of safety reports from the 4 in vivo cases.(A) 3D Inversion-recovery MR sequences did not reveal any contrast agent enhancement in the myocardium meaning that no scar or edema were detectable (blue circle depicts sonicated region). (B) Gross examination did not reveal any particular damage in the sonicated region of any animal (blue circle depicts sonicated region). (C) Histology (Masson's staining) slices analysis did not show noticeable differences between control and sonicated regions.

3.4 Discussion

The need for a less intrusive approach has been highlighted with the recent development of leadless pacing [13, 14, 15] This promising technique offers improvements in both reduction of invasiveness and improved cost-effectiveness at the expense of implant risks due to large diameter device (perforation) and issues with replacement and retrieval of the device (dislodgement). However this approach remains mini-invasive. To the best of our knowledge, this study is the first ex vivo and in vivo proof of feasibility of controlled non-invasive ultrasound-based threshold as a function of ultrasound pulse duration and amplitude. The in vivo proof of feasibility performed in large animals showed that this novel technology offers good prospects for clinical developments.

Pressure values needed to depolarize the myocardium were in the same range as those reported in small animals [16, 17]. The shape of the stimulation threshold curve for the acoustic stimulation at 1 MHz displays two well identified pressure thresholds for pulse durations shorter or longer than 1 ms. This suggests the existence of two distinct mechanical stimulation mechanisms, e.g. cavitation radiation force or another process.

Cavitation has already been suggested as one of the driving mechanisms in small animal studies, as adjunction of ultrasound contrast agents decreased the stimulation threshold. Our study supported these findings. Acoustic backscattered signals from the focus have been recorded during both ex vivo and in vivo experiments. Ex vivo and transcostal in vivo cavitation detection during non-invasive cardiac pacing was shown feasible in this study. SCD and ICD were measured ex vivo and in vivo in 14 pigs. SCD increased near stimulation threshold and its value is consistent from ex vivo to in vivo experiments suggesting the idea that a minimal dose might be needed to induce cardiac depolarization. Ongoing studies are needed to correlate SCD with stimulation success rate but this metric is a promising candidate for treatment efficacy monitoring. Inertial cavitation was maintained minimal near threshold ex vivo and was not significant near threshold in vivo. As of now, results from this study show that acute stimulation during hour-long sessions did not cause any detectable damage near threshold. Further investigations are needed to determine the correlation between low ICD and safe stimulation as well as between high ICD and induced damages. Those metrics have already been linked to treatment efficacy and safety for the disruption of the blood-brain barrier using focused ultrasound [18, 19] but its cardiac application need further validations.

Feasibility of MR-ARFI displacement monitoring on the heart was performed successfully. Monitoring of the displacement has several interests:

1. Localize the focus position within the heart. This can for instance avoid false negative, when sonication is performed outside the myocardium or be used during focus steering to see successive stimulation sites.

2. Characterize in a qualitative way the cardiac tissue stiffness and especially its variation during cardiac contraction. For instance, Pernot et al. [20] characterized cardiac tissue elasticity variation, using ultrasound shear wave imaging.

3. Characterization of nonlinear effects at the focus due to inertial cavitation by monitoring displacement profile and amplitude variations along time.

Even though this method allowed to monitor the displacement induced at the focus or follow the displacement variations along the cardiac contraction, the acoustic power needed to have a sufficient signal to noise on displacement images, were $\sim$2-fold greater than the cardiac stimulation threshold. Complementary experiments should be performed to attest the safety of the monitoring. However its application for cardiac ablations in combination with temperature monitoring (Chapter 2) remains promising.

In the presence of an ultrasound contrast agent, no differences in minimal pressure to induce cardiac depolarization were found in vivo between short and long pulses (100 μs and 5 ms) suggesting that cavitation may be the preferred mechanism under these experimental conditions. Long lasting stimulation was possible ex vivo however in its current configuration the transducer design is suboptimal for this application in vivo and was unable to generate sufficient focal pressure due to attenuation of ultrasonic waves by the rib cage. As such, consistent cardiac depolarization could not be achieved without the adjunction of ultrasound contrast agents. The aperture of the ultrasound probe has to be adapted to the small acoustic window due to the presence of ribs or lungs and both respiratory and cardiac motions have to be taken into account. Real-time target tracking and adaptive beam-steering might improve the efficacy of non-invasive cardiac stimulation without the adjunction of ultrasound contrast agent. This requires further development of dedicated hardware and software to perform efficient non-invasive cardiac pacing in vivo without the adjunction of ultrasound contrast agent.

In vivo and ex vivo imaging and histology preliminary safety studies did not show any differences between sonicated and control tissues. These encouraging results show that acute stimulation during hour-long sessions did not cause any detectable thermal and mechanical damage under the experimental parameters used. Ongoing work includes a complete safety study in vivo using various stimulation protocols. This investigation coupled with the aforementioned real-time cavitation monitoring study is crucial to judge the clinical potential of this technique. This is motivated by reports of macroscopic lesions using ultrasound contrast agent and focused ultrasound targeting thVarious ultrasound-induced electrical effectse myocardium in rats under extreme exposure conditions (respectively 15.9 MPa and up to 8 MPa in situ peak negative pressure, both using ultrasound contrast agent). Eventually a complete preclinical chronic safety investigation will be performed. Such a study could be performed collecting blood samples during non-invasive stimulation sessions and biomarkers of cardiac injury such as myoglobin, lactate dehydrogenase,creatine kinase and troponin could be looked for. These biomarkers have been proven to correlate well with cardiac injury in different large animal models [21, 22].

The present study also shows a number of limitations. The success rate threshold for stimulation was arbitrarily set to 90% to account for the few occurrences of false negatives (see Figure 3.8B). Although arbitrary, the resulting pressure thresholds for short and long pulses are relevant as modification of this threshold will not result in drastic changes in the minimal pressure needed to induce a cardiac depolarization. These false negatives

might be caused by the experimental conditions. Firstly, swinging motion of the ex vivo heart on the polyurethane membrane might have occurred during its contraction. Also, the heart was not paced and was beating in sinus rhythm. Therefore when stimulating different regions of the ventricles, some sonications could have occurred during the absolute refractory period. Ex vivo assessment of the ultrasound contrast effect on the stimulation threshold was complicated due to the Langendorff perfusion (comprising pump and oxygenator that would not allow microbubbles to be stable for a sufficient time). However this study demonstrates the potential of such an ultrasound-based non-invasive cardiac stimulation in large animals that may provide a new approach to regulate cardiac function. Last but not least, MRI was used during this study as the main imaging modality for targeting, planning and safety assessment. Other simpler imaging modalities could be used such as ultrasound imaging for real-time HIFU guidance. This other imaging modality might also be used for hemodynamic assessment and coupled with extracorporeal ECG for a fully non-invasive procedure.

3.5 Conclusion

In this study we have presented a purely extracorporeal approach to perform contactless cardiac stimulation using High Intensity Focused Ultrasound (HIFU). Several applications have been identified (long duration pacing, multi-site pacing, induction of arrhythmia) and two monitoring methods (PCD and MR-ARFI) have been validated.

3.6 Perspectives

In perspective of in vivo cardiac stimulation without adjunction of ultrasound contrast agent, further developments will be needed. These developments will focus on: optimization of the acoustic window to avoid ribs/lung screening of the ultrasound beam, the choice of the operating frequency of the transducer and finally the optimization of the ultrasound energy distribution.

3.6.1 Acoustic windows optimization

In this study, we have used a large 256 elements transducer with an aperture of 14.5 cm. This large aperture intercepted several ribs and sometimes lungs, reducing the resulting acoustic power at the focus. In order to optimize the ultrasound propagation, intercostal

sonication approach should be preferred. Indeed, a transducer with a 2-3 cm size in the elevation direction might allow to deposit most part of the energy on the heart. It requires the design of a dedicated multi-element HIFU probe whose design may be similar to those used for ultrasound imaging. This design would allow to target the heart from different locations (see Figure 3.20).

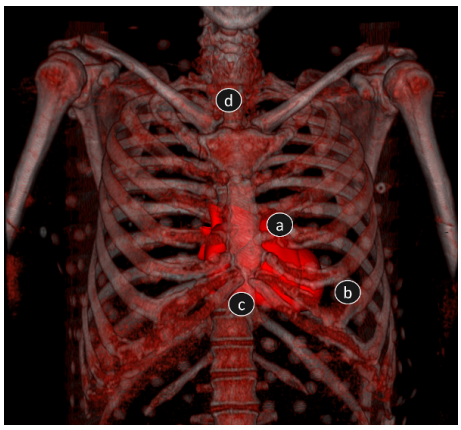

Figure 3.20: Thoracic cage and registration of the heart position.The most common echo windows are: (a) the left parasternal window, (b) the apical window, (c) the subcostal window, and (d) the suprasternal notch.

3.6.2 Choice of ultrasound operating frequency

The choice of the transducer operating frequency may be important as cavitation effects seem to be the predominant actor in the cardiac depolarization. As described in section 2.2.6.1, cavitation effects can be enhanced by decreasing the emission frequency. Hence, the stimulation threshold in terms of acoustic pressures may be decreased using lower frequencies. The role of the emission frequency in transcient applications of ultrasounds is an ongoing field of research for other applications. For instance, a multi-frequency transducer was designed for investigating ultrasound frequency effects in neurostimulation [23]. Even though a lower frequency enhance the cavitation effects, it also decreased focalization capacity of the transducer. This will result in a larger focus size and lower acoustic power for a given acoustic power at the surface of the transducer. In addition, steering capability will be also reduced. Hence, a compromise must be made between focalization capacity and generation of cavitation effects.

Exploratory experiments were performed using two 8 channel transducers operating at 2.5 MHz and a 1.5 MHz with a focal distance of 2 cm, respectively. Acoustic power and focus size were investigated. During these experiments, the pig chests were opened and we tentatively performed cardiac stimulations in direct contact with the heart. Sonication were performed at more than two-fold the cardiac stimulation threshold found in

this study. There preliminary results have highlighted the importance of the frequency source, as with the 2.5 MHz transducer, not a single stimulation could be induced even at maximum acoustic power. On the contrary, with the 1.5 MHz transducer, several stimulations were performed, but with lower success rate than at 1 MHz with the 256 elements transducer. In light of this exploratory result, further studies should be conducted to investigate the relationship between cardiac stimulation success rate and the ultrasound operating frequency. At the end of this writing, two prototypes are being built to test this hypothesis and refine specifications to create a product that could be clinically relevant.

3.6.3 Sonication patterns optimization

As of now, consecutive pacing reported in Figure 3.10 were limited to a single focus position. The repeated sonication at the same location may destroy bubble and hence, decrease the cavitation effect and success rate of cardiac stimulation.

Additional exploratory experiments have been conducted on isolated left ventricles (N=2) of pigs with more complex sonication patterns. These sonication patterns aim at distributing the ultrasound energy on a larger surface of the heart using the beam steering capability of our transducer. Using a distributed energy deposition, the stimulation success rate seems to be improved, but this assessment has to be supported by additional experiments.

3.7 References

[1] E. Newton Harvey. “THE EFFECT OF HIGH FREQUENCY SOUND WAVES ON HEART MUSCLE AND OTHER IRRITABLE TISSUES”. In: *American Journal of Physiology – Legacy Content* (1929).

[2] Diane Dalecki et al. “Effects of pulsed ultrasound on the frog heart: I. Thresholds for changes in cardiac rhythm and aortic pressure”. In: *Ultrasound in medicine & biology* (1993).

[3] Amit Livneh et al. “Extracorporeal acute cardiac pacing by High Intensity Focused Ultrasound”. en. In: *Progress in Biophysics and Molecular Biology* (Aug. 2014).

[4] Truong An Tran et al. “On the Mechanisms of Ultrasound Contrast Agents-Induced Arrhythmias”. en. In: *Ultrasound in Medicine & Biology* (June 2009).

[5] M. Delius et al. “Biological effects of shock waves: induction of arrhythmia in piglet hearts”. In: *Ultrasound in medicine & biology* (1994).

[6] Andrew R. Kohut et al. “The potential of ultrasound in cardiac pacing and rhythm modulation”. en. In: *Expert Review of Medical Devices* (Sept. 2016).

[7] Aya Miwa and Nobuki Kudo. “Study on effects of pressure and duration of ultrasound pulse on pulsation of cultured cardiomyocytes”. In: *Ultrasonics Symposium (IUS), 2016 IEEE International*. IEEE, 2016.

[8] E. E. van der Wall. “Cardiac resynchronisation improves survival in mild heart failure!” en. In: *Netherlands Heart Journal* (Mar. 2011).

[9] T Alexander Quinn and Peter Kohl. “Comparing maximum rate and sustainability of pacing by mechanical vs. electrical stimulation in the Langendorff-perfused rabbit heart”. In: *Europace* (2016).

[10] Fanny Vaillant et al. “Magnetic resonance-compatible model of isolated working heart from large animal for multimodal assessment of cardiac function, electrophysiology, and metabolism”. en. In: *American Journal of Physiology - Heart and Circulatory Physiology* (May 2016).

[11] Daniel Pereda et al. “Elective cardiac surgery using Celsior or St. Thomas No. 2 solution: a prospective, single-center, randomized pilot study.” In: *European journal of cardio-thoracic surgery : official journal of the European Association for Cardio-thoracic Surgery* (2007).

[12] Mark G. Hoogendijk et al. “Ventricular fibrillation hampers the restoration of creatine-phosphate levels during simulated cardiopulmonary resuscitations”. In: *Europace* (2012).

[13] A. Auricchio et al. “First-in-man implantation of leadless ultrasound-based cardiac stimulation pacing system: novel endocardial left ventricular resynchronization therapy in heart failure patients”. en. In: *Europace* (Aug. 2013).

[14] Vivek Y. Reddy et al. “Percutaneous Implantation of an Entirely Intracardiac Leadless Pacemaker”. en. In: *New England Journal of Medicine* (Sept. 2015).

[15] P. Ritter et al. “Early performance of a miniaturized leadless cardiac pacemaker: the Micra Transcatheter Pacing Study”. In: *European Heart Journal* (2015).

[16] Diane Dalecki et al. “Effects of pulsed ultrasound on the frog heart: II. An investigation of heating as a potential mechanism”. In: *Ultrasound in Medicine & Biology* (1993).

[17] A. G. MacRobbie et al. “Thresholds for premature contractions in murine hearts exposed to pulsed ultrasound”. eng. In: *Ultrasound in Medicine & Biology* (1997).

[18] Fabrice Marquet et al. “Real-Time, Transcranial Monitoring of Safe Blood-Brain Barrier Opening in Non-Human Primates”. en. In: *PLoS ONE* (Feb. 2014). Ed. by Stefan Liebner.

[19] Shih-Ying Wu et al. “Transcranial cavitation detection in primates during blood-brain barrier opening-a performance assessment study”. In: *IEEE Transactions on Ultrasonics, Ferroelectrics, and Frequency Control* (June 2014).

[20] Mathieu Pernot et al. “Real-Time Assessment of Myocardial Contractility Using Shear Wave Imaging”. In: *Journal of the American College of Cardiology* (2011).

[21] P J O’Brien et al. “Cardiac troponin I is a sensitive, specific biomarker of cardiac injury in laboratory animals.” In: *Laboratory animals* (2006).

[22] Yue Jin Feng et al. “Comparison of cardiac troponin I, creatine kinase-MB, and myoglobin for detection of acute ischemic myocardial injury in a swine model”. In: *American Journal of Clinical Pathology* (1998).

[23] Charlotte Constans et al. “A 200–1380-kHz Quadrifrequency Focused Ultrasound Transducer for Neurostimulation in Rodents and Primates: Transcranial In Vitro Calibration and Numerical Study of the Influence of Skull Cavity”. In: *IEEE Transactions on Ultrasonics, Ferroelectrics, and Frequency Control* (Apr. 2017).

CHAPTER 4

Simultaneous monitoring of temperature and displacement under MRI

Contents

4.1 Introduction

This chapter presents an ablation monitoring method that measures at the same time the temperature increase and the focal displacement induced by the acoustic radiation force. We will explore the added value of displacement monitoring along with conventional MR-Thermometry. In the previous Chapter, we have performed the first proof of feasibility of MR-ARFI monitoring on the heart, during cardiac stimulation. Besides ablation applications, monitoring both the temperature and the displacement would allow to attest if a temperature increase is generated during cardiac stimulation and could attest the safety of the procedure

Personal contributions:

- Sequence development and real-time computation of temperature and displacement images.
- Management of all ex vivo andin vivo animal experimentations.
- Data post-treatment and production of figures.

4.1.1 Literature

Magnetic Resonance-guided High Intensity Focused Ultrasound (MRgHIFU) allows for non-invasive ablation of pathological tissue. Current clinical procedures exploit MR images for target delimitation, online thermometry to define a therapy end-point during the ablation, and post-ablation lesion assessment [1, 2]. Typically, the principal monitoring parameters are temperature measurement via the Proton Resonance Frequency Shift (PRFS) [3] along with online thermal dose calculations [4]. During treatment, acoustic characteristics of tissue may change, such as absorption with temperature, tissue elasticity with protein denaturation [5] or, for example, in the presence of cavitation, shock wave [6] or boiling [7]. If small bubbles form within the HIFU propagation cone at the patient's body surface during sonication, less acoustic energy is transmitted to the target region, making treatment more difficult to achieve. However, local modifications of tissue characteristics can be exploited to enhance heating efficiency [8] at the focus and to protect tissues located beyond the targeted area [9]. Specifically, online rapid monitoring

of potential transient changes of tissue acoustic properties during HIFU sonication simultaneously with temperature imaging, may help to improve the safety of the procedure, exploit non-linear effects (e.g. cavitation) of ultrasound for enhanced heating efficiency and provide additional information on the outcome of the therapy beside conventional thermal dose imaging. The imaging sequence should be fast, allow large spatial coverage and provide a high sonication duty cycle to avoid a loss in heating efficiency. MR-Acoustic Radiation Force Impulse (ARFI) imaging encodes the local displacement of soft tissues induced at the HIFU focal point in the phase image (using a Motion-sensitive Encoding Gradient, MEG) synchronized with short duration ultrasound pulses [10, 11]. MR-ARFI has been reported to visualize the focal spot location prior to ablation without inducing thermal effects, to compensate tissue aberrations relative to ultrasound propagation in transcranial HIFU ablation [12, 13] and to determine the acoustic pressure for exploiting nonlinear effects of HIFU in order to enhance heating efficiency [7]. MR-thermometry and MR-ARFI imaging are complementary as they are respectively sensitive to thermal and mechanical effects. For example, during ultrasonic neuromodulation, nerve conduction blocking has been attributed to a thermal action of ultrasound by some teams [14] whereas other teams attributed it to action of radiation pressure [15] or intramembrane cavitation [16]. Therefore, simultaneous imaging of both temperature and displacement would help to better understand the mechanisms underlying this bioeffect for a given experimental situation. In the present work, we propose a fast implementation of a simultaneous MR-ARFI-thermometry allowing subsecond multi-slice imaging of temperature and displacement during HIFU ablation. An MR-ARFI-thermometry sequence has already been proposed [17, 18] to visualize focal spot location and to verify the absence of thermal effect prior to ablation. However, its current implementation has a limited sonication duty cycle to induce thermal necrosis and remains too slow to monitor HIFU ablation.

4.1.2 Objectives

In this study, we propose a continuous monitoring of temperature and displacement during a HIFU treatment where we preserved a high sonication duty cycle (> 80 %) compatible with thermal ablation energy deposition. Additional data reflecting tissue elasticity modifications associated with temperature changes were extracted from displacement measurements. The method was first evaluated in ex vivo skeletal muscle to demonstrate the benefit and limitations of the technique. Then, in vivo sonications were

performed in the liver of pigs to illustrate potential of rapid and simultaneous temperature and displacement monitoring during ablation in a clinically relevant application. Finally, in the perspective of a brain application, a proof of feasibility on two healthy volunteers was conducted to assess the stability of temperature and displacement measurements.

4.2 Materials and methods

4.2.1 Theory on temperature and displacement monitoring

Displacement (D) and temperature (T) were encoded into the phase image. Therefore, a second order finite development of the phase ϕ led to the following equation:

$$\phi = \phi_{ref} + \alpha_T.T + \alpha_D.D + \alpha_T.T^2 + \beta_D.D^2 + \theta.D.T \tag{4.1}$$

with $(\alpha_T, \alpha_D, \alpha_T, \alpha_D, \theta)$ constants and ϕ_{ref} a reference phase

Anterior works [3, 10] have shown that the phase variation induced by temperature or displacement taken independently was linear, thus β_T and β_D can be considered negligible in a first approach. In Eq 4.1, $\alpha_T = \gamma.TE.B0$ and $\alpha_D = \gamma.|A|.\Delta$ where $\gamma = 267.51$ rad.s^{-1}.T^{-1} was the gyromagnetic ratio, α= -0.0094 ppm.$^{\circ}C^{-1}$ [19] the PRFS constant, TE the echo time, $B_0 = 1.5$ T the static magnetic induction, Δ was the duration of the MEG, and A its amplitude.

Assuming that θ, the coefficient of second-order mixed partial derivatives of temperature and displacement, can be neglected, Eq 4.1 became:

$$\phi = \phi_{ref} + \alpha_T.T + \alpha_D.D \tag{4.2}$$

The sequence described in this manuscript uses an alternating MEG ($A = (-1)^i|A|$ where i is the dynamic acquisition number in the time series and $\alpha_D = (-1)^i.\gamma.|A|.\Delta$). Therefore, the average temperature $\overline{T}_i$ and displacement $\overline{D}_i$ i on two successive dynamic acquisition was computed by summing and subtracting two consecutive phase images:

$$(\phi^{i+} - \phi^{+}_{ref}) + (\phi^{(i-1)-} - \phi^{-}_{ref}) = \gamma.\alpha.TE.B0.(T_i + T_{i-1}) + (-1)^i.\gamma.|A|.\Delta(D_i - D_{i-1}) \tag{4.3}$$

$$(\phi^{i+} - \phi^{+}_{ref}) - (\phi^{(i-1)-}_{ref} - \phi^{-}_{ref}) = (-1).\gamma.|A|.\Delta.(D_i + D_{i-1}) + \gamma.\alpha.TE.B0.(T_i - T_{i-1}) \tag{4.4}$$

$$\overline{T}_i = \frac{T_i + T_{i-1}}{2} = \frac{(-1)^i.((\phi^{i+} - \phi^{+}_{ref}) + (\phi^{(i-1)-} - \phi^{-}_{ref}))}{2.\gamma.\alpha.TE.B0} - \epsilon_T \tag{4.5}$$

$$\overline{D}_i = \frac{D_i + D_{i-1}}{2} = \frac{(-1)^i.((\phi^{i+} - \phi^{+}_{ref}) - (\phi^{(i-1)-}_{ref} - \phi^{-}_{ref}))}{2.\gamma.|A|.\Delta} - \epsilon_D \tag{4.6}$$

From Eq 4.5 and 4.6, the errors in temperature (ϵ_T) and displacement (ϵ_D) were proportional to the temporal derivatives of displacement and temperature curves, respectively:

$$\epsilon_T = \frac{\alpha_D}{2.\alpha_T}(D_i - D_{i-1}) \tag{4.7}$$

and

$$\epsilon_D = \frac{\alpha_T}{2.\alpha_D}(T_i - T_{i-1}) \tag{4.8}$$

ϵ_T and ϵ_D led to artifact at the onset and offset of HIFU sonication where the temperature and displacement derivatives were maximum. Thermal dose was computed from temperature images using the Sapareto and Dewey [20, 21] algorithm with a threshold for the lethal thermal dose (LTD) of 240 min at 43 °C. For in vivo experiments, the rectal temperature measured by an optical probe served as the reference temperature for thermometry.

4.2.2 MR-sequence

A single-shot echo planar imaging (ss-GE-EPI) sequence was modified to insert a bipolar MEG before the echo train (Figure 4.2). The MEG direction was set parallel to the acoustic propagation axis to encode longitudinal tissue displacement induced by HIFU pulses, with adjustable duration (Δ) and amplitude (A, maximal value of 25 mT/m).

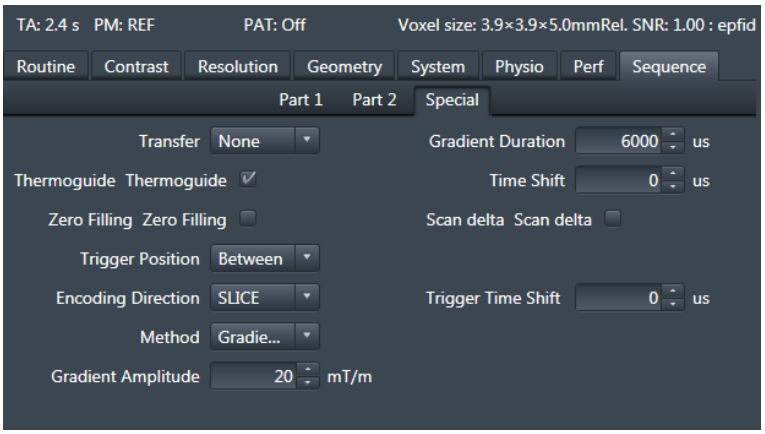

Figure 4.1: Sequence user interface: Here is a screen capture of the sequence that has been implemented. Note that all parameters were not required for this study.
Transfer: choose to reconstruct images on Siemens or with the Gadgetron
Thermoguide: activate the transfer from the Gadgetron to Thermoguide (visualization software);
Trigger Position: choose "when" to synchronize the ultrasound emission ["None" (no trigger), "Before" the MEG, "Between" the first and second lobe of MEG]
Encoding Direction: chose the direction of MEG ["READ","SLICE","PHASE"]
Method: ["ARFI" no MEG alternation (conventional MR-ARFI), "Gradient alternation" [18] , "Trigger alternation" [17];
Time Shift: additional delay between the first and second lobe of MEG
Scan delta: the trigger in synchronize "Before" MEG and at each repetition in the time series the synchronization is shifted in time (step 1 ms by default) to range the MEG duration
Trigger Time Shift: shift in time the position of the trigger from its initial position defined by Trigger Position.

The polarities of the MEG were alternated during successive dynamic acquisitions to encode displacement into the phase image with either a positive or negative contribution. An analogic synchronization pulse (TTL) was generated by the MR sequence and sent to the trigger input of the HIFU generator. Its timing (δ) could be adjusted relative to the beginning of the second lobe of the MEG (see Trigger Time Shift parameter in Figure 4.1). This delay influences the apparent displacement that MEG could encode in the phase image, depending on the tissue displacement time-constant. The HIFU sonication was divided into two independent shots with amplitudes noted S_{ARFI} and S_{THERMO}, respectively. S_{ARFI} shot overlapped the second lobe of MEG to encode ARFI displacement and S_{THERMO} was applied during the rest of the time sequence except during the first lobe of the MEG, resulting in a large HIFU duty cycle. The duration of the S_{ARFI} pulse was controlled from the Thermoguide^{TM} console and an additional adjustable delay τ (see Figure 1a) was set before the first lobe of the MEG to allow for tissue mechanical relaxation after S_{THERMO} was stopped.

4.2.3 Reconstruction & pipeline

Raw MR data were streamed in real-time to the open source Gadgetron [22] framework for image reconstruction. Magnitude and phase images were transferred by TCP/IP to Thermoguide^{TM} for online computation and display of temperature images and displacement maps using a customized software.

For each slice the pipeline:

1. computed the temporal standard deviation in each pixel from phase data over the first ten acquisitions in the time series
2. automatically generated an image mask to exclude pixels with a phase standard deviation higher than 0.5 rad
3. performed a temporal phase unwrap of phase data over the computed mask.
4. reconstructed the temperature and displacement maps following eq 4.5 and 4.6.

4.2.4 Ex vivo experiments

Ex vivo validation was performed on ten fresh ex vivo pig muscle samples. A Plexiglas tank filled with deionized water was thermo-regulated at 37 °C. The sample was positioned inside the water tank in a plastic box on top of the ultrasound transducer. Millar membranes (50 μm thick, smaller than 1/30 of the ultrasonic wavelength) were glued to the base of the plastic box and water tank to ensure ultrasound wave propagation from the transducer toward the sample. Two 6-element MR coils were positioned laterally to the Plexiglas tank and an additional single loop coil (19 cm in diameter) was positioned on top of the plastic box containing the muscle sample.

4.2.5 Animal preparation

In vivo validation was performed on the liver of three pigs (Large White x Landrace, ∼40 kg). The protocol was approved by the local Animal Research Ethics Committee "CEEA50" according to the European rules for animal experimentation. After premedication of pigs with ketamine (20 mg.kg^{-1}) and acepromazine (1 mg.kg^{-1}) by an intramuscular injection, the induction of anesthesia was realized with intravenous (IV) bolus of ketamine (15 mg.kg^{-1}) and midazolam (1.5 mg.kg^{-1}). This step was followed by intubation, ventilation and shaving of the thoraco-abdominal region. Depilatory cream (Veet, Reckitt Benckiser, USA) was used to remove residual hair in the sonicated area. The

animal was placed in the prone position on the MR-HIFU platform to avoid transcostal sonication. Figure 4.2 shows the animal positioning with respect to the HIFU transducer. The animal was assisted for ventilation (AESTIVIA, General Electric, Fairfield USA) and maintained under general anesthesia with continuous IV injection of ketamine and midazolam (40 $mg.kg^{-1}.h^{-1}$ and 2 $mg.kg^{-1}.h^{-1}$ respectively). ECG and arterial pressure were recorded during the procedure. MR data was acquired using two 16-element antennas positioned laterally to the thorax and a 19 cm loop coil was positioned underneath the animal on top of the HIFU device. After completion of the treatment, the animal was euthanized with an IV injection of Dolethal (Vetoquinol, Lure, France), until complete cardiac arrest was attested from the ECG trace. The liver was extracted surgically for gross pathology examination.

4.2.6 Human study

Two healthy volunteers were informed about the protocol and consented to be included in the study. They were included in the protocol to assess the mean standard deviation of temperature and displacement measurements on the brain with the proposed sequence. The protocol was performed using 6-element brain array coils where ten slices without spacing between slices were acquired at 1 Hz for 3'20" (200 dynamics acquisition) with FOV = 156x170 mm^{-1}, TR/TE/FA = 100 ms/28 ms/60 °, 1.6x1.6x3 mm^3 voxel size, with a bandwidth of 1447 Hz per pixel with grappa acceleration (factor = 2), A = 25 mT/m, Δ = 5 ms for the MEG. The orientation of MEG was cranio-caudal for all slice orientations. For temperature data analysis, a spatio-temporal baseline correction proposed in a previous publication was performed to correct for phase drift during long acquisitions. Mean standard deviation of temperature and displacement images were then computed and analyzed in a ROI covering the entire brain and in a smaller ROI corresponding to accessible regions of the brain from current clinical HIFU devices. The whole brain ROI was automatically computed on modulus, averaged over all dynamics, taking into account pixels with values above 25 % of mean maximum intensity. This was performed on each slice for each orientation. Displacement and temperature distribution were analyzed in a Box and Whisker plot for each volunteer.

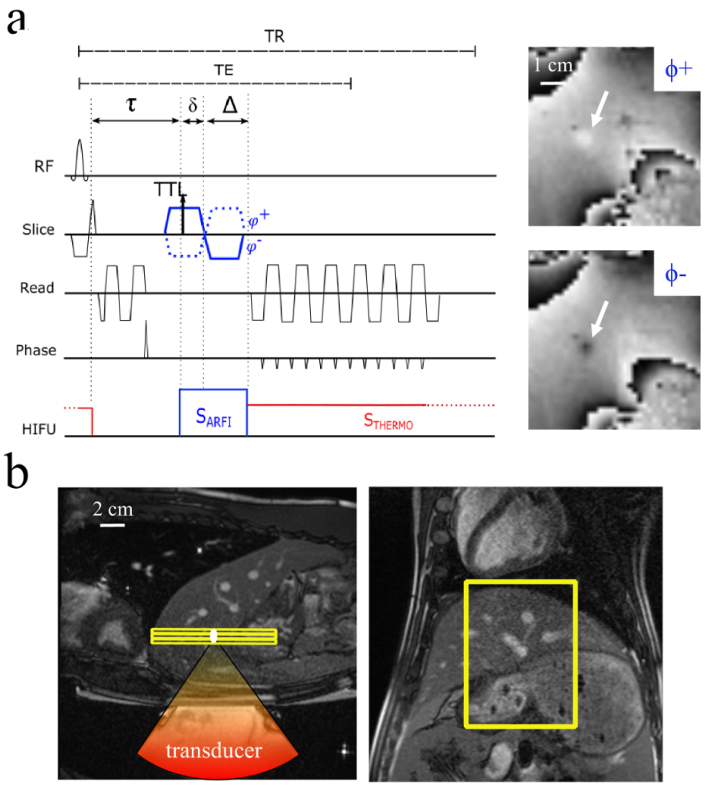

Figure 4.2: Description of the MR thermometry-ARFI method. (a) Schematic of the single-shot echo planar imaging MR thermometry-ARFI sequence integrating MEG (in blue) with alternating polarities (ϕ^+ and ϕ^-) to encode both temperature and ARFI displacement in the phase of the reconstructed MR image. Black arrow shows zero k-space lines used for EPI phase correction. Ultrasound sonications (SARFI) and (STHERMO) are represented in the bottom line. The TTL arrow indicates the timing of the output synchronization signal from the MR acquisition sequence used for triggering the (SARFI) pulse of the HIFU generator. δ and Δ (see material and method section for details) represent the adjustable offset of the TTL signal relative to the beginning of the second lobe of the MEG gradient and the duration of this lobe, respectively. Images on the right display representative phase images for alternative MEG polarities, with the focal spot location indicated by arrows. (b) 2D balanced-SSFP images acquired in sagittal (left) and coronal (right) orientations in vivo on a pig for localization of HIFU transducer, targeting of the beam into the liver and positioning of the acquisition slices for the sequence presented in (a). Yellow lines represent the three slices, centered on the HIFU focal location. The ultrasound cone is represented on the sagittal slice. The white horizontal scale indicated on each image represents 2 cm.

4.2.7 Optimization of the experimental parameters

The apparent displacement derived from MR phase image may be influenced by experimental choices of δ (delay related to time for tissue to reach a steady state during S_{ARFI}) and τ (delay post sonication S_{THERMO} to let tissue relax toward its initial position before encoding next displacement with S_{ARFI}). Thus, a preliminary batch of experiments was conducted in ex vivo muscle to optimize these parameters. The proposed sequence was ran with the following acquisition parameters: one coronal slice with fat saturation, FOV = 92x147 mm2, TR/TE/FA = 800 ms/29 ms/45°, voxel size = 2.1x2.1x5 mm^3, with a

bandwidth of 1500 Hz per pixel, GRAPPA acceleration (factor = 2), A = 25 mT/m, Δ = 5.3 ms.

- Calibration of ARFI measurement without heating ($S_{THERMO} = 0$) allowed to define the practical amplitude S_{ARFI} required to encode displacement and to precisely locate the focal spot location within the targeted region. During this step, 3 to 5 shots with incremental S_{ARFI} amplitude were performed. The sequence was ran with the following parameters:

  1. Ex vivo, three coronal slices with fat saturation, FOV = 92x147 mm^2, TR/TE/FA = 266 ms/29 ms/45°, voxel size = 2.1x2.1x5 mm^3, with a bandwidth of 1500 Hz per pixel, GRAPPA acceleration (factor = 2), A = 25 mT/m, Δ = 5.3 ms and δ = 3 ms for the MEG,
  2. In vivo, three slices in the coronal plan with fat saturation and saturation slabs surrounding the FOV in the phase direction, FOV = 156x170 mm^2, TR/TE/FA = 333 ms/28 ms/50 °, 2.3x2.3x5 mm^3 voxel size, with a bandwidth of 2003 Hz per pixel, GRAPPA acceleration (factor = 2), A = 25 mT/m, Δ = 5.3 ms and δ = 3 ms for the MEG. During sonication, a breath hold of 50 seconds was maintained in order to avoid respiratory motion.

- Ablation procedure with $S_{THERMO} > 0$ and S_{ARFI} determined in step 3, using identical MR acquisition parameters. Temperature and displacement maps were overlaid in real-time on magnitude images, together with temporal evolution of temperature, displacement and thermal dose values in selected pixels located in heated/non heated regions. Three points of interest were identified on the displacement curves to quantify the elasticity contrast: the initial, the maximal and the final value of displacement. The initial value is determined as the first measurement of displacement after the artifact at the onset of HIFU emission.

4.3 Results

4.3.1 Calibration

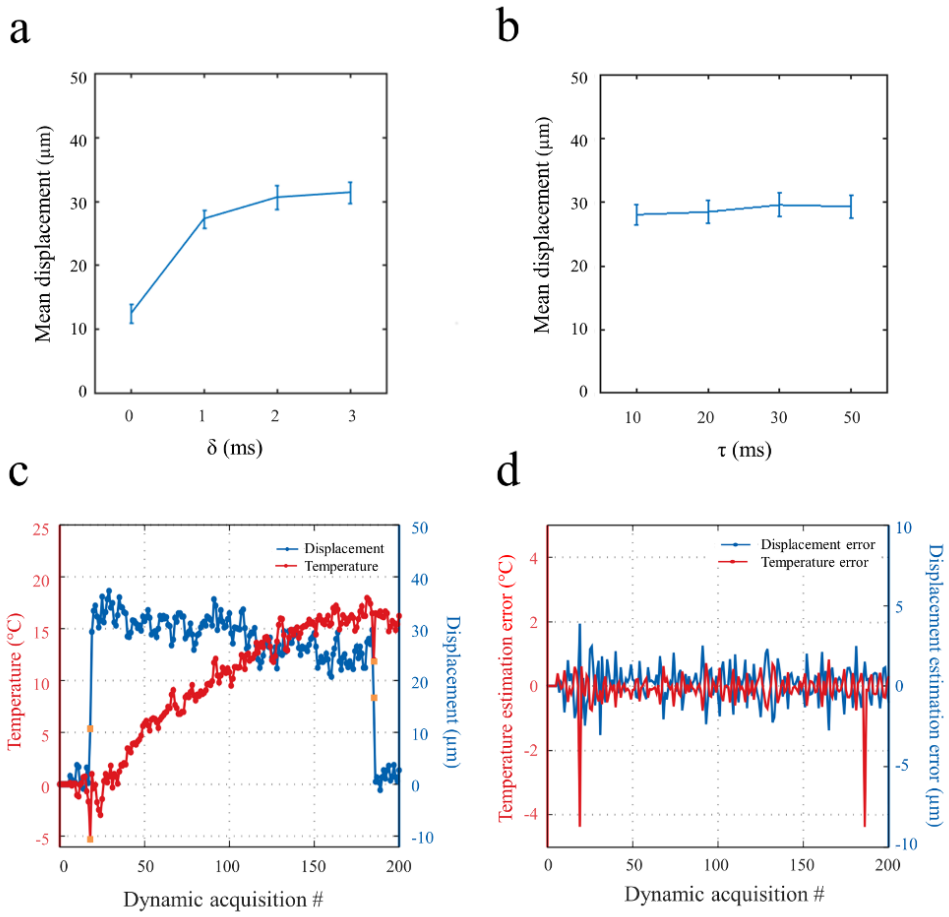

Figure 4.3: Sequence parameter optimization, representative results in ex vivo muscle and errors in temperature and displacement measurement. (a) Mean ± sd of tissue apparent displacement at the focus as a function of δ using $[S_{ARFI}, S_{THERMO}]$ = [198, 0] W. Curves were computed from 50 independent measurements. A plateau of ∼30 μm is reached at δ=2-3 ms. (b) Mean ± sd of tissue apparent displacement at the focus as a function of τ using $[S_{ARFI}, S_{THERMO}]$ = [198, 198] W. For these experiments, δ was set to 3 ms and curves were computed from 10 independent measurements consisting of 5 s sonication duration interleaved with a 10 s cooling period. A mean displacement of around 30 μm (identical to the value reported in (a) when $S_{THERMO} = 0$) is observed whatever the value of τ.Maximal temperature remained below 7 °C (not shown) (c) Representative result of temperature and displacement curves obtained in ex vivo pig muscle with the proposed sequence. Sonication duration was 120 s, with δ =3 ms, τ=10 ms and $[S_{ARFI}, S_{THERMO}]$ = [198, 128] W. Orange squares represent artifacts in temperature and displacement estimates resulting from the data processing (see equation 4.5 and 4.6), when ultrasound is turned on and off, respectively. (d) Computation of the error in temperature and displacement using equation 4.2.1 and 4.8 , from the experimental data plotted in (c). Standard deviation of temperature and displacement are 0.33 °C and 1.0 μm before sonication and 0.30 °C and 1.0 μm during sonication (excluding times points when ultrasound is turned on/off), respectively.

Figure 4.3a shows the apparent displacement for the pixel at the focus measured in ex vivo muscle for δ = 0, 1, 2 and 3 ms. The curve displays a progressive increase in apparent displacement from δ = 0 ms (12.3 ± 1.4 μm) with a plateau near 30 μm reached for δ around 2 to 3 ms. Thus, δ was kept at 3 ms for all ex vivo experiments on muscle. Identical value was used during in vivo for experiments on pig liver based on previously

published data [18] leading to similar observation with a different acquisition sequence.

Figure 4.3b shows the apparent displacement in the pixel at the focus after a 5 s sonication interleaved with a cooling period of 10 s, for different values of τ. Similar values were observed for each experimental condition with a mean apparent displacement around 30 μm, identical to the values reported in Figure 4.3a in the absence of S_{THERMO}. A maximal temperature increase was found below 7 °C (data not shown), indicative of negligible accumulated thermal dose and absence of thermal damage. A value of 10 ms after S_{THERMO} was thus considered sufficient to ensure full relaxation of tissue before next encoding of S_{ARFI} at the following dynamic acquisition in the time series. Figure 4.3c shows sonication performed in ex vivo pig muscle with simultaneous estimation of temperature and displacement. Artifacts (orange squares) at the beginning and completion of the HIFU sonication, resulted from uncompensated MEG encoding in the iterative subtraction of phase images (see Eq 4.5 and 4.6) at these time points.

4.3.2 In vitro and in vivo

Figure 4.3d displays the computed error in temperature and displacement (according to Eq 4.2.1 and 4.8) from the same experiment. The standard deviation of temperature estimation error before and during sonication were 0.33 °C and 0.30 °C, respectively. Displacement estimation led to a standard deviation error of 1.0 μm before sonication and 1.0 mum during sonication.

Figure 4.4 presents typical results of the calibration step obtained ex vivo and in vivo. The displacement and associated temperature increase for the pixel located at the focal spot are displayed for four different acoustic powers applied to the HIFU transducer (Figure 4.3a). The standard deviation of the displacement measured prior to sonication was 1.2 μm ex vivo and 1.4 μm in vivo. Ex vivo, we measured 6, 12, 19 and 32 μm for acoustic power values of 53, 74, 158 and 198 W, respectively. In vivo, we measured 9, 15, 21 and 52 μm maximal displacement for acoustic power values of 99, 158, 198 and 470 W, respectively. Displacement curves as a function of acoustic power were fitted with a linear function to determine the slope (see values on the curves in Figure 4.4c). Maximal temperature increase during this procedure was 2.6 ± 0.3 °C ex vivo and 2.1 ± 0.4 °C in vivo. In Figure 4.4b, displacement and temperature maps were overlaid on magnitude images. Ex vivo and in vivo, the spatial distribution of the temperature remained localized at the focus and did not exceed 3 °C for the hottest pixel demonstrating that tissue was not significantly heated during this procedure.

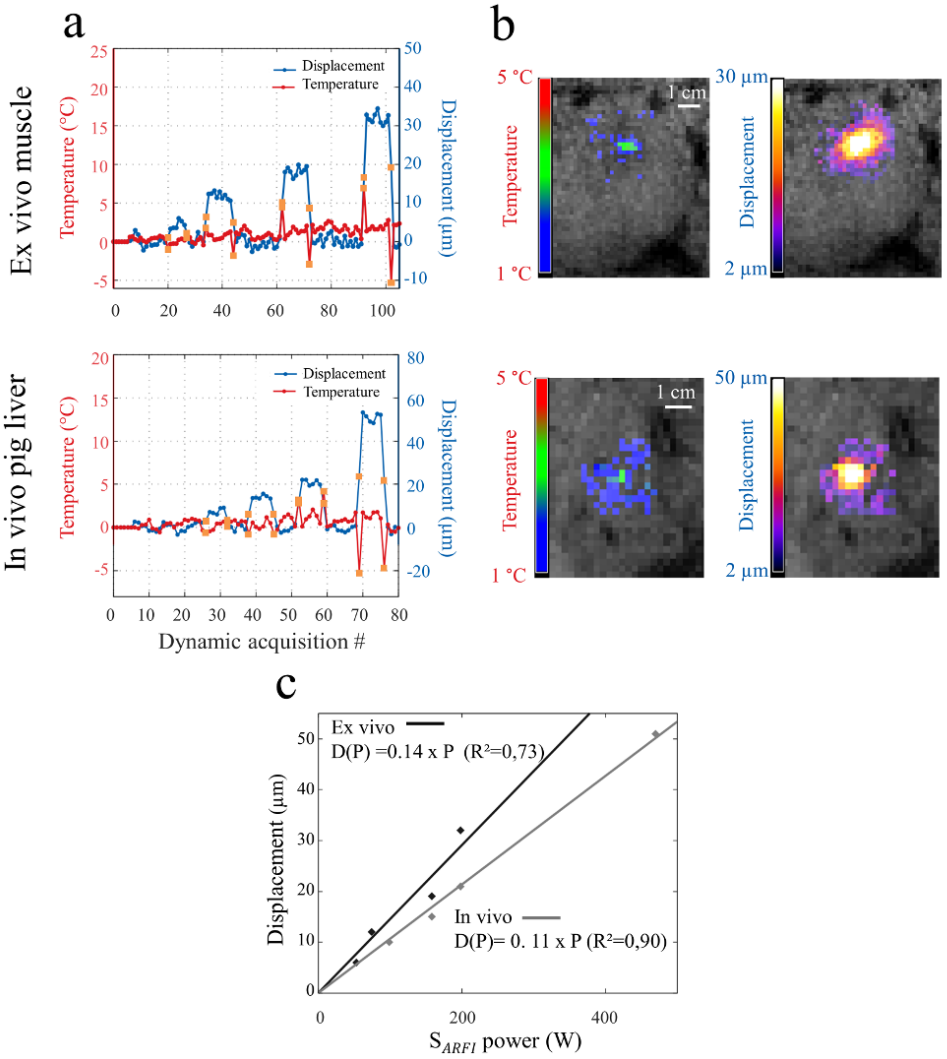

Figure 4.4: Representative results of the calibration step (S_{THERMO}=0) from ex vivo and in vivo experiments. (a) Temporal evolution of displacement (blue curve) and temperature (red curve) in the pixel located at the HIFU focal point. Four sonications were performed with S_{ARFI} of 53, 74, 158 and 198 W ex vivo and 99, 158, 198 and 470 W in vivo, respectively. Orange squares represent artifacts in temperature and displacement estimates resulting from the data processing (see Eq [5] and [6]), when ultrasound is turned on and off, respectively. (b) Corresponding temperature and displacement images overlaid on magnitude images for the fourth HIFU shot. Temperature and displacement scales are indicated on each graph. Horizontal white bar on temperature images represent 1 cm. (c) Plots of displacement measured at the focus as a function of S_{ARFI} for both experiments displayed in (a). Continuous lines represent the result of the linear fit of both curves, with slope and R^2 values indicated on each curve.

Figure 4.5 displays representative results of HIFU ablation for the ex vivo and in vivo experiments with the proposed MR-ARFI-thermometry monitoring method. The values of [S_{ARFI}, S_{THERMO}] were [198, 128] W acoustic for the ex vivo muscle experiment (two minutes sonication) and [470, 470] W in the liver of pig (30 s sonication). Local temperature increase and displacement were visible in both images (Figure 4.5a) at identical spatial locations. In both cases, the temperature increase was associated with a decrease in displacement (Figure 4.5b). Maximal temperature increases were 15 ± 0.4 °C in the

muscle and 26 ± 0.5 °C in the liver, respectively. During sonication, initial, maximal and final displacement values were 30 μm, 32 μm and 23 μm in the muscle and 41 μm, 80 μm and 31 μm in the liver.

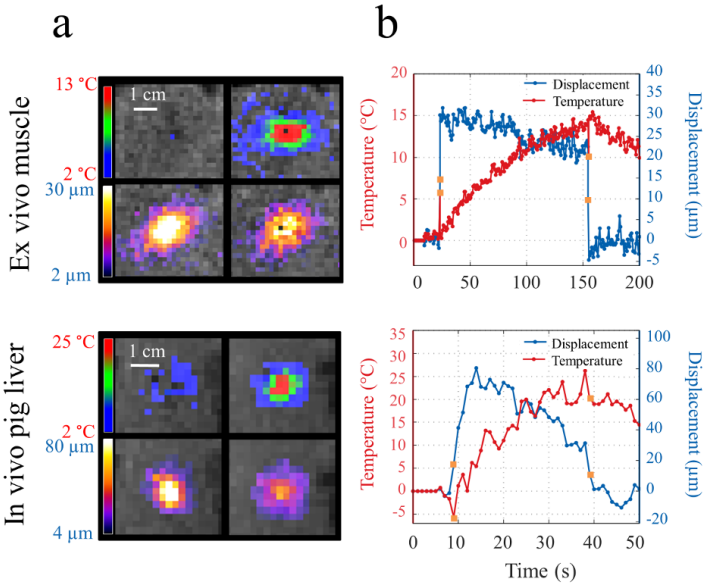

Figure 4.5: Results of representative ex vivo and in vivo experiments during HIFU sonication ($S_{THERMO} > 0$). (a) Temperature (top row) and displacement (bottom row) maps overlaid to magnitude images obtained at the beginning (left column) and at the end (right column) of the HIFU sonication, in ex vivo muscle and in vivo in the liver of one pig. Color bars indicate temperature and displacement scales and the white horizontal bar on temperature images represent 1 cm. (b) Temporal evolution of the temperature and displacement in the hottest pixel. HIFU sonication S_{THERMO} lasted 2 minutes for ex vivo muscle experiment with [S_{ARFI}, S_{THERMO}] of [198, 128] W. For in vivo experiment on the liver of a pig performed under apnea, the sonication duration was 30 s with [S_{ARFI}, S_{THERMO} S_{THERMO}] of [470, 470] W. Orange squares represent artifacts in temperature and displacement estimates resulting from the data processing (see equation 4.6 and 4.5), when ultrasound is turned on and off, respectively.

Figure 4.6a presents comparative results of representative experiments including the temperature, cumulative thermal dose and the displacement curves at the focus. For both ex vivo and in vivo conditions, two examples of results of HIFU sonication are displayed with/without reaching the LTD. When the LTD threshold could not be reached, the maximal displacement remained nearly constant, whereas it decreased when the LTD was reached. In some experiments, the displacement at the beginning of the sonication displayed a progressive increase before reaching the thermal dose (see Figure 4.6b and 4.6d).

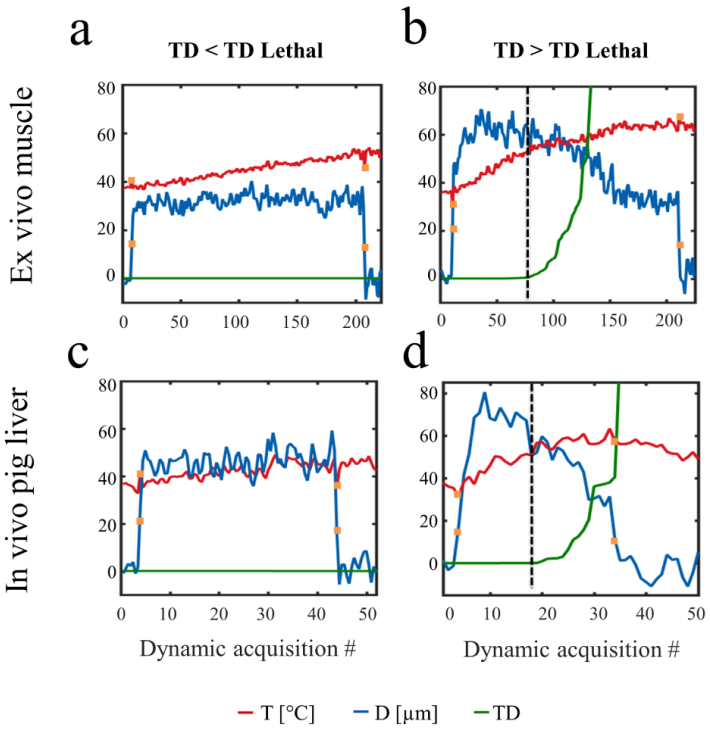

Figure 4.6: Examples of temporal evolution of displacement (D), temperature (T) and accumulated thermal dose (TD) for sonications performed ex vivo (muscle) and in vivo (pig liver). For each graph, temperature (red), displacement (blue) and thermal dose (green) curves are plotted as a function of time. Top row shows representative results obtained on the muscle and bottom row shows representative results in the liver of pig. Graphs in the left column display results where the thermal dose (TD) did not reach the lethal value (LTD), and graphs in the right column display results where the lethal thermal dose was reached (TD > LTD). Orange squares represent artifacts in temperature and displacement estimates resulting from the data processing (see equation 4.5 and 4.6), when ultrasound is turned on and off, respectively. (a) Example of a sonication in muscle resulting in insufficient heating to reach the lethal thermal dose (TD < LTD). (b) Example of a sonication in muscle resulting in sufficient heating to reach the lethal thermal dose (TD < LTD). (c) Example of a sonication in pig liver resulting in insufficient heating to reach the lethal thermal dose (TD > LTD). (d) Example of a sonication in pig liver resulting in sufficient heating to reach the lethal thermal dose (TD < LTD).

Table 4.7 summarizes the results for all the sonications. The maximal variation of the displacement remained below 5 % for all sonications performed with insufficient accumulated thermal dose (maximal temperature increase below 16 °C), whereas it displayed a relative decrease of 21 ± 7 % (ex vivo) and 28 ± 6 % (in vivo) for sonications in which the LTD threshold was reached.

	Ex vivo pig muscle		In vivo pig liver	
	TD > LTD N = 11	**TD < LTD** N = 3	**TD > LTD** N = 8	**TD < LTD** N = 2
TD/LTD ratio (mean ± sd)	60 ± 23	0.7 ± 0.2	20 ± 10	0.5 ± 0.3
Maximum temperature increase [°C]	20 ± 6	14 ± 4	26 ± 7	16 ± 1
From maximal to final displacement decrease [µm]	21 ± 10	4 ± 3	35 ± 14	3 ± 4
From maximal to final relative displacement decrease [%]	30 ± 6	3 ± 2	39 ± 10	5 ± 3
From initial to final displacement decrease [µm]	17 ± 8	4 ± 3	25± 9	3 ± 4
From initial to final relative displacement decrease [%]	21 ± 7	3 ± 2	28 ± 6	5 ± 3

Figure 4.7: Maximal temperature, accumulated thermal dose and tissue displacement at the focus for experiments performed in ex vivo pig muscles and in vivo pig livers Data are sorted as a function of the accumulated thermal dose (TD), depending on whether it reached or not the lethal thermal dose value (LTD). The ratio TD/LTD, maximal temperature increase, absolute and relative displacement decreases are reported as mean ± sd values. N values indicated on top of each column are the number of sonications for each condition.

4.3.3 Results on Volunteers

Figure 6 displays results of the temperature and displacement maps obtained on the brain of volunteer # 2 with the proposed sequence. A volume of 230x160x30 mm^{-3} for each orientation was acquired every second. In the ROI covering the whole brain the median of the mean standard deviation maps of the temperature and displacement in coronal, sagittal and transversal orientations were 0.7 °C and 2.5 μm, 0.7 °C and 1.8 μm, 0.6 °C and 2.2 μm, respectively. In the ROI located in the center of the brain, the mean standard deviation values of the temperature and displacement in coronal, sagittal and transversal orientations were 0.7 °C and 2.4 μm, 0.8 °C and 2.1 μm, 0.7 °C and 2.2 μm, respectively. The box and whisker plots of the distribution of temperature and displacement values in the centered ROI showed that 75 % of the pixels display a temperature and displacement mean standard deviations below 1 $^{-1}$C and 3 μm in coronal orientation, 0.9 °C and 2.6 μm in sagittal orientation and 0.7 °C and 2.8 μm in transversal orientation, respectively.

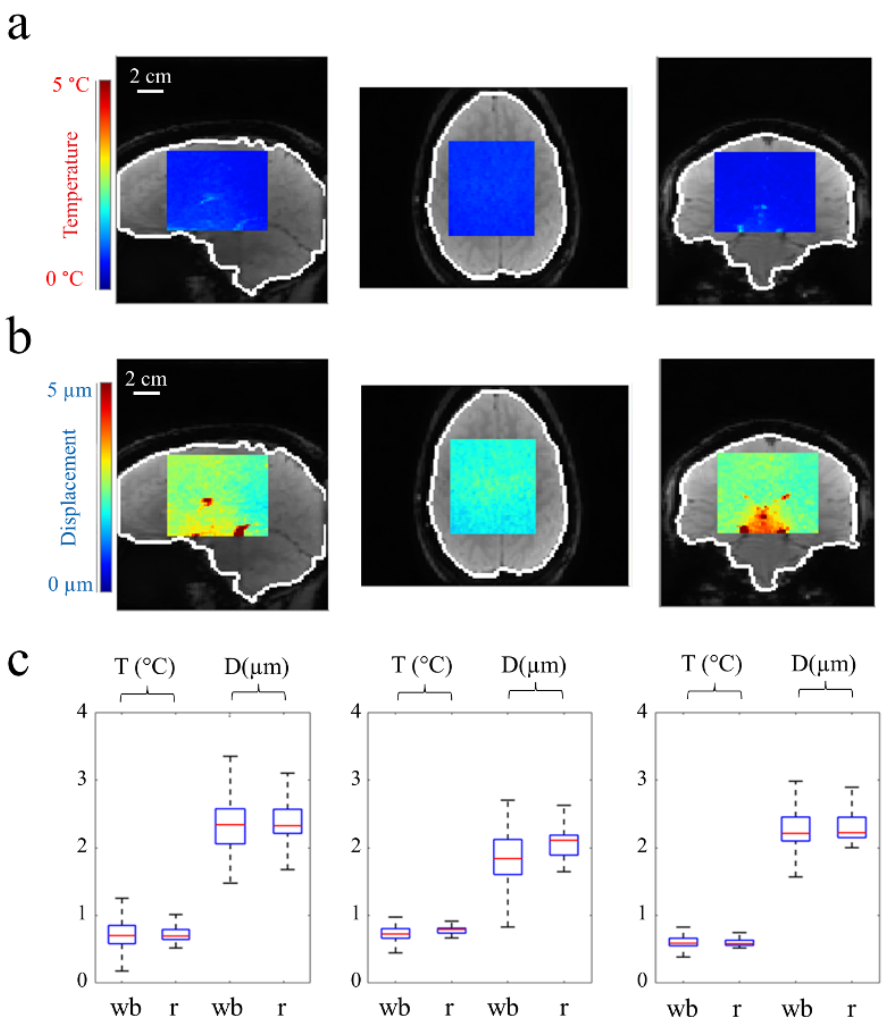

Figure 4.8: Standard deviation maps of temperature and displacement obtained on one volunteer. (a) Central slices of the stack of 10 slices acquired in sagittal (left), transverse (center) and coronal (right) orientations. Temperature standard deviation (color code is indicated on the right) is displayed in the central ROI (see material and method section for details) overlaid on time-averaged magnitude images. The contour of the ROI surrounding the whole brain is indicated by white pixels on each slice. (b) Displacement standard deviation (color code is indicated on the right) in identical ROIs to images displayed in (a). (c) Box and whiskers plots of temperature and displacement distributions with thresholds of 10 %, 25 % (bottom of the blue box), median value (horizontal red line), 75 % (top of the blue box) and 90 %. On horizontal axis of each graph, "wb" stands for whole brain ROI (white contour in (a)) and "r" for the central ROI (displayed in (a)). Data analysis include all data from both volunteers. Horizontal white bars on the images represent 2 cm.

4.4 Discussion

The hybrid MR-ARFI-thermometry sequence and the associated post-treatment allow real-time visualization of temperature and displacement with a repetition time below 100 ms and a spatial resolution of 2.3x2.3x5 mm^3 in vivo. Although the principle of simultaneous measurement of displacement and temperature has already been reported

[18, 17], it remained limited to the assessment of temperature increase during focal spot localization, without adjunction of a second HIFU pulse dedicated to thermal ablation. Moreover, such acquisition sequences were segmented EPI, which required several repetitions to reconstruct one image. Mougenot et al. [17] reported an improvement of 41 % in temperature and displacement measurements without alternating MEG polarity, but using a variable trigger delay for sonication, synchronized alternatively on the first or second lobe of MEG. Such a method may also be implemented with a single-shot EPI. Although voxel size reported in Mougenot et al. [17] and Auboiroux et al. [18] was smaller in the liver using a segmented EPI acquisition sequence with respiratory gating at 3T, the spatial resolution in this study was considered sufficient to monitor temperature and displacement changes during HIFU sonication. Although the tissue displacement was encoded into the MR phase image using the MEG, the computed value of displacement has to be considered as an apparent displacement, since it is averaged over the voxel size and that its value may also be affected by sub optimal choice of τ and δ. For this purpose, an experimental approach was proposed to optimize these parameters, as illustrated in Figure 4.3.

In our experimental conditions the error in the estimation of temperature and displacement (see equation 4.2.1 and 4.8) were $|\frac{\alpha_D}{2.\alpha_T}| = 0.16$ °C.μm^{-1} and $|\frac{\alpha_T}{2.\alpha_D}| = 1.5$ μm.°C^{-1} ex vivo, and $|\frac{\alpha_D}{2.\alpha_T}| = 0.17$ °C.μm^{-1} and $|\frac{\alpha_T}{2.\alpha_D}| = 1.5$ μm.°C^{-1} in vivo, respectively. The standard deviation of the error in temperature and displacement estimates (see Figure 4.3d) showed similar values before and during sonication. These values depended on the experimental noise in phase images and on the proposed processing method. The latter contribution can be minimized by rapid sampling to avoid important variations of temperature and displacement between successive measurements (see Eq 4.2.1 and 4.8). This justifies the use of a rapid imaging sequence based on a single-shot EPI acquisition. In vivo on the liver of pig, only a limited period of acquisition was available (50 s) due to apnea. The ablation process was required to be quicker (30 s) than for sonications performed in ex vivo muscle. Hence, signal-to-noise ratios of temperature and displacement curves were lower than for the results obtained in ex vivo muscle.

However, with the proposed MEG combination of parameters (Δ = 5.3 ms and A = 25 mT/m), the displacement sensitivity was 14.1 μm.rad^{-1} and standard deviation of temperature and displacement measurements were found to be sufficient for visualizing the focal spot ex vivo in skeletal muscle and in vivo in pig livers.

In the proposed method, the loss in sonication duty cycle was limited ($\sim$ 15 %) and

corresponded to the dead time at the beginning of the sequence to allow the tissue to mechanically relax toward its initial position before the next ARFI displacement encoding. Results obtained during this study indicate that energy deposition under these experimental conditions was sufficient to create thermal lesions in muscle and liver and to quantify simultaneously tissue mechanical changes at the focal point through apparent displacement variations, temperature distribution in the heated area and thermal dose evolution. Displacement amplitudes found ex vivo on pig muscle (~ 40 μm) are in agreement with those from Mougenot et al. [17]. Auboiroux et al. [18] reported from in vivo pig liver, a lower displacement (less than 15 μm) during a transcostal sonication, whereby a significant portion of acoustic power was absorbed by the rib cage. In our experimental conditions, displacement estimations were higher. However, Figure 4.4b and 4.4c showed a linear relationship between displacement and acoustic power in the range of acoustic powers used in this study. Thus, induction of nonlinear effects that could interfere with displacement measurement is unlikely under these experimental conditions.

The proposed faster implementation enables acquisition of several slices in a subsecond temporal resolution, calibration of S_{ARFI} with negligible acoustic energy deposition (attested by absence of heating, see Figure 4.4) and provides full flexibility on the balance between displacement sensitivity and acoustic energy deposition for ablation. In the present work, sonication of S_{ARFI} during the ablation procedure could have been maintained before and after $S_{THERMO} > 0$ for continuous monitoring of displacement but this was not implemented for practical reasons.. Our results are in agreement with recent studies on elasticity monitoring during HIFU ablation using either ultrasound shear wave imaging (SWI) [23] or harmonic motion imaging [24]. Hou et al. [25] observed a decrease of displacement and Arnal et al. [23] observed an increase of shear modulus for temperatures higher than 55 °C.

The overall decrease of displacement found in this study could be attributed to increased shear modulus during tissue denaturation (qualitative elasticity contrast). Another driving factor of focal displacement change is the potential variation of attenuation with temperature. A previous study [26] reported that attenuation is increasing with temperature (51 % attenuation increase for temperature increase from 37 °C to 65 °C), which would result in an apparent increase of displacement at the focal point. Such an increase in displacement could be observed at the beginning of thermal accumulation and before reaching the lethal thermal dose on Figure 4.6b and 4.6d for in vivo and ex vivo experiments. Values are consistent with the linear slope reported by Arnal et al.

[23] below 50 °C, using shear wave imaging. Such an increase in displacement may also have been attributed to rapid boiling at the focus that would locally modify tissue stiffness, as reported by Khokhlova et al. [27] and Elbes et al.[7]. However, Khoklova et al. reported that boiling can occur in a few milliseconds although the increase in displacement observed in Figure 4.6 lasts several seconds. Moreover, as already mentioned above, nonlinear effects are unlikely to occur in our experiments. Addition of backscattered ultrasound signal measurement during sonication to monitor non-linear ultrasound effects may provide additional information. Qualitative gross pathology observations of the tissue was performed to verify the presence of thermal lesion, but no inference of lesion extent based on displacement variation has been made in this paper that focuses on presenting a new MR acquisition method. Further studies could encompass mapping displacement variation using beam steering capabilities of the HIFU probe then correlating measured lesion extent with post-ablation imaging.

This single-shot EPI thermometry-ARFI sequence allows rapid focal spot localization using only two HIFU pulses, since the first measurement correspond to the artifact at the onset of HIFU sonication. However, the resulting energy deposition remains limited, as illustrated by negligible temperature increases observed in Figure 4.4. As such, it may provide a safer way to identify the effective sonication beam's location in the targeted area than the usual methods relying on the observation of local temperature increase during pre-intervention sonication performed at low energy.

MRgHIFU brain therapies are increasingly used for new clinical applications and may benefit from improved temporal and spatial quantitative monitoring, as current monitoring methods are restricted to a single slice with limited spatial resolution and temporal update [28, 29, 30]. Using our sequence with 10 slices per second and taking advantage of the higher signal-to-noise ratio and the longer T2* in the brain, the spatial resolution of the temperature and displacement images were improved, with a resulting voxel dimension (1.6x1.6x3 mm^3) in the same range as the focal spot dimension of current clinical HIFU devices. On Figure 4.8c, the mean standard variation of displacement was below 2.5 μm. Experiments performed in ex vivo human skull [31] showed displacements over 20 mm using phase aberration corrections methods.

Although direct comparison of displacement on in vivo and ex vivo brain tissue must be taken with care, our results in terms of standard deviation of displacement in the brain open promising perspectives for the application of this method for clinical treatment. Thus, mechanical changes associated with temperature increase during HIFU ablation

could be monitored more precisely. Moreover, current clinical brain therapy MR-HIFU devices operate at 3T and are equipped with stronger gradients, which could potentially provide better spatial resolution on both temperature and displacement images and more accurate measurements, thanks to an increased signal-to-noise ratio.

Several studies have reported the added value of exploiting nonlinear acoustic propagation (e.g. cavitation, boiling) to increase heating efficiency at constant acoustic energy and to protect organs located in the far field of the HIFU beam[9, 32]. The present method would allow rapid calibration of the HIFU power and slice position for exploiting such effects on the liver, as suggested by Ramaekers et al. [6]. In addition, this study proposed to use a respiratory gated sonication which overcomes the use of real-time motion compensation strategies on temperature and displacement images, although these methods have only been evaluated in preclinical studies where breathing was fully controlled.

The proposed method may still benefit from further improvements. Particularly, no motion and susceptibility-related compensation were incorporated in the treatment pipeline, as the main objective of the study was to describe a new MR thermometry-ARFI acquisition sequence and provide experimental data illustrating the additional information given by the method for monitoring HIFU ablation in soft tissue. For in vivo experiments in the liver, displacement of the target relative to the HIFU probe was suppressed by breath holding. However, several correction methods for magnitude and phase images are available to compensate motion and associated susceptibility artifacts [33] and could be applied to allow free breathing temperature and displacement imaging on mobile organs, together with real-time locking of the HIFU beam on the target. In our experiments, the spatial resolution was experimentally adjusted as a tradeoff between signal-to-noise ratio, echo train duration and T2* decay, which resulted in acceptable standard deviation on both temperature and displacement measurements.

4.5 Conclusion

This chapter proposes a new rapid MRI sequence for subsecond, multi-slice, simultaneous monitoring of displacement at the focus and temperature distribution during HIFU ablation in soft tissue, while preserving high duty cycle for efficient acoustic energy deposition. Changes in the order of 20 % in tissue displacement amplitude were observed during both ex vivo and in vivo MR-HIFU experiments when lethal thermal dose was reached. The use of such metrics may thus be explored in future studies to assess poten-

tial tissular modifications during HIFU therapy in complement to conventional thermal dose imaging.

4.6 Perspectives

This study was a first step for the validation of the sequence and the associated pipeline of reconstruction, performed on a static organ. For the heart, further developments will be required.

Firstly, magnetic susceptibility artifacts corrections have to be incorporated in the treatment pipeline similarly to already published methods used for thermometry [34]. In addition, these susceptibility artifacts corrections have to take into account the MEG alternating polarity. Figure 4.9 shows the proposed modifications of the current pipeline, proposed in [34], for both temperature and displacement monitoring.

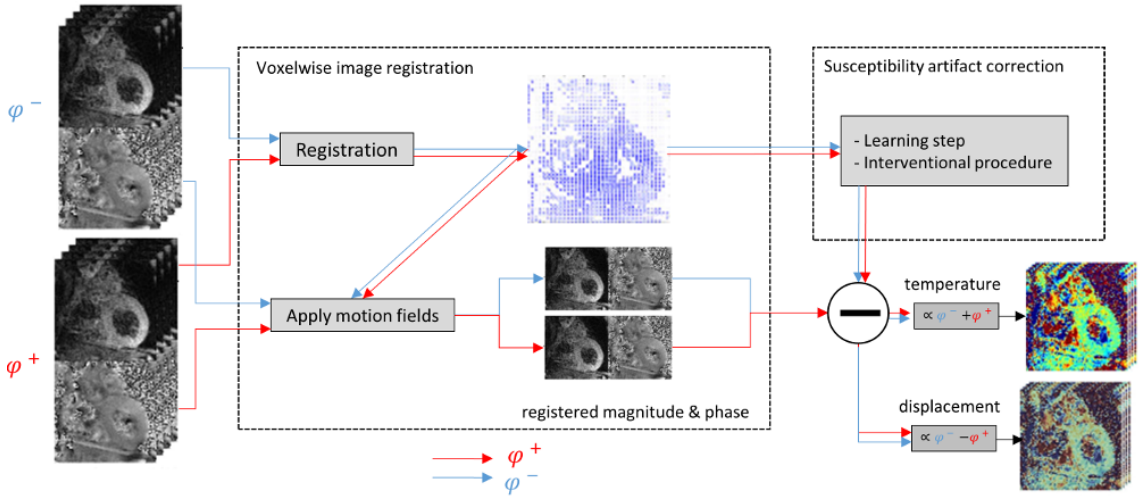

Figure 4.9: Susceptibility artifact Modified pipeline of reconstruction incorporating magnetic susceptibility artifacts corrections. Modifications consist of distinguishing between positive and negative polarities and apply the existing algorithm separately on both polarities.

The second part concerns the improvement of the temporal resolution. The proposed method requires two acquisitions to estimate the temperature and displacement simultaneously. However on the heart, only a limited period of the cardiac cycle is available with limited cardiac motion. As a consequence, only few slices could be acquired with the current implementation of the sequence. To overcome this limitation, we are currently working on EPI simultaneous multislice acquisitions [35] , dedicated to cardiac applications. A first prototype sequence is currently under validation. This sequence allows to acquire several slices at the same time point, reducing the acquisition time by a factor called slice acceleration factor. As of now, only one study has investigated simultane-

ous multislice acquisitions for thermometry [36], showing clear improvement in sequence acquisition time with negligible artifacts in temperature estimates.

Moreover, depending on the ultrasound device used (fully non-invasive, mini invasive, embedded in a catheter), motion compensation of the focus position might be required, to achieve both an effective ablation and a good monitoring of displacement variations.

During this thesis, we have not managed to perform cardiac ablations in vivo with the current setup. The main limitation was the geometry of our 256 transducer array (D=14.5 cm), which was not optimized for targeting the heart. Indeed, its large aperture intercepted ribs and lungs, reducing dramatically the acoustic power available at the focus. For further validations on the heart, several HIFU emitters could be envisioned:

1. Direct application of ultrasound power using an HIFU transducer embedded inside a catheter as proposed in Nazer et al.[37]. Such device would not require any physiological motion compensation of the focus position, as the catheter can be stuck onto the cardiac wall. Transducer designs using Capacitive Micromachined Ultrasonic Transducers (CMUT) [38] are very promising for future ultrasound catheters.

2. Trans-oesophagus probe as proposed by Bessiere et al. [39], which circumvent the acoustic power attenuation due to the rib cage.

3. Intercostal approach using a transducer array close to the design of ultrasound probes used for cardiac ultrasound imaging. This probe would request motion compensation of the focus position for an effective ablation. Overall, this solution seems to be a much more difficult to achieve.

4.7 References

[1] Samantha Ellis et al. “Clinical applications for magnetic resonance guided high intensity focused ultrasound (MRgHIFU): Present and future: Clinical applications for MRgHIFU”. en. In: *Journal of Medical Imaging and Radiation Oncology* (Aug. 2013).

[2] Hyun Joo Jang et al. “Current and Future Clinical Applications of High-Intensity Focused Ultrasound (HIFU) for Pancreatic Cancer”. en. In: *Gut and Liver* (Sept. 2010).

[3] John De Poorter. "Noninvasive MRI thermometry with the proton resonance frequency method: study of susceptibility effects". In: *Magnetic Resonance in Medicine* (1995).

[4] R.L. Clarke and G.R. ter Haar. "Temperature rise recorded during lesion formation by high-intensity focused ultrasound". In: *Ultrasound in Medicine & Biology* (1997).

[5] Emilie Sapin-de Brosses et al. "The link between tissue elasticity and thermal dose in vivo". en. In: *Physics in Medicine and Biology* (Dec. 2011).

[6] P. Ramaekers et al. "Increasing the HIFU ablation rate through an MRI-guided sonication strategy using shock waves: feasibility in the in vivo porcine liver". en. In: *Physics in Medicine and Biology* (2016).

[7] Delphine Elbes et al. "Magnetic Resonance Imaging for the Exploitation of Bubble-Enhanced Heating by High-Intensity Focused Ultrasound: A Feasibility Study in ex Vivo Liver". en. In: *Ultrasound in Medicine & Biology* (May 2014).

[8] S D Sokka et al. "MRI-guided gas bubble enhanced ultrasound heating in in vivo rabbit thigh". In: *Physics in Medicine and Biology* (Jan. 2003).

[9] Vesna Zderic et al. "Prevention of post-focal thermal damage by formation of bubbles at the focus during high intensity focused ultrasound therapy". In: *Medical Physics* (2008).

[10] Nathan McDannold and Stephan E. Maier. "Magnetic resonance acoustic radiation force imaging". In: *Medical Physics* (2008).

[11] Marcus Radicke et al. "New image contrast method in magnetic resonance imaging via ultrasound". In: *HFI/NQI 2007*. Springer, 2008.

[12] Elena A. Kaye et al. "Application of Zernike polynomials towards accelerated adaptive focusing of transcranial high intensity focused ultrasound". In: *Medical physics* (2012).

[13] Yoni Hertzberg et al. "Rapid method for assessing relative tissue stiffness using MR acoustic radiation force imaging". en. In: *International Journal of Imaging Systems and Technology* (Mar. 2014).

[14] Po-Hsiang Tsui et al. "In vitro effects of ultrasound with different energies on the conduction properties of neural tissue". en. In: *Ultrasonics* (June 2005).

[15] R. T. Mihran et al. “Temporally-specific modification of myelinated axon excitability in vitro following a single ultrasound pulse”. eng. In: *Ultrasound in Medicine & Biology* (1990).

[16] Michael Plaksin et al. “Intramembrane Cavitation as a Predictive Bio-Piezoelectric Mechanism for Ultrasonic Brain Stimulation”. en. In: *Physical Review X* (Jan. 2014).

[17] Charles Mougenot et al. “Variable ultrasound trigger delay for improved magnetic resonance acoustic radiation force imaging”. In: *Physics in Medicine and Biology* (Jan. 2016).

[18] Vincent Auboiroux et al. “ARFI-prepared MRgHIFU in liver: Simultaneous mapping of ARFI-displacement and temperature elevation, using a fast GRE-EPI sequence”. en. In: *Magnetic Resonance in Medicine* (Apr. 2012).

[19] J. A. de Zwart et al. “Fast magnetic-resonance temperature imaging”. eng. In: *Journal of Magnetic Resonance. Series B* (July 1996).

[20] Stephen A. Sapareto and William C. Dewey. “Thermal dose determination in cancer therapy”. In: *International Journal of Radiation Oncology*Biology*Physics* (Apr. 1984).

[21] W. C. Dewey. “Arrhenius relationships from the molecule and cell to the clinic”. en. In: *International Journal of Hyperthermia* (Jan. 1994).

[22] Michael Schacht Hansen and Thomas Sangild Sørensen. “Gadgetron: An open source framework for medical image reconstruction”. en. In: *Magnetic Resonance in Medicine* (2013).

[23] B. Arnal et al. “Monitoring of thermal therapy based on shear modulus changes: II. Shear wave imaging of thermal lesions”. In: *IEEE Transactions on Ultrasonics, Ferroelectrics and Frequency Control* (Aug. 2011).

[24] C Maleke and E E Konofagou. “Harmonic motion imaging for focused ultrasound (HMIFU): a fully integrated technique for sonication and monitoring of thermal ablation in tissues”. In: *Physics in Medicine and Biology* (Mar. 2008).

[25] Gary Y. Hou et al. “High-intensity focused ultrasound monitoring using harmonic motion imaging for focused ultrasound (HMIFU) under boiling or slow denaturation conditions”. In: *IEEE Transactions on Ultrasonics, Ferroelectrics, and Frequency Control* (July 2015).

[26] Christakis A. Damianou et al. "Dependence of ultrasonic attenuation and absorption in dog soft tissues on temperature and thermal dose". In: *The Journal of the Acoustical Society of America* (1997).

[27] Tatiana D. Khokhlova et al. "Magnetic resonance imaging of boiling induced by high intensity focused ultrasound". en. In: *The Journal of the Acoustical Society of America* (Apr. 2009).

[28] Daniel Coluccia et al. "First noninvasive thermal ablation of a brain tumor with MR-guided focused ultrasound". In: *J Ther Ultrasound* (2014).

[29] Stephen J. Monteith et al. "Transcranial magnetic resonance–guided focused ultrasound surgery for trigeminal neuralgia: a cadaveric and laboratory feasibility study: Laboratory investigation". In: *Journal of neurosurgery* (2013).

[30] Jin Woo Chang et al. "Neurophysiologic Correlates of Sonication Treatment in Patients with Essential Tremor". en. In: *Ultrasound in Medicine & Biology* (Jan. 2015).

[31] L. Marsac et al. "MR-guided adaptive focusing of therapeutic ultrasound beams in the human head". In: *Medical Physics* (2012).

[32] T. Douglas Mast et al. "Acoustic Emissions During 3.1 MHz Ultrasound Bulk Ablation In Vitro". en. In: *Ultrasound in Medicine & Biology* (Sept. 2008).

[33] Baudouin Denis de Senneville et al. "Real-time adaptive methods for treatment of mobile organs by MRI-controlled high-intensity focused ultrasound". en. In: *Magnetic Resonance in Medicine* (Feb. 2007).

[34] Valéry Ozenne et al. "Improved cardiac magnetic resonance thermometry and dosimetry for monitoring lesion formation during catheter ablation". In: *Magnetic resonance in medicine* (2017).

[35] Markus Barth et al. "Simultaneous multislice (SMS) imaging techniques: SMS Imaging". en. In: *Magnetic Resonance in Medicine* (Jan. 2016).

[36] P T S Borman et al. "Towards real-time thermometry using simultaneous multislice MRI". In: *Physics in Medicine and Biology* (Sept. 2016).

[37] Babak Nazer et al. "Epicardial Catheter Ablation Using High-Intensity Ultrasound". In: *Circulation: Arrhythmia and Electrophysiology* (2015).

[38] Omid Farhanieh et al. "Integrated HIFU Drive System on a Chip for CMUT-Based Catheter Ablation System". In: *IEEE Transactions on Biomedical Circuits and Systems* (2017).

[39] Francis Bessiere et al. “Ultrasound-Guided Transesophageal High-Intensity Focused Ultrasound Cardiac Ablation in a Beating Heart: A Pilot Feasibility Study in Pigs”. en. In: *Ultrasound in Medicine & Biology* (Aug. 2016).

CHAPTER 5

3D ultrasound-based motion tracking

Contents

5.1 Introduction

This chapter studies a standalone ultrasound based motion tracking method, combined with real-time monitoring of temperature evolution using MR-thermometry. In this study,

we have validated the method during HIFU ablations (thermal applications) but focus correction could also be of particular interest for transient applications of ultrasounds.

Personal contributions:

- Implementation of the ge-ssEPI echo-navigated sequence.
- Ultrasound signal acquisitions and implementation of the motion correction algorithms.
- Participation to all ex vivo and animal experimentations.
- Data post-treatment and production of figures.

5.1.1 Literature

MRgHIFU therapies have been successfully delivered clinically in static organs such as brain [1], bones [2] or uterus [3]. However, treatments of mobile organs (e.g. liver, kidney, pancreas, heart ...) are significantly more challenging. Respiratory motion amplitude (typically 10 mm with 10 mm.s^{-1} maximal speed [4]) is greater than the focus size (eg. $\sim$2 mm at -6 dB in the direction transverse to the axis of propagation). Thereby, HIFU focus has to be steered in real-time to follow the targeted tissue position in order to deposit heat at the desired location, reduce the treatment time and improve the safety of the procedure [5] by avoiding overheating of the surrounding tissues [6].

Several methods have been proposed to extract organ motion, either using MR-based information or through external sensors. In the first approach, extraction of the respiratory motion has been proposed by tracking anatomical contours [7] in 2D using optical flow algorithms [8], or in 1D using an echo navigator [9]. An MR-based 3D motion tracking was proposed by combining the two aforementioned methods [10]. The second approach relies on 1D ultrasound signal [11] or 2D ultrasound imaging combined with optical flow algorithms. More recently, a 2D ultrasound imaging correction method combined with an MR-navigator echo perpendicular to the imaging plane was proposed for a full 3D correction [12]. Even though these methods have shown good correction capabilities, they suffer either from an update time slaved to the imaging time resolution, need to operate an additional device inside the magnet or lack of three-dimensional correction. Ideally, a 3D motion correction should be precise (millimeter uncertainty), independent from the MR acquisition system (to avoid imposing strong compromises on the imaging strategy) and require minimal modifications of the hardware to remain compatible with limited available space inside the magnet. A standalone, ultrasound-based 3D motion

tracking has been introduced in Pernot et al. [13] using several elements of the therapeutic transducer in reception. This method estimates the displacement by monitoring temporal shifts in the back-scattered ultrasound (US) signals produced by HIFU pulses shot from different locations of the transducer. Using a triangularization algorithm one can retrieve the organ displacement near the focal point and steer the beam accordingly. However, this technique has only been validated outside the MRI [14] and could be of major interest for MRgHIFU on mobile organs.

As a matter of fact, monitoring temperature with MRI on mobile organs is also not trivial, since it requires combination of fast acquisition methods with real-time image processing to register each image in the time series at the same position and compensate for susceptibility artifacts on phase images and resulting temperature maps. Although several studies reported precise thermometry on liver [15], kidney [16] and heart [17], a compromise is usually made between acquisition speed, volume coverage, spatial resolution and thermometry uncertainty. Thus, having a fully decoupled MR-thermometry pipeline and HIFU beam steering may provide an ideal situation where MRI may be optimized to increase volume coverage for enhanced safety of the therapeutic procedure (e.g. monitoring temperature in organs located in the near and far fields of the HIFU beam and near the focus) and/or avoid compromises on image resolution or acquisition speed.

5.1.2 Objective

In this study, we propose a 3D ultrasound-based motion compensation for online HIFU beam steering combined with rapid MR-thermometry (using the proton resonance frequency shift (PRFS) [18] method) . Such a method is expected to improve acoustic energy deposition at the desired location to increase treatment efficiency while providing online volumetric temperature imaging for enhanced safety. The methods are evaluated in vitro in an agar phantom mounted on a motion controller and in vivo in the liver of pig.

5.2 Materials and Methods

5.2.1 3D ultrasound motion correction

3D motion correction was performed using four sub-apertures (i = [1:4]) composed of one element in reception surrounded by six elements in emission in order to produce a focused ultrasound beam (Figure 5.1a). Each of these four elements could thus not

be used for emission. Band-rejecter filters tuned at the MR-frequency (64 MHz) were inserted into each corresponding transmission line to prevent potential interferences from the MR-sequence. A 2 ms sonication at 22 W acoustic power was emitted simultaneously on the four sub-apertures to produce a back-scattered signal from the tissue speckle. Each sub-aperture estimated the displacement along its normal direction A_i (a_{ix}, a_{iy}, a_{iz}) in a pulse-echo mode, as shown by yellow arrows in Figure 5.4a). Then, the displacement estimation pipeline followed these steps (see Figure 5.2):

1. Ultrasound backscattered signals received upstream (20 mm downward the focal spot toward the transducer) from the ultrasonic focus were sampled (Oscar, Gage Applied Technologies, Dynamic Signal LLC, IL, USA) at a frequency of 100 MHz (1250 points, for an acquisition duration of 12.5 μs) simultaneously on each channel. In a preliminary step before ablation, the acquisition window was adjusted by 5 mm steps in depth, to find the optimal displacement content in US acquisitions.

2. Setting of mean correlation thresholds (see $\overline{Corr_{t=0,t+dt}}$ and $\overline{Corr_{t=t,t+dt}}$ on Figure 5.2) for absolute estimation and for dumping low correlated signals. This step prevents two situations of displacement estimation error. 1) Drift due to cumulative error in displacement estimation and 2) local displacement discontinuities due to insufficient correlations between measurements. These two cases have been addressed separately (see Figure 5.2 legend for details) using different thresholds determined experimentally.

3. 1D cross-correlation was calculated between two consecutive signals acquired from each of the four sub-apertures. From this calculation, the temporal lag T_i defined as the temporal shift at maximum correlation was computed.

   Based on the pulse/echo theory, T_i is linked to $D(d_x, d_y, d_z)$ as:

$$T_i = \frac{2}{c} \begin{pmatrix} a_{ix} \\ a_{iy} \\ a_{iz} \end{pmatrix} \begin{pmatrix} d_x \\ d_y \\ d_z \end{pmatrix} \quad i \in [1, 4]$$

   Where c is the speed of sound set to 1600 m.s^{-1}.

4. The pseudo-inverse of the system [1] allowed to retrieve the displacement $\vec{D}$ between

t and t + dt in the transducer frame of reference ($\vec{x}$,$\vec{y}$,$\vec{z}$).

5. Current focus position ($\overrightarrow{FP_{t+dt}}$) is then calculated as $\overrightarrow{FP_t} + \vec{D}$ where $\overrightarrow{FP_t}$ is the previous focus position

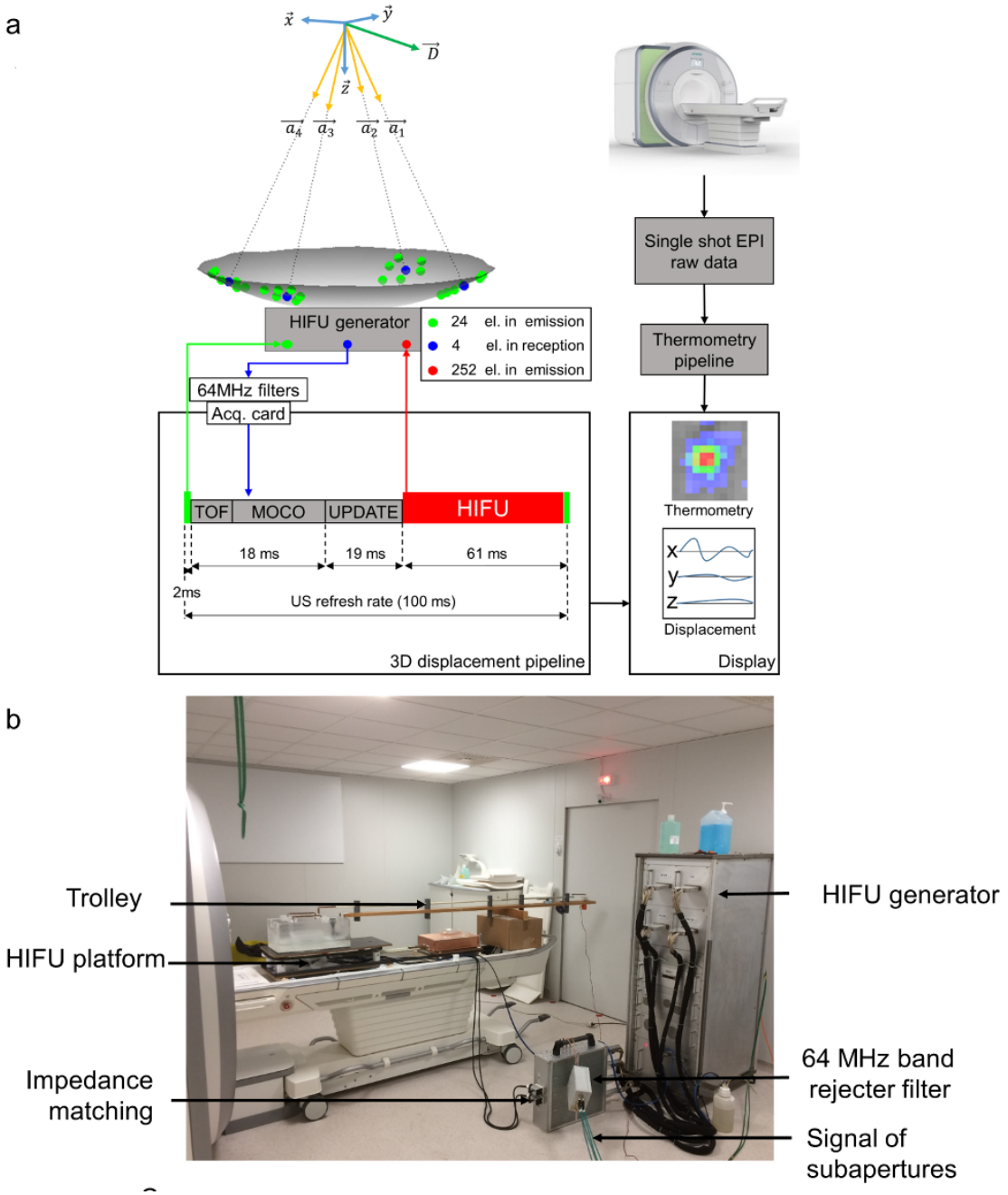

Figure 5.1: 3D ultrasound-based motion tracking and MRI thermometry pipeline. a: schematic of the 3D ultrasound-based motion estimation system. The 256 elements HIFU transducer is represented in gray. Transducer elements operating in emission are represented in green and those in reception in blue, respectively. ($\vec{x}$,$\vec{y}$,$\vec{z}$) is the transducer spatial reference frame of coordinates, where the displacement $\vec{D}$ (green arrow) is estimated. $\vec{a_i}$,i[1,4] represents the normal vector of each sub-aperture along which the displacement is measured using a pulse-echo mode. The pipeline of 3D displacement estimation is presented underneath. TOF: Time Of Flight for ultrasound to reach the depth of interest; motion correction (MOCO): computing time for the displacement estimation, UPDATE: transducer phase law update (see material and methods section for details). HIFU: additional ultrasound sonication to induce temperature increase of the tissue. Refresh rate is given by durations of TOF (150 mus for typical distance of 12 cm) + MOCO (18 ms) + UPDATE (19 ms) + HIFU (adjustable depending on desired update rate).
b) Picture of the in vitro validation setup inside the MR-room.

Decision tree for incoming US-data allowed to correct for displacement estimation drifts and local displacement estimation discontinuities. Drifts have been corrected by taking the first US-acquisition in the time series as the initial position of reference. During the displacement monitoring, if the averaged cross-correlation between current and the reference US-acquisition (see $\overline{Corr_{t=0,t+dt}}$ in Figure 5.2). was greater than a predefined threshold (experimentally tuned between 0.997 and 0.999 for in vitro experiments and between 0.977 and 0.983 for in vivo experiments), the previous focus position $\overrightarrow{FP_t}$ was reset to its initial position [0 0 0] and current focus position was computed as $\overrightarrow{FP_{t+dt}} = \overrightarrow{FP_t} + \vec{D} = \vec{D}$.The reset of the position was restrained to one occurrence per respiratory cycle. Potential discontinuities induced by artifact signals were suppressed by discarding the current acquisition if the averaged cross-correlation between current and previous acquisition (see $\overline{Corr_{t,t+dt}}$ in Figure 5.2) was lower than 0.80. The number of such adverse events was recorded to assess the robustness of the method. When focus correction was disabled, $\overrightarrow{FP_{t+dt}}$ was set to [0 0 0].

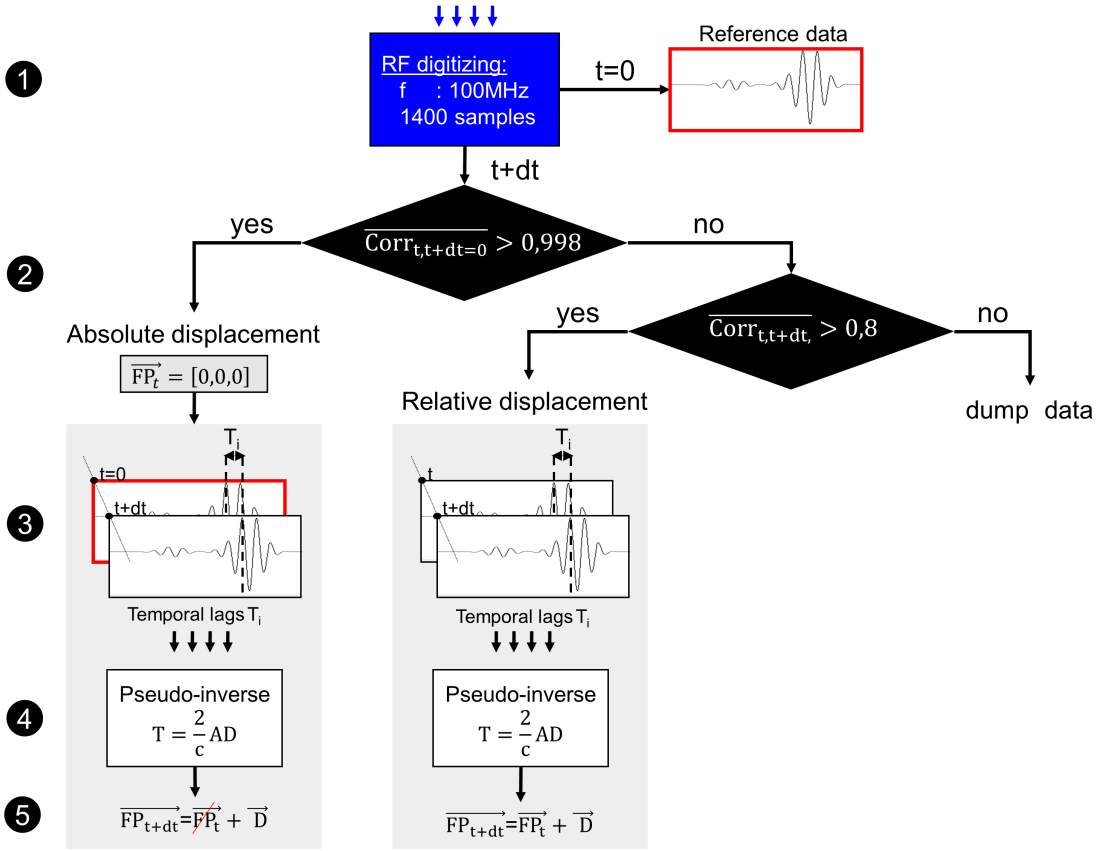

Figure 5.2: Displacement estimation pipeline.
1. Ultrasound signal acquisition was performed at 100 MHz and 1400 samples were acquired. The first acquisition (t=0) was taken as reference (red border US signals).
2. Decision tree: Absolute displacement (reset to initial position $\overrightarrow{FP_t}$=[0 0 0]) was made if cross-correlation of the current and reference data ($\overline{Corr_{t=0,t+dt}}$) was greater than 0.998 (in vitro). Otherwise if cross-correlation $\overline{Corr_{t,t+dt}}$ was greater than 0.8 a relative displacement between t and t+dt was performed. In the other case current data is dumped to prevent a bad displacement estimation.
3. Computation of cross-correlations and extraction of temporal lags Ti.
4. Computation of the displacement $\vec{D}$ in ($\vec{x}$,$\vec{y}$,$\vec{z}$) by solving a pseudo-inverse problem (see equation [1]).
5. Update of the current focus position $\overrightarrow{FP_{t+dt}}$.

After the pulse-echo for displacement estimation (total duration of 18 ms), a second HIFU pulse was emitted to induce tissue heating until a new displacement estimation was performed (see Figure 5.2). Electronic steering was updated according to the displacement estimation by uploading phase values to the HIFU generator (19 ms) and acoustic power was corrected to compensate for power losses inherent from electronic steering, using previously mentioned attenuation factors in each direction. The 3D position was determined from a synchronized push for all sub-apertures and each US-signals were recorded on the four channels simultaneously. This differs from the initial solution proposed by Pernot et al. [13] in which each position was determined sequentially through consecutive pulse-echo measurements for each individual sub-aperture. With this implementation and available hardware, the 3D motion estimation could be performed up to 25 times per sec-

ond. US signals, 3D positions, velocities and correlation coefficients were computed and continuously displayed in real-time on a Matlab™ plot (see Figure 5.3).

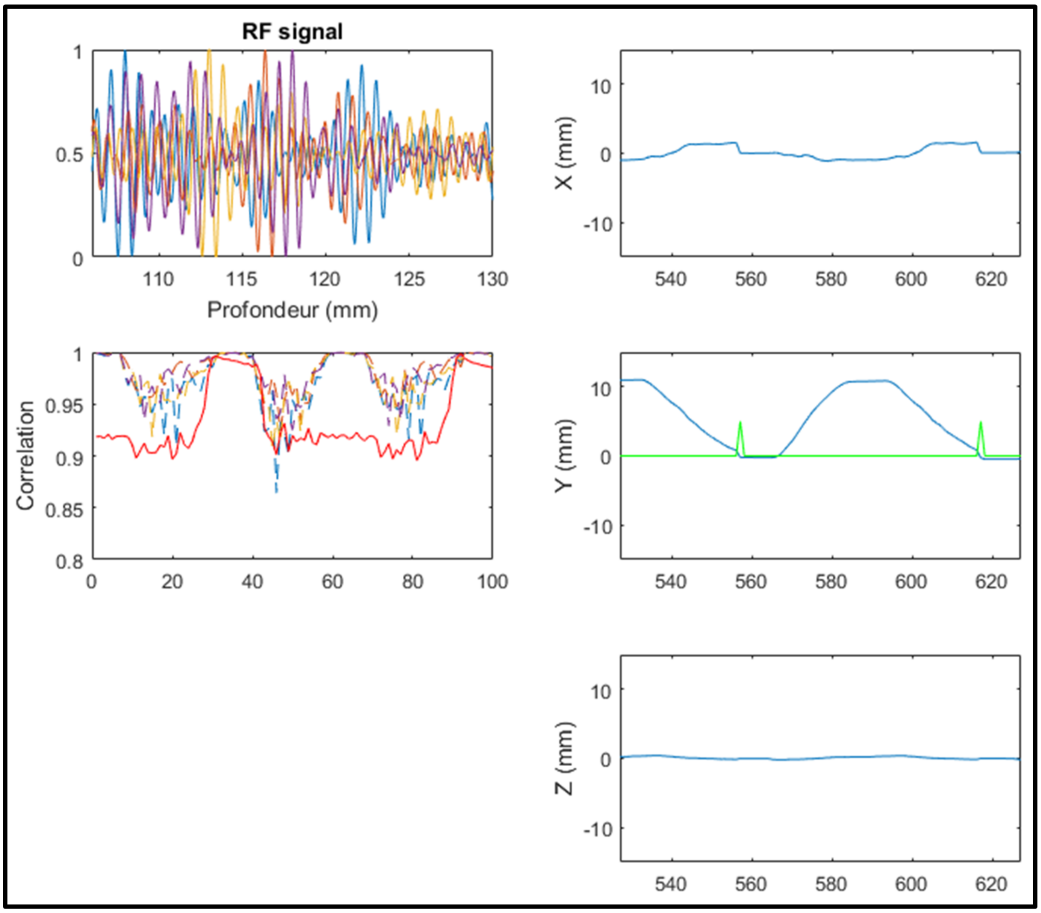

Figure 5.3: Screen capture of the real-time monitoring interface. a. Real-time monitoring of US signal backscattered from the tissue for the four sub-apertures. b. Real-time monitoring of the cross-correlation for each sub-apertures (dashed lines) and red curve shows the cross-correlation between current and the reference data ($\overline{Corr_{t=0,t+dt}}$) c. Displacement estimations in ($\vec{x}$,$\vec{y}$,$\vec{z}$) and the green curve depicts the reset of the position (see Figure 5.2) .

5.2.2 MR acquisition and reconstruction pipeline

MR-Thermometry was performed on a 1.5T scanner (Siemens Aera, Erlangen, Germany) using a single-shot echo-planar imaging sequence with GRAPPA acceleration factor of 2. This sequence integrated a crossed-pair navigator used to correlate the displacement estimations with an absolute displacement measurement. Navigator was positioned along the y-axis in the transducer geometry were motion was the most significant. During in vitro experiments, three slices were acquired in coronal orientation with the following parameters: FOV = 180x168 mm^2, TR/TE/FA = 166 ms/14 ms/32°, voxel size = 2x2x5 mm^3, with a bandwidth of 1650 Hz per pixel. For in vivo experiments, five slices were acquired: FOV = 224x224 mm^2, TR/TE/FA = 140 ms/14 ms/45°, voxel size = 2x2x5

mm^3, partial Fourier 6/8, with a bandwidth of 1860 Hz per pixel.

Temperature image reconstruction was performed on the open source Gadgetron framework [19]. Magnitudes and phase images were processed in real-time in a previously described thermometry pipeline [20] developed for cardiac thermometry:

1. The first twenty magnitudes images in the time series were used to find the image corresponding to the central position within the displacement range. This image was used as a reference frame for the registration.

2. The following magnitude images were registered using optical flow algorithm. For in vitro experiments a rigid motion algorithm was used, whereas a Black-Anandan algorithm (implemented on graphic card) was used for in vivo experiments to account for liver deformations during breathing.

3. A principal component analysis method was performed on the first thirty frames to build a phase model (synthetic phase image) freed from susceptibility artifact induced by motion.

4. Temperature maps were computed using the PRFS method after fifty frames (25 s in vitro and 35 s in vivo) of learning step. The current temperature increase T_i was computed as

$$T_i = \frac{\phi_i - \phi_{ref}}{\gamma.\alpha.B_0.TE}$$

Where ϕ_i is the current synthetic phase and ϕ_{ref} is a reference phase taken as the first synthetic phase of the interventional step. γ = 267.5 rad.s^{-1}.T^{-1} is the gyromagnetic ratio, α = -0.0094 ppm.°C^{-1} is the PRF temperature coefficient, B_0 = 1.5 T is the static magnetic field strength and TE is the echo time.

The potential improvement of the 3D US based beam steering was analyzed on the temperature images. The pixel displaying the maximal temperature increase in the sonicated area was selected and temperature profile in y direction was plotted. The full width at half maximum (FWHM) was computed and compared with and without motion compensation.

5.2.3 Evaluation platform

A gel phantom composed of 3 % agar and 2 % silica was positioned in a plastic box inside a water tank (see Figure 3a). Silica (Particle size < 14 nm, Aldrich, USA) is aimed

to have Rayleigh scattering effects (14 nm $< \lambda$=1.6 mm) in order to mimic the speckle observed in tissues. Mylar membranes (50 mum thick, smaller than 1/30 of the ultrasonic wavelength) were glued to the base of the plastic box and water tank to ensure ultrasound wave propagation from the transducer toward the phantom. A rotary motor was used to generate a translation of the sample on y-axis using rod and slides. Variations of the voltage imposed at the motor's dipole allowed tuning of the frequency of the sinusoidal displacement and thus to change the maximal velocity. Typical settings of the motion were amplitudes 10 mm and maximum velocities ranged between 1.0 to 1.5 mm.s^{-1}. MR data was acquired using two 32-element imaging coil arrays positioned laterally to the water box and a 19 cm loop coil was positioned above the phantom to improve coil coverage and maximize signal to noise of the MR-images. A first batch of experiments were conducted to setup the displacement monitoring method and integrate it into the thermometry pipeline. After adjustments, this study reports five ablations in vitro, with and without focus correction.

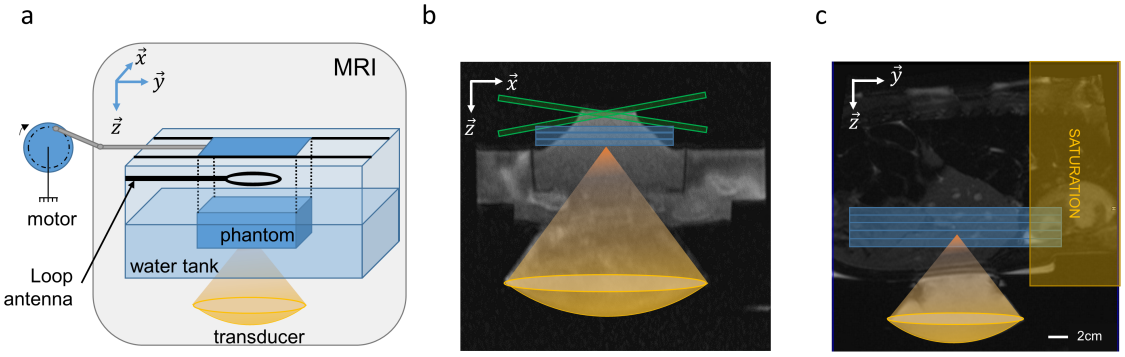

Figure 5.4: In vitro and in vivo validation. a: The rotation of a motor is converted into a 1D translation along y-axis, using a rod and slides. The phantom is maintained above the transducer using a plastic box with a Mylar membrane glued at the bottom to allow propagation of the ultrasound beam. Typical motion settings were 10 mm of amplitudes and maximum velocities of 10 mm.s-1. Three coronal slices were acquired to monitor MR-thermometry. b: Transverse ((x, z) plane in the transducer's frame of reference) anatomical image of the setup. Blue box represent three slices in coronal orientation and green box represent the crossed pair navigator position. c: Anatomical image and animal positioning. Blue box represent five MR-temperature slices positioned in coronal orientation. A saturation slab (yellow box) was positioned on top of the hepatic dome to suppress signal from the heart on the images.

5.2.4 In vivo study

In vivo validation was performed in the livers of two pigs (Large White x Landrace, $\sim$ 40 kg). In total, N=8 ablations in vivo have been performed. The protocol was approved by the local Ethics Committee according to the European rules for animal experimentation. Premedication of pigs were performed by an intramuscular injection of

a mix ketamine (20 mg.kg^{-1}), acepromazine (1 mg.kg^{-1}) and buprenorphine (10 μg.kg^{-1}). Animal anesthesia was induced with intravenous injection of propofol (1.5-2 mg.kg^{-1}) and maintained using 2 % of Isoflurane mixed with the appropriate air/oxygen supply (50/50) after intratracheal intubation. The heart rate and arterial pressure were recorded and monitored continuously. The animal was installed in prone position on top of the HIFU platform and positioned at the magnet isocenter. The animal was continuously cared for by veterinary staff. MR-data was acquired using two 32-element imaging coil arrays positioned laterally to the thorax and a 19 cm loop coil was positioned underneath the animal on top of the HIFU transducer. After completion of the treatment, the animal was euthanized with an intravenous injection of Dolethal (Vetoquinol, Lure, France), until complete cardiac arrest was attested from the ECG trace.

5.2.5 Navigator feedback and slice following

A TCP connection was implemented in the sequence in order to communicate with our remote computer where the motion correction was performed. This connection was bidirectional: the MRI send the current position of the echo navigator and receive the 3D position found by our 3D motion estimation algorithm.

On the remote computer: the navigator feedback was used to compare the displacement estimation to a absolute measurement.

On the scanner: the reception of the 3D position allowed to freeze the motion by updating the position of the slices on-the-fly. Direct estimation of the quality of the motion correction was thus possible.

Some ticks were necessary to make this connection possible while avoiding to slave the sequence on 3D motion estimation algorithm or vice versa. It consisted to implement a TCP connection with two buffers on the remote computer side (see Figure 5.5).

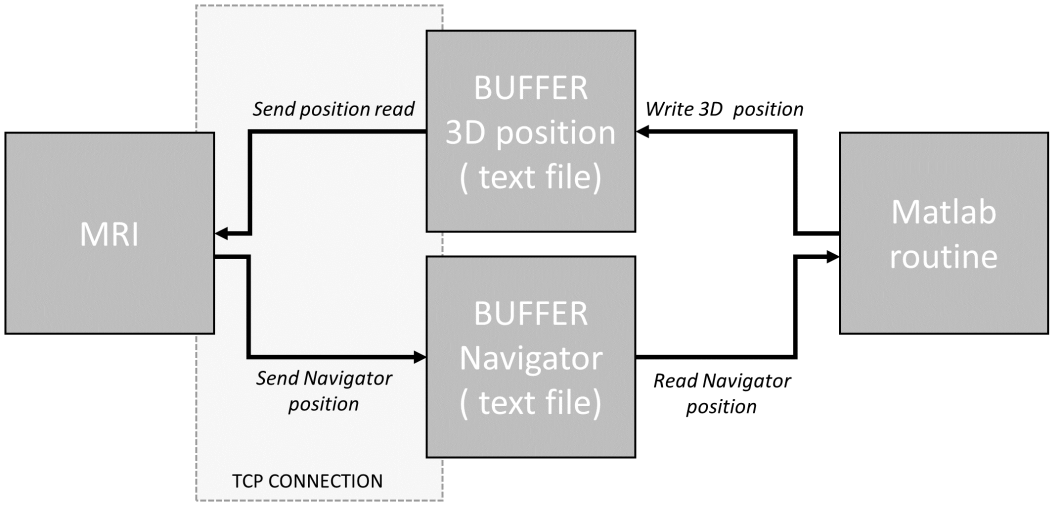

Figure 5.5: Schematic representation of remote computer and MRI communication.

5.3 Results

The thermometry pipeline allowed to retrieve temperature maps with a total computation time around 100 ms/slice, for an image size of 140x140 pixels. This processing pipeline is thus compatible with real-time conditions, with minimal latency. No interference of the 3D motion estimation pipeline could be identified on the MR-images. Very limited radiofrequency interferences (the maximal number of discarded signals during 120 s monitoring was 3 over 1200 measurements, with most of the experiments showing 0 or 1 occurrence) were observed on the recorded backscattered signals from ultrasound pulse-echo system when the MRI thermometry sequence was running.

Figure 5.4a shows the timings for the 3D motion correction pipeline. US data computation time and update of phases of the ultrasound transducers lasted 18 ms and 19 ms, respectively. This leads to the main source of HIFU sonication time loss, resulting in a 63 % of duty cycle for a motion correction update rate of 10 Hz. Such a refresh rate was considered sufficient to monitor liver displacement while maintaining a reasonable sonication duty cycle.

5.3.1 In vitro

Figure 5.7b shows the 3D displacement monitored using speckle-tracking in the transducer geometry. The maximum displacement and velocity were 12 mm and 11 mm.s^{-}1, respectively. The MR-navigator signal amplitude (Figure 5.7a) was in good agreement with the proposed method (y-axis on Figure 5.7). Cross-correlation coefficients between current and previous US-acquisition, along time, for all sub-apertures, remained above

0.94 (see Figure 5.7b). Not surprisingly, minimum cross-correlation was found when the absolute velocity was maximum (see black arrows on Figure 5.7b). The mean correlation on each sub-aperture between the reference and current US-acquisition ($\overline{Corr_{t=0,t+dt}}$) , is displayed in red on the bottom graph of Figure 5.7. Above the threshold (dashed line) a reset of the position based on an absolute displacement estimation was performed (see Figure 5.2). Using this approach, the reset of the position was found robust on every in vitro experiments (N = 5).

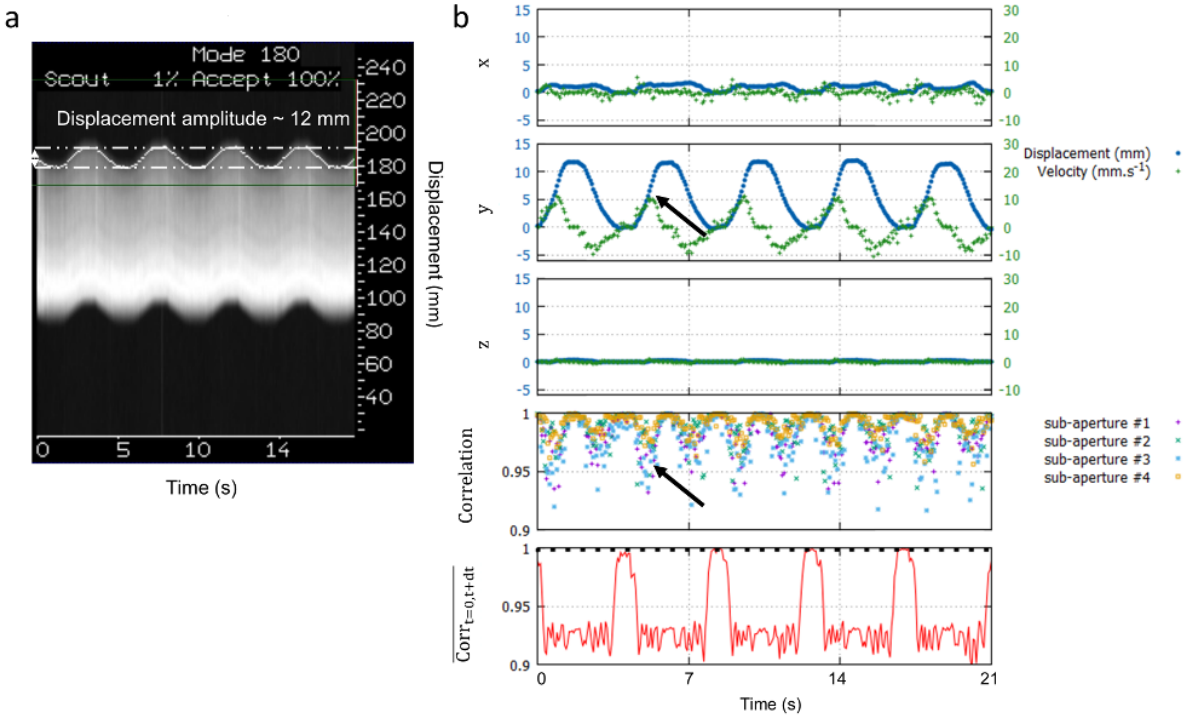

Figure 5.6: Displacement estimation validation in vitro. a: Navigator signal positioned along the y-axis acquired during 20 s. b: Representative displacement estimations in ($\vec{x}$,$\vec{y}$,$\vec{z}$) obtained in vitro using our experimental settings. The blue and green curves represent the displacement estimations and the corresponding instantaneous speed computed from estimated positions, respectively. The bottom graph displays the cross-correlations between two successive US acquisitions along time, for each sub-apertures. Black arrows depict lower cross-correlation coefficients during peak velocities. On the bottom graph, the red curve represents the mean correlation between current measurement and the first acquisition taken as reference. The black dashed line represents the threshold above which absolute displacement estimations in performed to reset the position. s.

Figure 5.9a shows a screen capture of temperature map for the three slices, after 60 s of sonication at 150 W acoustic power. Without motion correction of the focus, the temperature footprint was lengthened mainly in the y-direction where the displacement was the most important. With 3D us-based motion correction the temperature rise remained very localized. The temporal evolution of the maximum temperature increase is displayed on Figure 5.9b. It reached 18 °C and 26 °C without and with motion compensation, respectively. The temperature standard deviation on this pixel measured prior to

sonication was 1.2 °C. These improvements of heating efficiency were observed for each in vitro experiments (N = 5). Overall, maximum temperature increases were improved by 38 *pm* 5 %. The FWHM of the temperature profiles along the y direction were 18 mm and 6 mm without and with HIFU beam steering, respectively (see Figure 5.9c).

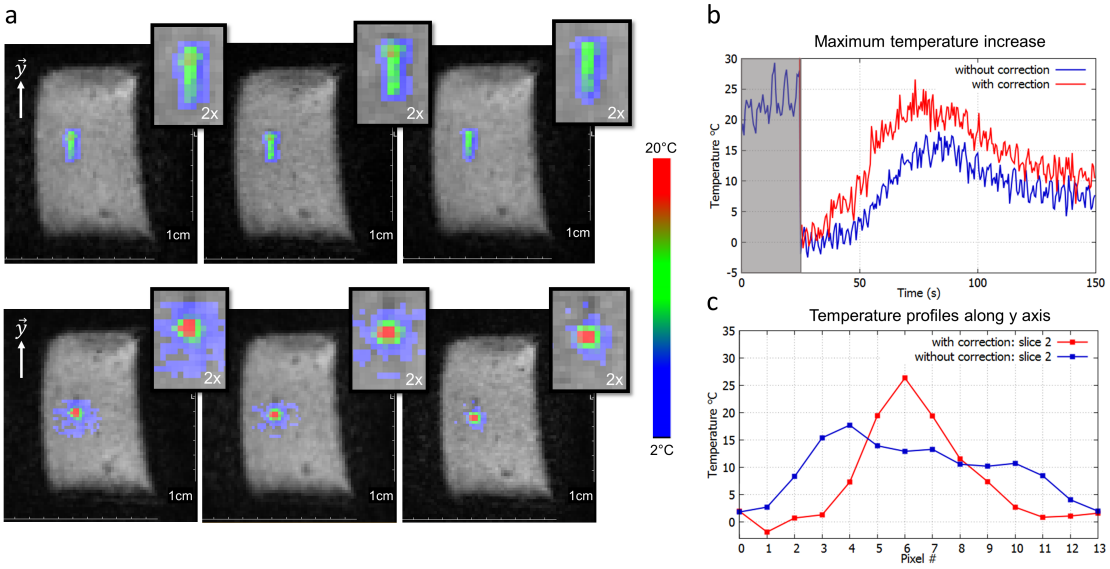

Figure 5.7: Representative in vitro MR-Thermometry. a: Shows temperature images overlaid to magnitude images, taken at the end of HIFU sonication, without (top) and with (bottom) 3D focus position update. b: Shows the temperature temporal evolution of the pixel experiencing the maximum temperature increase, for both conditions. The 50 first dynamic acquisitions (gray box) corresponded to the learning step in the thermometry pipeline and were used for correction of motion and associated susceptibility artifacts of temperature images. c: shows the temperature profiles along the y-axis crossing the pixel with maximal temperature increase, at the end of sonication, for both conditions.

5.3.2 In vivo

Displacement could also be successfully monitored in vivo in the liver of pig during N = 8 ablations. Figure 6b shows displacement in ($\vec{x}$,$\vec{y}$,$\vec{z}$) . The maximum displacement and peak velocity were 10 mm and 11 mm.s-1, respectively. MR-navigator signal amplitude (Figure 5.8) was in agreement with the motion displacement estimated on y-axis. Compared to the in vitro experiments, cross-correlation coefficients along time, were lower but remained above 0.85 (see Figure 5.8b). In vivo ($\overline{Corr_{t=0,t+dt}}$) was a robust metric to reset the position to its initial position, for each respiratory cycle.

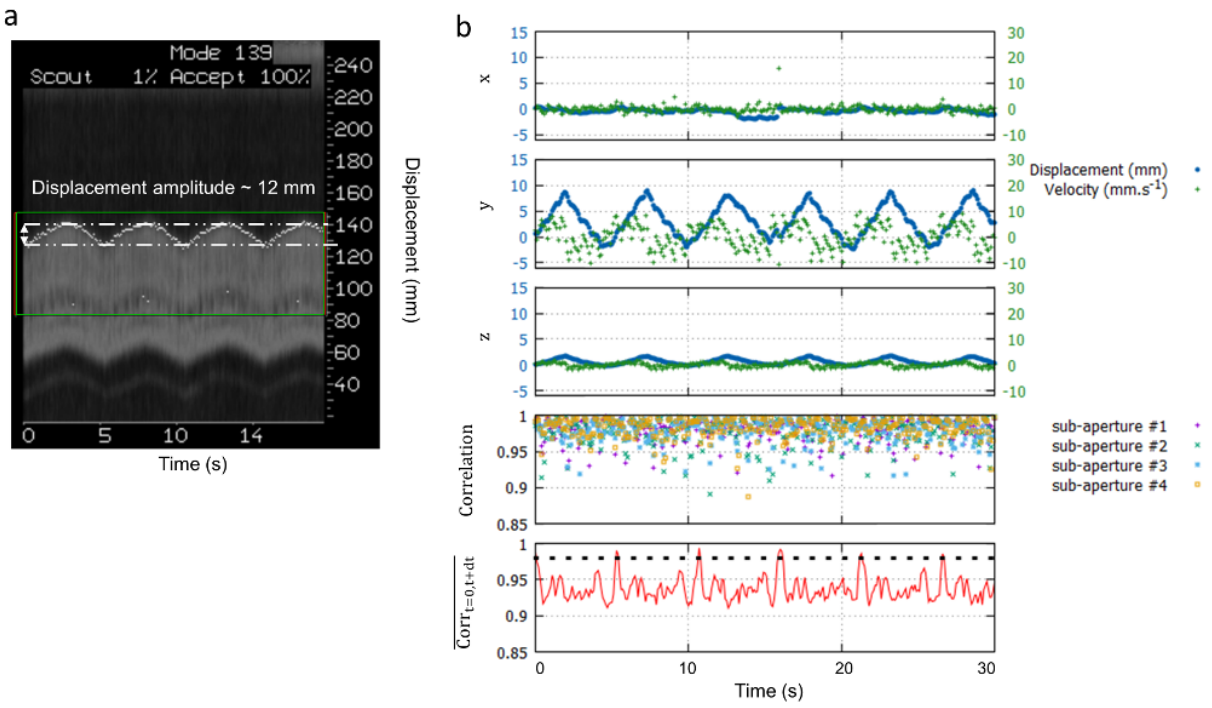

Figure 5.8: Displacement estimation in vivo on pig liver. a: Navigator signal positioned along the y-axis acquired during 20 s. b: Representative displacement estimations in $(\vec{x},\vec{y},\vec{z})$ obtained during in vivo experiment on liver. The blue and green curves represent the displacement estimations and the corresponding instantaneous speed computed from estimated positions, respectively. The bottom graph displays the cross-correlations between two successive US acquisitions along time, for each sub-apertures. The red curve displays the mean correlation between current and the first acquisition taken as reference. The black dashed line represents the threshold above which absolute displacement estimations in performed to reset the position.

Figure 5.9a shows a screen capture of temperature map after 40 s of sonication at 450 W acoustic power. The temperature footprint at the focal spot, with and without focus correction were close to each other. However, we can note a slightly lengthening in the y-axis along the principal motion axis without focus correction. Conversely, with motion correction the focal spot conserved its point like shape. The maximal temperature, on the five slices, was displayed over time on Figure 5.9b. The maximum temperature increase was 18 °C and 27 °C without and with focus correction, respectively. The temperature standard deviation on this pixel prior to ablation was 0.9 °C. Similarly to in vitro experiments, in vivo temperature increases (N = 8) were improved by 34 ± 9 %.

Figure 5.9c displays temperature profiles on y axis for both conditions. The FWHM of the temperature profiles along the y direction were 13 mm and 9.5 mm without and with HIFU beam steering, respectively. The FWHM in the x direction (data not shown) were 12 and 8 mm, respectively.

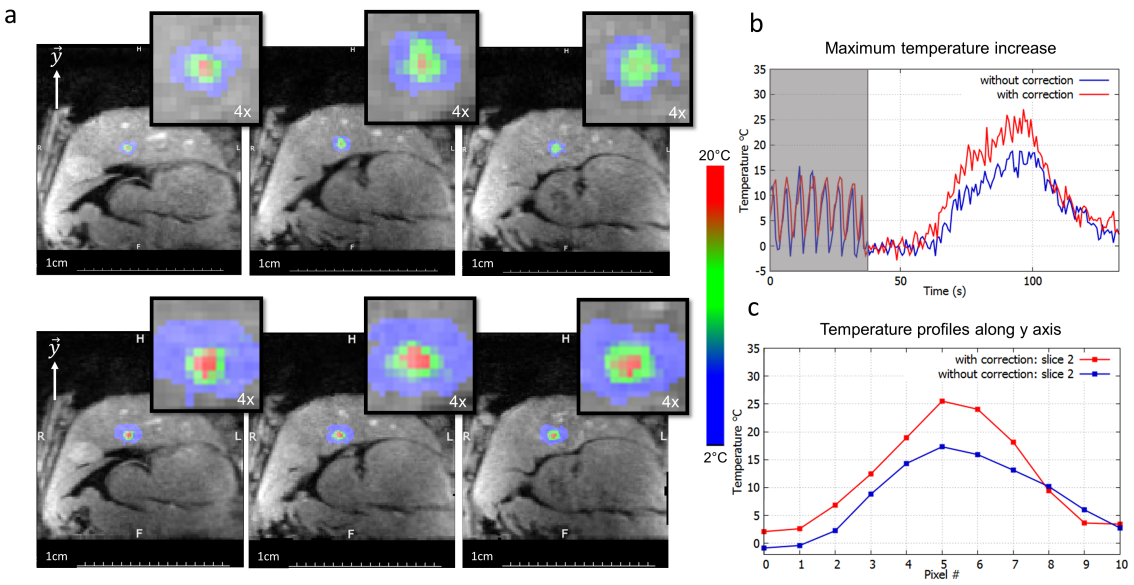

Figure 5.9: Representative in vivo MR-Thermometry. a: Screen capture of representative temperature images overlaid to magnitude image, taken at the end of HIFU sonication, without (top) and with (bottom) focus update. b: Shows the temperature evolution of the pixel experiencing the maximum temperature increase, along time, for both conditions. The 50 first dynamic acquisitions (gray box) corresponded to the learning step in the thermometry pipeline (see material and methods for details). c: shows the temperature profile along the axis crossing the pixel with maximal temperature increase at the end of sonication, for both conditions.

5.4 Discussion

This study shows that the proposed 3D ultrasound-based motion correction approach allows maintaining the HIFU focal spot in the presence of motion without adding any burden or complexity to MR thermal imaging.Thus, treatment efficiency on mobile organs can be improved while reducing risks of overheating of tissues located in the near field of the HIFU beam. Simultaneous 3D rapid MR-thermometry provided precise monitoring of temperature distribution at the focus and in surrounding areas, allowing online safety assessment of the therapeutic procedure, which is mandatory in perspective of clinical application.The 3D speckle-tracking method required only 4 elements over 256 of the HIFU transducer to operate in reception, resulting in a negligible loss in maximal available acoustic power. Only few US signals from back scattered ultrasound were affected by electro-magnetic radiofrequency signals from the MRI sequence. However, the US signal envelope was preserved and no error was induced on displacement estimations. Thus, no constraint was imposed on MRI sequence timings with respect to displacement estimations or vice-versa, allowing HIFU and MRI to operate asynchronously. This provides the operator full flexibility for adjusting MRI sequence parameters according to the desired priority, including spatial resolution, volume coverage, update rate or effective signal

to noise ratio. In the present work, we chose to acquire 5 slices every 0.7 s in vivo with an in-plane spatial resolution of 2 mm using a single-shot EPI acquisition. Higher spatial resolution (1 mm in-plane) was reported in the liver of pig using a segmented EPI acquisition, at the cost of a much slower imaging update rate (2.1 s/slice) [21].

3D ultrasound-based HIFU beam steering was successfully evaluated on a phantom and in vivo in the liver of pig. Estimation of 3D position from a simultaneous measurement of the 4 sub-apertures was found robust and did not require sequential measurements for each sub-aperture, as proposed initially in Pernot et al. [13] Compared to other autonomous methods (e.g. 2D ultrasound imaging), this method does not require any additional device to be operated inside the magnetic bore. The 3D motion correction system was able to compensate typical respiratory motion. These values are similar to physiological measurements reported in the literature [4], showing direct practical applicability of this method for clinical application. 3D speckle motion tracking relies on the spatio-temporal correlations of ultrasound speckle measured consecutively. Compared to in vitro, in vivo temporal correlation coefficients were found lower. These results can be attributed to attenuation of the back-scattered US-signal, inherent to heterogeneities of the liver (lobes, blood vessels) and presence of other anatomical structures (skin, fat layer) in the HIFU beam path. Besides, the in vivo density and homogeneity of the ultrasound speckle may differ from in vitro experiments. Other parameters such as the transducers sensitivity in reception and their operating frequency can play a predominant role in the overall quality of the displacement estimation. However, 3D tracking results were found satisfactory with the available hardware and technical implementation.

US signals were acquired upstream from the focus to limit displacement estimation errors due to speed of sound variations during temperature increase. For in vivo ablations, the footprint of temperature rise in the direction of motion appeared less visible on temperature images (Figure 5.7a) than for in vitro experiments (Figure 5.8a). The presence of perfusion in the liver is expected to evacuate heat more efficiently than in the gel, making observation of moderate temperature increase outside of the focal spot position more difficult. Moreover, thermal diffusivity also differs in the liver, which may explain that temperature spot dimensions were larger than in the gel. However, the FWHM was systematically reduced in vivo with motion compensation and showed comparable values in x and y directions (8 mm vs 9.5 mm), whose difference remained lower than the pixel size of the temperature image (2 mm). As a result of spatially reduced temperature spread, the maximal temperature was increased by approximately 35% in vitro

and in vivo, confirming that the correction substantially improved focalization of acoustic energy for better heating efficiency.

In vitro and in vivo, an MR-navigator echo was aligned with the main axis of displacement, allowing to correlate its values with those estimated by ultrasound measurements. In vitro, only rigid motion was present and MR-navigator positions were very close to the 3D estimations on the y-axis. However for the in vivo case, some differences were observed between MR-navigator readings and displacement estimated from ultrasound. Although maximal amplitudes of displacement were similar, the shape of displacement was slightly different. However, the MR-navigator was positioned at the dome of the liver (liver/lung interface), whereas HIFU sonication were performed at the inferior part of the liver. Thus, readings from the 1D MR-navigator echoes can hardly reflect the effective liver deformation at this position during the different breathing states. Thereby, the proposed approach appears more robust as compared to MR-navigator-based motion estimation since it evaluates local displacements near the targeted region to be treated. Another advantage of the method is that motion of the target is directly computed in the transducer's frame of reference and does not require computations between different frames of coordinates. In this study MR-acquisition slices were positioned from anatomical images to cover the region being sonicated. Thus, potential out-of-slice motion may appear when the stack of slices is not aligned with the direction of motion, which could introduce small oscillations in MR-temperature readings. Although these effects were not experimentally observed in our experiments (maximal displacement measured by ultrasound in x and z axes remained below 3 mm – see Figure 5.8b and Figure 5.8b), refinement of the method may include automatic slice repositioning from the 3D ultrasound position. Another option would be to run ultrasound pulse-echo over several respiratory cycles and to compute optimal slice orientation to minimize out-of-slice motion in order to optimize temperature mapping precision around the targeted region.

Despite the positive results reported in this study, the current implementation suffers from several limitations. First, the loss in sonication duty cycle is due to the 18 ms delay to process the RF data and estimate the displacement (cross-correlations, pseudo-inverse) and to the additional 19 ms delay to update the phase law of our 256 elements generator. These delays could easily be reduced using optimized electronic device and using more rapid implementation of the displacement estimation algorithm. Second, the current implementation does not allow arbitrary selection of the transducer elements operating in reception. Thus, in perspective of transcostal liver ablation [22, 23] some transducer may

be located in front of a rib, making determination of liver position impossible. Again, this limitation could be circumvented by appropriate electronics, with all US channels operating in transmit/receive mode.

5.5 Conclusion

In this study we have validated a 3D ultrasound based motion tracking along with real-time MR-temperature monitoring. Focus position was successfully corrected in vivo in the liver of pigs for typical respiratory motion amplitudes and maximum velocities of 10 mm and 10 mm.s^{-1}, respectively. After focus position correction the heating effectiveness was improved by approximately 35 % in vitro and in vivo. Hardware and software optimization may provide higher frame rate for motion determination and compensation in 3D.

5.6 Perspectives

3D ultrasound based motion correction of the focus position, implemented in this study is suited for respiratory motions and thus for applications on abdominal organs. However, such a method could be of particular interest for therapeutic treatment on the heart using ultrasounds. As introduced in Chapter 1, two applications of ultrasounds on the heart could benefit from displacement monitoring and real-time correction of the focus position.

Continuous pacing under free breathing conditions. This application wont require an additional shot to improve the sonication duty cycle, as presented in the study. Hence, a displacement estimation framerate of 25 Hz could be achieved, which should provide better correlation and thus better displacement estimations, between successive US-acquisitions.

Cardiac ablation. For this application, the framerate of displacement estimation will be limited ($\sim$ 10 Hz) by the additional HIFU sonication used to induce a thermal necrosis. Further studies should investigate whether this low refresh rate is sufficient to correct effectively the position of the focus on the heart.

In any case, for both applications, the implementation of this method on the heart will be challenging as it combines several constrains. 1) cardiac motion is by far, more complex than respiratory motion. 2) cardiac walls are relatively thin ($<$ 3-5 cm), and

extraction of the displacement information from the back scattered signals may be harder to achieve. In addition, blood flow may be a possible source of displacement estimation errors. 3) Only limited acoustic apertures are available to reach de heart, due to lungs and the ribs cage. In our study the four elements in receive mode were chosen at the four corners of the transducer, resulting on a good projection of the normal vectors a_i on x, y and z . These projections may be dramatically reduced for other ultrasound probe designs. As a consequence, it will increase the crosstalk between sub-apertures, which will ultimately decrease the sensitivity of the motion estimation.

5.7 References

[1] Daniel Coluccia et al. "First noninvasive thermal ablation of a brain tumor with MR-guided focused ultrasound". In: *J Ther Ultrasound* (2014).

[2] David Gianfelice et al. "Palliative Treatment of Painful Bone Metastases with MR Imaging–guided Focused Ultrasound 1". In: *Radiology* (2008).

[3] Eric J. Dorenberg et al. "Volumetric ablation of uterine fibroids using Sonalleve high-intensity focused ultrasound in a 3 Tesla scanner – first clinical assessment". In: *Minimally Invasive Therapy & Allied Technologies* (July 2012).

[4] S. C. Davies et al. "Ultrasound quantitation of respiratory organ motion in the upper abdomen". In: *The British journal of radiology* (1994).

[5] W. Apoutou N'Djin et al. "An ultrasound image-based dynamic fusion modeling method for predicting the quantitative impact of in vivo liver motion on intraoperative HIFU therapies: Investigations in a porcine model". In: *PloS one* (2015).

[6] M. de Greef et al. "Intercostal high intensity focused ultrasound for liver ablation: The influence of beam shaping on sonication efficacy and near-field risks". In: *Medical physics* (2015).

[7] Andrew B. Holbrook et al. "Respiration based steering for high intensity focused ultrasound liver ablation: Respiration Guided MRgFUS in the Liver". en. In: *Magnetic Resonance in Medicine* (Feb. 2014).

[8] B. D. de Senneville et al. "MR-Guided Thermotherapy of Abdominal Organs Using a Robust PCA-Based Motion Descriptor". In: *IEEE Transactions on Medical Imaging* (Nov. 2011).

[9] Zarko Celicanin et al. “Real-time method for motion-compensated MR thermometry and MRgHIFU treatment in abdominal organs: MRgHIFU Treatment Method in Abdominal Organs”. en. In: *Magnetic Resonance in Medicine* (Oct. 2014).

[10] Mario Ries et al. “Real-time 3D target tracking in MRI guided focused ultrasound ablations in moving tissues”. en. In: *Magnetic Resonance in Medicine* (Dec. 2010).

[11] Philippe Lourenço de Oliveira et al. “Rapid motion correction in MR-guided high-intensity focused ultrasound heating using real-time ultrasound echo information”. en. In: *NMR in Biomedicine* (Nov. 2010).

[12] *(ISMRM 2014) Catheter-mounted expandable loop (CAMEL) balloon RF coil for high-resolution intracardiac MR imaging.*

[13] Mathieu Pernot et al. “3-D real-time motion correction in high-intensity focused ultrasound therapy”. en. In: *Ultrasound in Medicine & Biology* (Sept. 2004).

[14] F Marquet et al. “Optimal transcostal high-intensity focused ultrasound with combined real-time 3D movement tracking and correction”. In: *Physics in Medicine and Biology* (Nov. 2011).

[15] J.W. Wijlemans et al. “Magnetic resonance-guided high-intensity focused ultrasound (MR-HIFU) ablation of liver tumours”. In: *Cancer Imaging* (2012).

[16] G. Nabi et al. “High intensity focused ultrasound treatment of small renal masses: Clinical effectiveness and technological advances”. In: *Indian Journal of Urology : IJU : Journal of the Urological Society of India* (2010).

[17] Solenn Toupin et al. “Feasibility of real-time MR thermal dose mapping for predicting radiofrequency ablation outcome in the myocardium in vivo”. In: *Journal of Cardiovascular Magnetic Resonance* (Jan. 2017).

[18] Robert D. Peters and R. Mark Henkelman. “Proton-resonance frequency shift MR thermometry is affected by changes in the electrical conductivity of tissue”. In: *Magnetic resonance in medicine* (2000).

[19] Michael Schacht Hansen and Thomas Sangild Sørensen. “Gadgetron: An open source framework for medical image reconstruction”. en. In: *Magnetic Resonance in Medicine* (2013).

[20] Valéry Ozenne et al. “Improved cardiac magnetic resonance thermometry and dosimetry for monitoring lesion formation during catheter ablation”. In: *Magnetic resonance in medicine* (2017).

[21] Vincent Auboiroux et al. “Respiratory-Gated MRgHIFU in Upper Abdomen Using an MR-Compatible In-Bore Digital Camera”. en. In: *BioMed Research International* (2014).

[22] Fabrice Marquet et al. “Noninvasive, Transient and Selective Blood-Brain Barrier Opening in Non-Human Primates In Vivo”. en. In: *PLoS ONE* (July 2011). Ed. by Martin W. Brechbiel.

[23] Bruno Quesson et al. “A method for MRI guidance of intercostal high intensity focused ultrasound ablation in the liver”. In: *Medical Physics* (2010).

CHAPTER 6

General conclusion and perspectives

The treatment of the heart using HIFU is a major technological challenge. Ultimately it could have a real impact on the improvement of patient treatment for certain cardiac diseases. Prior to clinical translation, two well-known limitations of the application of HIFU, namely physiological motions and a limited acoustic window need to be addressed. Besides, monitoring of MRgHIFU procedures (ie. MR-thermometry and/or MR-ARFI) on the heart is also non-trivial and requires several image corrections.

During this thesis work, we have identified and explored two potential applications of therapeutic ultrasounds using fully non-invasive approaches. Firstly cardiac ablations in case of arrhythmia and secondly, cardiac stimulation in case of bradycardia or asystoly.

The first study has demonstrated the relevance of non-invasive pacing for therapeutic purposes. The study has allowed to identify the requirements in terms of acoustic pressures and its efficacy under controlled conditions. In addition, we have identified two biomarkers of interests to be monitored during the procedure (ie. MR-ARFI and PCD). However, for in vivo experiments injunctions of micro-bubbles were compulsory to overcome the reduced acoustic power at the focus. Hence, before confirmation of the clinical applicability of non-invasive stimulations, further investigations would be required. They encompass, the optimization of the ultrasound emission frequency, the design of a second generation ultrasound probe and a more in-depth safety study.

In a second step, we have validated a new monitoring method that proposed to monitor, with a high temporal resolution, the temperature and the displacement evolution along the MRgHIFU procedure. This study was validated during ablation. We have investigated the displacement amplitude as a qualitative surrogate for tissue elasticity variation and found that as the lethal thermal dose was reached, the displacement amplitude decreased by around 25 %. This decrease was attributed to an increase in tissue stiffness as the lesion was forming. The validation was performed on static organs, however it has a clear relevance for cardiac ablations and for cardiac stimulations, under MRI.

On the one hand, it could provide the focus position localization and stiffness change information during cardiac ablations and on the other hand, it could be of particular interest for safety assessment during cardiac stimulations.

In perspective of MRgHIFU procedures on mobile organs, the second development has investigated a standalone, ultrasound based, motion correction of the focus position. This method exploited the temporal shift of backscattered signals during displacement and was combined with MR-thermometry to assess the correction quality. Results have shown a complete compensation of the motion artifact on the temperature footprint, for respiratory motion with an improvement of the thermal therapy of 35 %. As of now, the feasibility of focus position correction for cardiac motion was not performed. Once validated, it could provide a way to correct the focus position and improve HIFU cardiac ablations or lock the focus on a desired localization of the heart in the context of cardiac stimulation.

Despite the clear interest of the two aforementioned methods for cardiac applications of therapeutic ultrasounds, their validations on the heart was not possible in the timescale of this work thesis. One of the main limitation was the design of our HIFU device which was not able to deliver sufficient acoustic power in the heart. For simultaneous temperature and displacement monitoring, necessary refinements of the method have been identified and solutions have been proposed (i.e magnetic susceptibility artifact and motion corrections).

Publications

Peer-reviewed journal papers

1. Pierre Bour, Fabrice Marquet, Valéry Ozenne, Solenn Toupin, Erik Dumont, Jean-François Aubry, Matthieu Lepetit-Coiffe, and Bruno Quesson. "Real-time monitoring of tissue displacement and temperature changes during MR-guided high intensity focused ultrasound". In: *Magnetic Resonance in Medicine* (2017)

2. Solenn Toupin, Pierre Bour, Matthieu Lepetit-Coiffé, Valéry Ozenne, Baudouin Denis de Senneville, Rainer Schneider, Alexis Vaussy, Arnaud Chaumeil, Hubert Cochet, Frédéric Sacher, Pierre Jaïs, and Bruno Quesson. "Feasibility of real-time MR thermal dose mapping for predicting radiofrequency ablation outcome in the myocardium in vivo". In: *Journal of Cardiovascular Magnetic Resonance* (Jan. 2017)

3. Valéry Ozenne, Solenn Toupin, Pierre Bour, Baudouin Denis de Senneville, Matthieu Lepetit-Coiffé, Manuel Boissenin, Jenny Benois-Pineau, Michael S. Hansen, Souheil J. Inati, Assaf Govari, et al. "Improved cardiac magnetic resonance thermometry and dosimetry for monitoring lesion formation during catheter ablation". In: *Magnetic resonance in medicine* (2017)

4. Fabrice Marquet, Pierre Bour, Fanny Vaillant, Sana Amraoui, Rémi Dubois, Philippe Ritter, Michel Haïssaguerre, Mélèze Hocini, Olivier Bernus, and Bruno Quesson. "Non-invasive cardiac pacing with image-guided focused ultrasound". In: *Scientific Reports* (Nov. 2016)

5. Fanny Vaillant, Julie Magat, Pierre Bour, Jérôme Naulin, David Benoist, Virginie Loyer, Delphine Vieillot, Louis Labrousse, Philippe Ritter, Olivier Bernus, Pierre Dos Santos, and Bruno Quesson. "Magnetic resonance-compatible model of isolated working heart from large animal for multimodal assessment of cardiac function, electrophysiology, and metabolism". en. In: *American Journal of Physiology - Heart and Circulatory Physiology* (May 2016)

6. V. Ozenne, S. Toupin, P. Bour, A. Emilien, F. Vaillant, B.D. de Senneville, P. Jaïs, E. Dumont, J. Benois-Pineau, P. Desbarats, and B. Quesson. "Magnetic Resonance

Imaging guided cardiac radiofrequency ablation". en. In: *IRBM* (Mar. 2015)

Under revision

1. Real-time 3D ultrasound based motion tracking for the treatment of mobile organs with MR-guided High Intensity Focused Ultrasound. *P.Bour, F.Marquet, V.Ozenne, B. Senneville, E. Dumont, B. Quesson, International Journal of Hyperthermia 2016*

In preparation

1. Feasibility of cavitation-guided non-invasive cardiac stimulation using focused ultrasound in pigs. *P.Bour, F.Marquet, F.Vaillant, S.Amraoui,V.Loyer, D.Vieillot, R.Dubois, P.Ritter, M.Haïssaguerre, M.Hocini, O.Bernus, B.Quesson*

6.1 Patents

1. Fabrice Marquet, Pierre Bour, Bruno Quesson, Fanny Vaillant, Remi Dubois, Universite de Bordeaux, Institut National De La Sante Et De La Recherche Medicale, and Centre Hospitalier Universitaire De Bordeaux. "Systeme de stimulation cardiaque ultrasonore focalise, dispositif portable et stimulation cardiaque, et methodes associees". Sept. 2015

2. Fabrice Marquet, Pierre Bour, Bruno Quesson, Fanny Vaillant, Universite de Bordeaux, Institut National De La Sante Et De La Recherche Medicale, and Centre Hospitalier Universitaire De Bordeaux. "Système pour l'ablation ou le contrôle d'une zone du coeur par ultrasons et méthodes associées". Sept. 2015

Oral presentations

1. Simultaneous monitoring of displacement and temperature during HIFU ablation. *P.Bour, F.Marquet, V.Ozenne, S.Toupin, M. Lepetit-Coiffé, J-F Aubry, E. Dumont, B. Quesson, IEE IUS 2016*

2. Non-invasive cardiac pacing using image-guided focused ultrasound ex vivo and

in vivo in pigs. P.Bour, *F.Marquet, F.Vaillant, S.Amraoui, R.Dubois, P.Ritter, M.Haïssaguerre, M.Hocini, O.Bernus, B.Quesson, ISTU 2016*

3. Non-invasive cardiac stimulation with MR guided HIFU, a rapid, cardiac triggered, MR-ARFI method for direct visualization of stimulation site and assessment of tissue stiffness. P.Bour, *F.Marquet, V.Ozenne, S.Toupin, M. Lepetit-Coiffé, E. Dumont, B. Quesson, ISMRM 2016*

4. Simultaneous monitoring of displacement and temperature during HIFU ablation. P.Bour, *F.Marquet, V.Ozenne, S.Toupin, M. Lepetit-Coiffé, J-F Aubry, E. Dumont, B. Quesson, ISMRM 2015*

Poster presentations

1. 3D ultrasound based motion tracking with MR-thermometry. P.Bour, *F.Marquet, V.Ozenne, B.Denis de Senneville, E.Dumont and B.Quesson, SFR TECSAN 2017.*

2. Non-invasive thermal ablation of the myocardium with MRI-guided High Intensity Focused Ultrasound on perfused heart from pig. P.Bour, *F.Marquet, F.Vaillant, E.Dumont, P.Ritter, P.Jaïs, M.Haïssaguerre, Bruno Quesson, ISHR european section 2015*

3. Simultaneous MR-ARFI and MR-Thermometry during HIFU ablation. P.Bour, *F.Marquet, V.Ozenne, S.Toupin, M. Lepetit-Coiffé, E. Dumont, B. Quesson, ISMRM 2015*

4. Simultaneous monitoring of MR-ARFI and MR-THERMOMETRY during HIFU ablation. P.Bour, *F.Marquet, V.Ozenne, E.Dumont and B.Quesson*, SFR TECSAN 2015.

5. Simultaneous MR-ARFI and MR-Thermometry during HIFU ablation. P.Bour , *F.Marquet and B.Quesson, SFR TECSAN 2014.*